Explanatory Report for the Dublin Town, Brilliant, Falmouth and Beaumaris geological map sheets

Department of Infrastructure, Energy and Resources
Mineral Resources Tasmania

Cover: Beach outcrops of Mathinna sediments at Beaumaris. The distant hills of Mt Elephant and St Patricks Head in the centre of the photo (Ironhouse quadrangle), and Cheeseberry Hill, North Sister and South Sister to the right of picture (Falmouth quadrangle) are all formed by Jurassic dolerite capping Parmeener Supergroup rocks, which in turn rest on the St Marys Porphyrite and Mathinna Supergroup rocks. [M. Worthing]

Mineral Resources Tasmania
Department of Infrastructure, Energy and Resources

Tasmania
Explore the possibilities

1:25 000 Scale Digital Geological Map Series
— Explanatory Report 3 —

Explanatory Report for the Dublin Town (5840), Brilliant (5841), Falmouth (6040) and Beaumaris (6041) geological map sheets

by M. A. Worthing and I. R. Woolward

November 2010

Mineral Resources Tasmania PO Box 56 Rosny Park Tasmania 7018
Phone: (03) 6233 8377 ● Fax: (03) 6233 8338
Email: info@mrt.tas.gov.au ● Internet: www.mrt.tas.gov.au

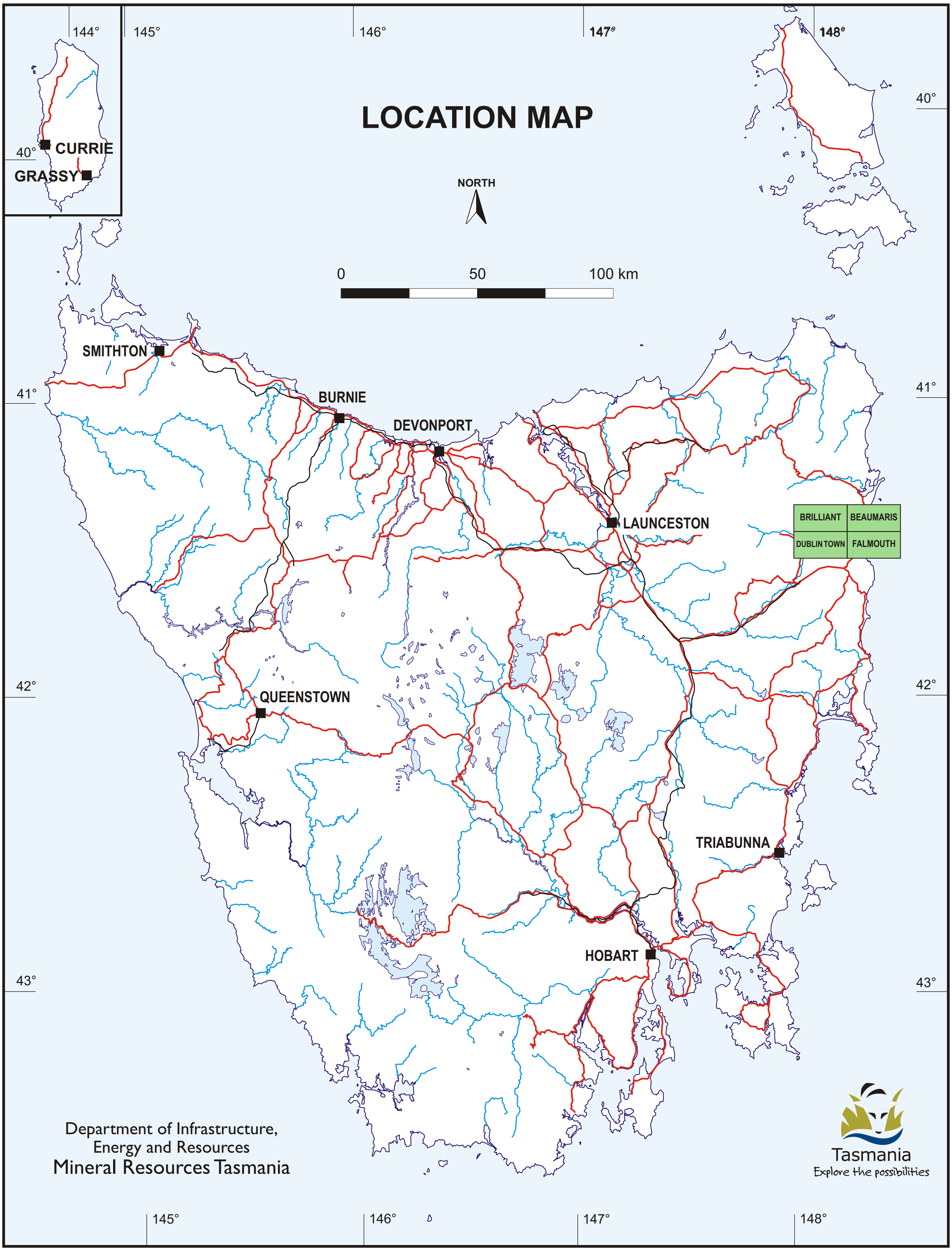

WORTHING, M. A.; WOOLWARD, I. R. 2010. Explanatory Report for the Dublin Town (5840), Brilliant (5841), Falmouth (6040) and Beaumaris (6041) geological map sheets. *Explanatory Report 1:25 000 Scale Digital Geological Map Series Mineral Resources Tasmania* 3.

CONTENTS

TABLES

FIGURES

INTRODUCTION

The work undertaken for this project is part of the Mineral Resources Tasmania *TasExplore* initiative which aims to produce an accurate 3-D model for northeast Tasmania. Such a model depends to a considerable extent on field studies aimed at elucidating the detailed structure and stratigraphy of the Mathinna Supergroup. The purpose of this project was to provide this basic information.

The project area is situated in northeastern Tasmania close to the town of St Helens (fig. 1) and includes most of the 1:50 000 scale St Helens geological map sheet (McClenaghan *et al*., 1992) together with parts of the adjacent St Marys (Turner and Calver, 1987) and Alberton (McClenaghan *et al*., 1993) 1:50 000 scale map sheets. The focus of the project was remapping the 1:25 000 scale Dublin Town (McClenaghan, 2006*b*), Brilliant (McClenaghan, 1996), Beaumaris (McClenaghan, 2002*a*) and Falmouth (McClenaghan, 2002*b*) map sheets which are bounded by grid lines 580 000 mE to 620 000 mE and 5 400 000 mN to 5 420 000 mN (all coordinates in the text are referenced to AGD66). The area is accessed via the Tasman Highway or Esk Main Road from Bicheno or St Marys respectively.

St Helens is the local administrative centre for the Break O'Day municipality and is a major fishing and tourism hub. The town has a mild temperate climate, with four distinct seasons. Summers are warm and sunny and winters are cool. Average annual temperatures vary from a high of 18.5°C to a low of 7.4°C with an average annual precipitation of 775.1 mm. The geographical position of the area means that winter temperatures are warmer than most parts of Tasmania but summer temperatures are cooler than those inland. The coastal strip to the north and south of St Helens is characterised by beautiful white sand beaches, lagoons and dunes. These natural assets, together with the equable climate and excellent fishing, have made the area a popular tourist and retirement destination.

Much of the area's pastoral and arable agriculture is confined to the lower alluvial flood plain of the Scamander River and the area west of Falmouth. Here sheep and cattle are raised, wheat is grown and fruit orchards and associated industries support the local economy. The remainder of the area is covered by dry sclerophyll forest with some wet sclerophyll on the higher peaks to the west. Logging is confined to the easterly coastal zone around Scamander Tier (fig. 1). Here much of the natural forest has been clear felled and reforested with radiata pine plantations. Forestry tracks are abundant in this area and have provided excellent access. However tracks are poor in the west where mapping has relied on a few well-exposed road sections plus river and creek traverses. There is no mining activity at present but the existence of adits and excavations in the forest testify to former exploitation of the tin, copper, lead, zinc, gold and silver of the Scamander mineral field (Groves, 1972).

Physiography

The eastern part of the area consists of a gently sloping coastal piedmont underlain by dissected Tertiary sand and gravel deposits covered by thick scrub. Sand dunes occur along much of the coastal strip adjacent to the ocean. Inland the terrain is rugged with peaks rising to approximately 500 metres. The area is dissected by a dendritic pattern of deeply incised v-shaped valleys occupied by creeks which flow into the two major rivers that cross the area. The Avenue River rises in the northwest and after flowing eastwards for most of its course, joins the Scamander River some nine kilometres inland from the coast (fig. 1). Towards the estuary the valley widens and the river meanders through marshy wetlands before it is again confined by low sandstone and granite hills prior to reaching the sea at Scamander. This river system provided a useful across-strike corridor for studying the geology.

Most of the area is occupied by the sedimentary rocks of the Mathinna Supergroup but in the north the terrain is more subdued and is underlain by granitic rocks covered by a thin veneer of Tertiary and Quaternary sediments (Sloane, 1974). To the south the area is dominated by the St Marys Porphyrite, the sedimentary rocks of the Parmeener Supergroup, and Jurassic dolerite (Turner and Calver, 1987). Within the outcrop area of the Mathinna sediments, sandstone and siltstone form the bulk of the exposure in the forestry tracks and creeks. Exposure in the forest is poor but massive sandstone crops out on forest slopes where it can be traced as rubbly benches and blocky float. Mudstone usually outcrops only in creeks and areas disturbed by human activity such as road cuts. Sandstone units tend to form the ridges, although in general it is surprising how little clear relationship exists between geology and topography. This may be either because the primary drainage system was superimposed on the Mathinna sediments by removal of the overlying Parmeener Supergroup and St Marys Porphyrite (fig. 1) or because the abundance of sandstone ensured that there is very little difference in the bedrock's susceptibility to erosion and structural control.

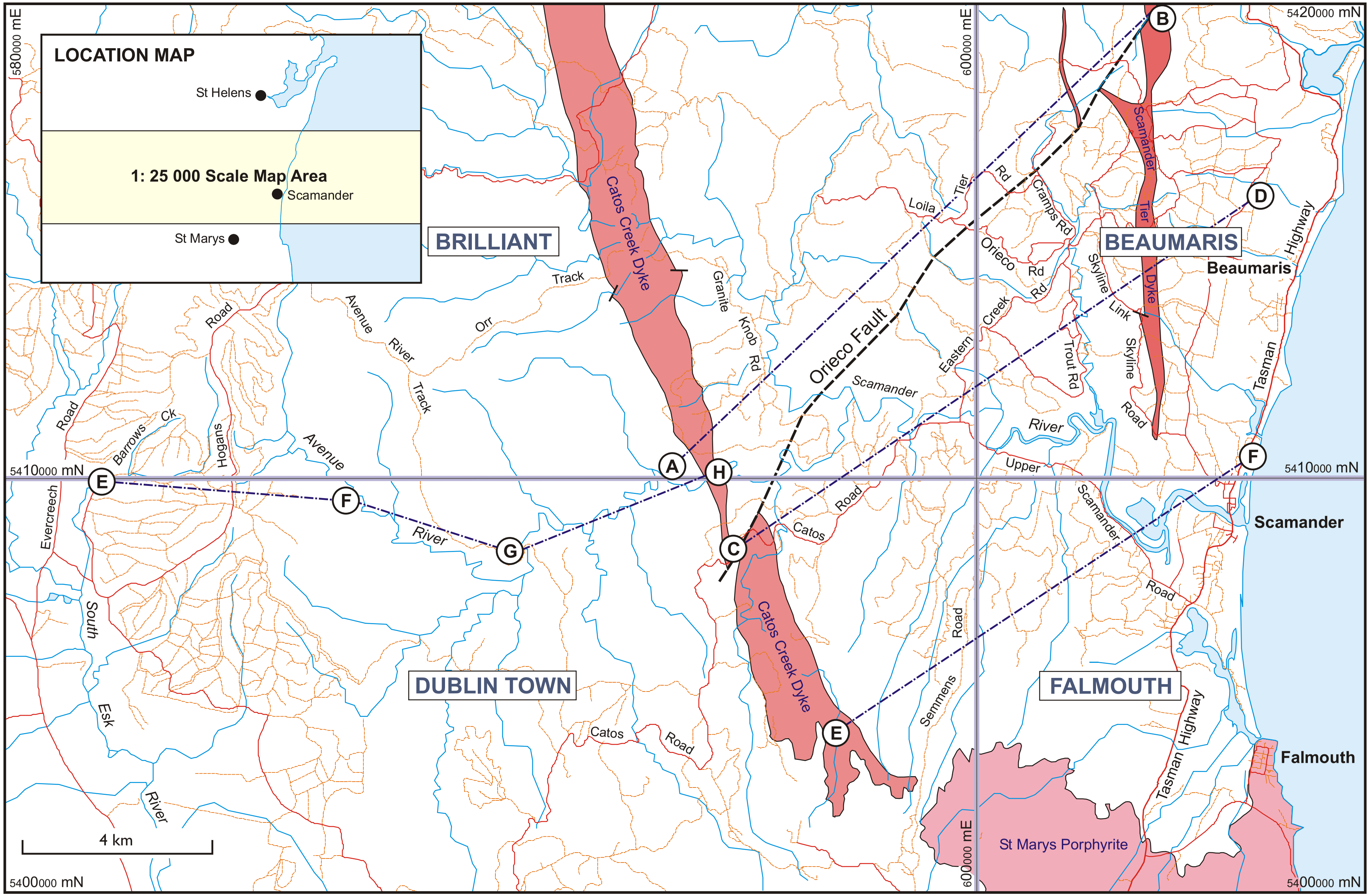

Figure 1

Location diagram. The oblique blue lines labelled A-B, C-D, E-F, G-H, F-G and E-F are lines of section (see fig. 19 and fig. 34 for appropriate sections). Inset shows relationship to local towns and boundaries of 1:25 000 scale map sheets Brilliant, Beaumaris, Dublin Town and Falmouth. Solid grey lines show map sheet boundaries.

REGIONAL GEOLOGY

Stratigraphy

The Mathinna Supergroup consists of a thick succession of turbiditic sandstone and mudstone that outcrops in northeastern Tasmania. These rocks comprise the pre-Carboniferous basement of the entire region east of the Tamar Valley. Banks (1962) noted that the Mathinna Supergroup consisted of two sedimentary associations; a lutite association with minor arenite considered to be Ordovician in age, and a younger arenite-lutite association. More recent work by Powell *et al.* (1993) suggested that the Mathinna Supergroup is about seven kilometres thick and consists of four conformable mappable stratigraphic units; the Stony Head Sandstone, the Turquoise Bluff Slates, the Bellingham Formation and the youngest Sideling Sandstone. They suggested that the relationship between the Ordovician lutite association and the younger arenite-lutite association in the Bellingham area is conformable.

The Stony Head Sandstone consists of medium to fine-grained quartzose sandstone with minor pelite characterised by a distinctive stripy cleavage (Powell *et al.*, 1993). The estimated thickness of one kilometre is speculative. The Turquoise Bluff Slates consists of massive black pelite at the base overlain by black pelite with thin siltstone and fine-grained sandstone which increases upwards. The Bellingham Formation displays classical turbidite features. Flutes, grooves and other sole marks are present but have been severely modified by strain. Cross lamination is also well preserved. The total thickness is considered to be about two kilometres. The Sideling Sandstone, which crops out in the east, is characterised by indurated quartzose sandstone which rarely shows cleavage. Load casts, convolute folds and small-scale synsedimentary slump folds are common, enabling palaeocurrent directions and other sedimentary features to be determined. The extent of this unit in the Scamander area suggested a thickness of about two kilometres (Powell *et al.*, 1993).

More recent work has resulted in a revision of the scheme proposed by Powell *et al.* (1993) for the area west of the Scottsdale Batholith. The main difference is that the Bellingham Formation has been replaced by three new formations, the Yarrow Creek Mudstone, the Retreat Formation and the Lone Star Siltstone. The base of this package is now considered to be a fault or unconformity (D. B. Seymour, pers. comm.). This supports earlier work by Reed (2001) who, based on structural criteria, suggested that this contact is an unconformity. The revised scheme is shown in Figure 2.

Group	Formation	Member	Age	Brief description
Panama Group	Sideling Sandstone		Early Devonian (plant fossils)	Dominantly fine-grained sandstone, some interbedded siltstone
	Lone Star Siltstone		Late Silurian (graptolites)	Dominantly thin-bedded siltstone with interbedded fine-grained sandstone increasing towards the top
	Retreat Formation		Silurian?	Interbedded turbiditic medium to very fine-grained sandstone and subordinate siltstone-mudstone
	Yarrow Creek Mudstone		Silurian?	Dominantly thin-bedded mudstone, with subordinate cross-laminated siltstone
Inferred faulted unconformable contact				
Tippogoree Group	Turquoise Bluff Slate		Early–Middle Ordovician (graptolites)	Phyllitic dark grey-black slate; recumbent folds and cleavage
		Industry Road Member	Ordovician?	Interbedded phyllitic slate and foliated very fine-grained sandstone; ridge-forming recumbent folds and cleavage
	Stony Head Sandstone		Ordovician?	Graded thick-bedded fine-grained turbiditic sandstone with minor interbedded pelite; large-scale recumbent folds and cleavage

Figure 2

Revised stratigraphy for Mathinna Supergroup (after Seymour, in prep.).

Geochronology

Rickards and Banks (1979) described an Early Devonian (Pragian) monograptid from the Scamander area. The fauna from this locality also includes poorly preserved remains of vascular plants, rugose corals, polyzoans, brachiopods, bivalves and crinoids, a conularid, orthocone cephalopods and abundant dacryoconarids, all assigned to the Early Devonian. Powell *et al.* (1993) suggested that these rocks are equivalents of the Sideling Sandstone. Banks and Smith (1968) described Arenigian (Lower Ordovician) graptolites from the Turquoise Bluff Slates in the Lefroy area. Subsequently, Rickards *et al.* (1993) described a Silurian (Ludlovian) monograptid fauna from a mudstone facies at Golden Ridge, some 20 km WSW of St Helens and northwards along strike from the western part of the project area. This discovery fills the long gap between the Early Ordovician at Turquoise Bluff and the Early Devonian at Scamander. Together these fossils bracket the known biostratigraphic age of the Mathinna Supergroup.

Zircon inheritance data from the Mathinna Supergroup (Black *et al*., 2004; Black *et al*., 2010) suggested that the sediments may have been derived from Neoproterozoic and Cambrian sedimentary and igneous rocks. Ages cluster around 550 Ma for both the Stony Head Sandstone and the upper part of the Mathinna Supergroup. Black *et al.* (2004) showed that there is little evidence of a zircon component from the Mt Read Volcanics and concluded that western Tasmania was not a significant source area for the Mathinna Supergroup sediments. Neither is there evidence of a contribution from the Tasmanian Proterozoic sedimentary rocks which are dominated by 1850 to 1650 Ma zircons. The data thus suggests that western and eastern Tasmania were not joined when the Mathinna sediments were being deposited. The zircon data is also consistent with Sr isotopic data (Gray and Webb, 1995) suggesting that the turbidites were derived from a predominantly Cambrian province in the Lachlan Orogenic Belt, probably by erosion of the Delamerian Orogen (Black *et al*., 2004; Gray and Webb, 1995; Gray and Foster, 2004; Black *et al*., 2010). In the Silurian to Early Devonian, the depositional environments and tectonic setting changed dramatically across large areas of the Lachlan Orogen, although the eroding Delamerian Mountain chain continued to supply sediment to an extensive sedimentary basin in central Victoria and northeast Tasmania until the final stages of marine deposition terminated in the mid-Devonian. The extensive nature of the turbiditic sediments suggests that the tectonic setting was most likely a passive margin (Gray and Webb, 1995).

Structure

Powell and Baillie (1992) recognised two deformation events in the western outcrop area of the Mathinna Supergroup. The earliest of these (F_1) produced upright to locally east-facing overturned folds in the Early Devonian. A second deformation (F_2), in the early Middle Devonian, rotated parts of the Mathinna Supergroup to a recumbent attitude. This second deformation, together with southwesterly verging imbricate thrusts, is said to be related to fault bend folding above ramps in an east-dipping sole thrust in which there has been a minimum of 25 km of southwesterly displacement. Cleavage development appears to be related to stratigraphic level. In the lower part of the Mathinna Supergroup cleavage in psammites is poorly developed to absent. A second generation cleavage is developed together with F_2 folds.

Reed (2001) suggested a more complex structural and depositional history, proposing two phases of deposition and deformation within the Mathinna Supergroup. In the Turquoise Bluff Slates and Stony Head Sandstone west of Pipers River he recognised east-facing open to tight recumbent folds with a slatey cleavage (S_1). The folds plunge northwest and are associated with west-dipping thrusts suggesting tectonic transport to the east. In the overlying Bellingham Formation and the Sideling Sandstone east of the Pipers River, Reed documented upright to northeast-verging open to concentric chevron folds with axial planes striking northwest and dipping steeply to the southwest. A weakly developed axial plane slatey cleavage is present and is considered to be the oldest fabric in the Bellingham Formation. In the west the early slatey cleavage (S_1) in rocks correlated with the Turquoise Bluff Slates is refolded and overprinted by a second closely-spaced disjunctive cleavage in pelitic units (S_2). Upright chevron folding is not seen but a late crenulation cleavage (S_3) was observed. This suggests that the upright folds are clearly later than the recumbent structures. Based on this evidence and palaeontological considerations, Reed (2001) suggested an Ordovician depositional age for the Turquoise Bluff Slates and Stony Head Sandstone followed by deformation in the Upper Ordovician during the Benambran Orogeny. Uplift and erosion was followed by unconformable deposition of the Bellingham Formation and Sideling Sandstone in the Middle Silurian followed by Early Devonian deformation during the Tabberabberan Orogeny. This is consistent with the recent revision of the Mathinna Supergroup stratigraphy proposed by Seymour (pers. comm.). Both the Benambran and Tabberabberan orogenies are part of the Lachlan Orogenic cycle (Gray and Foster, 2004).

Patison *et al.* (2001) also recognised two regional folding events in the Mathinna Supergroup. An Early Devonian phase (D_1) is characterised by northeast to east-directed thrusting with regional scale folds and thrusts. Widespread cleavage west of the Catos Creek Dyke (S_1) is a penetrative structure defined by white mica which is spaced in sandstone and slatey in pelitic rocks. East of the Catos Creek Dyke cleavage is restricted to pelites and locally, at Scamander in the east, only an intersected pencil cleavage is seen. A second deformation (D_2) involved west-directed thrusting which post-dates the unconformable St Marys Porphyrite and associated Scamander Tier Dyke and Catos Creek Dyke intrusive rocks (388 Ma) (fig. 1). D_2 also pre-dates the mid to late Devonian adamellite and granite plutons.

Keele (1994) mapped the structure along the Mathinna–Alberton gold lineament with a view to documenting structural controls involved in the gold mineralisation. He recognised two major phases of deformation; an early phase of low angle east-directed thrusting (D_1) which he associated with the main phase of the Tabberabberan Orogeny, and wrench faulting on northwest to NNW-trending faults. These thrusts are accompanied by NNW-trending folds which plunge at a shallow angle to the northwest and southeast. During D_1 a northeast to southwest-trending sinistral D_1 transfer zone was active and resulted in a mismatch in the structure and stratigraphy south of Mathinna. Small-scale second generation folds (F_2) with a well-developed north to northeast axial plane fracture cleavage (S_2) occur around gold-bearing lodes. Elsewhere the existence of large scale F_2 folds is inferred from girdle distributions of S_0 and S_1 on stereograms. Keele interpreted these relationships as being due to either superimposition of S_2 on S_1 or dextral shear along north-trending faults.

Goscombe *et al.* (1994) documented profuse small-scale and mega-scale kink bands in the Mathinna Supergroup. The kink bands were formed by a 166° ± 10° trending bulk shortening strain close to the trend of the S_1 which was sub-vertical and trended 157°. These structures post-date Middle Devonian granodiorite batholiths and pre-date deposition of the Parmeener Supergroup between 300 and 375 Ma. D_1 and D_2 both involved intense shortening along an ENE to WSW trending horizontal axis. D_1 occurred prior to the St Marys Porphyrite (before 388 Ma) and D_2 shortly afterwards. Thus the kinks are not a late stage episode of the same tectonic cycle as D_1-D_2 but a younger tectonic event. Keele's (1994) D_1 transfer zone was reactivated during the megakinking, resulting in anticlockwise rotation relative to areas to the east.

Regional metamorphism

Patison *et al.* (2001) conducted an east to west illite crystallinity survey across the entire outcrop of the Mathinna Supergroup. Their data suggested a decrease in temperature from west to east from borderline epizonal conditions (>300°C) in the west to the dominant anchizonal conditions in the east (200–300°C). They concluded that structural thickening of approximately ten kilometres was caused by D_1 thrusting followed by peak metamorphism. Peak metamorphism does not correlate with stratigraphic position or age and does not change across most of the large faults. However the Avenue River Fault Zone to the east of the outcrop area does show a significant variation in illite crystallinity across a three kilometre wide zone of D_1 thrusts, suggesting additional post-metamorphic movement. Patison *et al.* (2001) suggested that this is related to Middle Devonian D_2 westward-directed thrusting.

Igneous rocks

The Mathinna Supergroup was intruded by large volumes of granitic and granodioritic magma between the Devonian and Carboniferous, (McClenaghan, 2006*a*; Black *et al.*, 2010). U-Pb dates on zircons showed that intrusion occurred over a period of about 23 Ma from about 377 to 400 Ma (Black *et al.*, 2005). The earliest bodies were pre-tectonic, relatively mafic I-type granodiorites that may be arc related and indicate a relatively thin and cool mid-crust. Subsequent granites were more felsic and fractionated S-type granites. This progression may be related to crustal thickening accompanying amalgamation of the east and west Tasmanian terranes during the Tabberabberan Orogeny.

The four oldest dated intrusions are foliated by a distinct north or northwest-trending post-emplacement foliation defined by alignment of mafic minerals. This was correlated by Reed (2001) with his D_3 phase of the Tabberabberan folding, equivalent to the D_2 event of Powell and Baillie (1992). The latter authors also linked it with Tabberabberan structures on the mainland. Possible tectonic settings include association with an intraplate plume, or with flat subduction. It is considered more likely that the granites formed in a convergent plate margin (Black *et al.*, 2010).

Palaeozoic igneous activity was terminated by the intrusion of dolerite dyke swarms along pre-existing northeast to southwest-trending sinistral strike-slip faults.

Contact metamorphism

The host Mathinna Supergroup sediments suffered contact metamorphism adjacent to the granitoid intrusions. This is expressed by spotting in pelitic rocks and recrystallisation and hardening of the sandstones. Pelitic rocks close to the contacts contain the assemblage cordierite + muscovite + biotite + quartz + K-feldspar + ilmenite-rutile ± andalusite ± plagioclase (Goscombe *et al.*, 1992). Geothermometry and geobarometry suggested conditions of >450–500°C and 1000–1750 bar. In addition, geothermometry on two of the intrusions suggested a melt temperature of about 650 to 700°C during intrusion and emplacement pressures of 900–1300 bars (3.15–4.55 km depth). These data are consistent with pressure estimates from the sediments in the aureole. Goscombe *et al.* (1992) concluded that a large temperature gradient existed between the granitoids and the contact aureole, implying the absence of a thermal insulation effect which would have been provided by a thick section of overlying crust. The absence of such a blanketing effect implied a short-lived thermal pulse in the contact aureole with very little heat imparted to the country rock. The shallow emplacement depth is supported by the presence of coeval extrusive rhyolitic rocks of the St Marys Porphyrite (fig. 1).

PREVIOUS WORK ON THE PROJECT AREA

The most comprehensive general studies on the project area are documented in the 1:50 000 scale St Helens geological map sheet and explanatory report (McClenaghan *et al*., 1987, 1992), the 1: 50 000 scale Alberton geological map sheet to the west (McClenaghan *et al*., 1993) and the 1:50 000 scale St Marys geological map sheet and explanatory report to the south of the St Helens sheet (Turner *et al*., 1984; Turner and Calver, 1987). More detailed studies include Turner *et al.* (1986), who described the St Marys Porphyry. Powell *et al.* (1993) provided an excellent account of the sedimentology of the Mathinna Supergroup including four detailed logs from the Scamander area. Taylor (1992) conducted a general geological study with emphasis on the structure.

The Mathinna Supergroup occupies up to half the outcrop areas of the St Helens and Alberton quadrangles but is restricted to the northern and central eastern parts of the St Marys quadrangle. This large area of essentially undifferentiated Mathinna sediments is bounded to the north and west by Devonian granites (McClenaghan *et al*., 1992; McClenaghan *et al*., 1993) and to the south by the St Marys Porphyrite and an extensive area of Parmeener Supergroup sedimentary rocks and Jurassic dolerite (Turner and Calver, 1987). Some flat-topped ridges, particularly in the west, are capped by outliers of Parmeener Supergroup sedimentary rocks, Jurassic dolerite and Tertiary basalt, suggesting that the Permian unconformity surface was close to the present summit tops in this area. Two linear north-south trending dyke-like intrusions, the Scamander Tier Dyke to the east and the Catos Creek Dyke to the west (McClenaghan *et al*., 1992; Turner and Calver, 1987), subdivide the main sediment outcrop. These intrusions are important because they were intruded along major faults and also because they provide a geochronological time line against which the structural chronology of the area can be unravelled.

Stratigraphy

The two-fold subdivision of the Mathinna sediments into lutite and arenite associations (Banks, 1962) remained unchanged until Taylor (1992) proposed a four-fold facies subdivision of the Mathinna Supergroup in the project area. Taylor based this subdivision on the proportions of sandstone and siltstone plus textural and mineralogical considerations. McClenaghan *et al.* (1992) suggested a three-fold stratigraphic subdivision based on lithological and bed thickness criteria. P. R. Williams used this subdivision for mapping a small area centred on 602 500 mE, 5 416 500 mN (McClenaghan *et al*., 1987). D. B. Seymour (pers. comm.) advocates the use of mudstone:sandstone ratios as a means of characterising mappable units.

The most comprehensive study of the sedimentology of the Mathinna Supergroup across the whole outcrop area was conducted by Powell *et al.* (1993). They documented their work around six detailed logs, four of which are from the Scamander area, and concluded that the rocks are proximal in aspect and predominantly C,D channel-related lobe transition or overbank facies (Walker and Mutti, 1973). The rocks contain abundant sedimentary structures such as cross lamination, load casts, convolute folds and small-scale synsedimentary slump folds.

The different schemes discussed above illustrate the difficulty in establishing a coherent stratigraphy for the Mathinna sediments and in using the stratigraphy to define mappable units based on consistent sedimentological characteristics. In this report the authors have adopted a simple scheme similar to that used by Williams (McClenaghan *et al*., 1992) although without the restrictive definition of bed thicknesses.

Igneous rocks

The Catos Creek Dyke, the Scamander Tier Dyke and the St Marys Porphyrite (fig. 1) were intruded along probable F_1 thrusts and post-date the major tectonic structures in the country rocks. The Catos Creek Dyke and the Scamander Tier Dyke are displaced by a sinistral strike-slip fault which is herein called the Orieco Fault. To the south of this structure the Catos Creek Dyke is dominantly a hornblende granodiorite, but to the north it is composite, consisting of granodiorite, quartz porphyry and adamellite. The latter appears to be older than the granodiorite. There is a zone of contact metamorphism to the west but this is absent to the east and the contact is believed to be a fault (McClenaghan *et al*., 1994).

The Scamander Tier Dyke is a porphyritic microgranodiorite. Both contacts are steeply dipping and there is a narrow chilled margin but contact metamorphism is absent, probably because the relatively small intrusion volume was unable to impart sufficient heat to the country rocks.

The St Marys Porphyrite is situated in the northern part of the St Marys quadrangle. This body is interesting because it contains the only extrusive rocks associated with Devonian granitoids in Tasmania (Turner *et al*., 1986). It is about 1400 m thick and is predominantly a dacitic, welded, ash flow tuff together with the high level vesiculated part of the volcanic feeder (Turner *et al*., 1986; Turner and Calver, 1987). The eastern boundary is a subsidence fault which threw the extrusive rocks against the Catos Creek Dyke which is a deeper unvesiculated feeder. Geochemical and mineralogical studies strongly support a comagmatic relationship for the St Marys Porphyrite, Catos Creek Dyke and Scamander Tier Dyke which are linked to the I-type magmatism of the Blue Tier Batholith. Their age of emplacement, as determined by the Rb-Sr and K-Ar methods, is 388 1 Ma (Turner *et al*., 1986).

Pre-Parmeener Supergroup igneous activity was terminated by the intrusion of dolerite dyke swarms along pre-existing northeast to southwest-trending faults. These dykes have been dated at about 330.2 5.6 Ma (Mid-Carboniferous) (McClenaghan and Everard, in prep.).

Summary

- Deposition of the Mathinna Supergroup turbiditic sediments between the Lower Ordovician and the Lower Devonian (Banks and Smith, 1968; Rickards and Banks, 1979; Rickards *et al.*, 1993). The sediments were probably derived by erosion of the Delamerian Orogen (Gray and Webb, 1995; Gray and Foster, 2004). Reed (2001) suggested that deposition occurred in two phases separated by deformation, uplift and erosion followed by further deformation.
- All authors recognised an early phase of deformation (D_1). This produced westerly-dipping thrusts and associated easterly-verging folds with an axial plane cleavage (S_1). Keele (1994) suggested that a northwest-trending fault near Mathinna acted as a D_1 transfer zone.
- Emplacement of the St Marys Porphyrite and its associated feeders, the Scamander Tier and Catos Creek dykes at 388   1 Ma, probably along D_1 thrusts (Turner and Calver, 1987; Taylor, 1992). Contact metamorphism of the Mathinna sediments.
- Structures in the St Marys Porphyrite (Turner and Calver, 1987) suggested that the D_1 event was prolonged, continuing after intrusion of the porphyrite.
- Stacking of D_1 thrust sheets resulted in crustal thickening of up to 10 km followed by peak metamorphism (Patison *et al.*, 2001).
- Sinistral strike-slip faulting along the northeast to southwest-trending Orieco Fault displaces the outcrop of the Catos Creek and the Scamander Tier dykes.
- Keele (1994) also recognised a second deformation phase after D_1, describing F_2 folds with an associated S_2 cleavage in the Mathinna area. Patison *et al.* (2001) described a west-directed thrusting event in the west (D_2) whose relationship to the F_2 event of Keele (1994) is unclear.
- Regional mega-kinking resulting from a 166° ± 10° trending bulk shortening strain. Keele's (1994) area rotated anticlockwise relative to areas to the east (Goscombe *et al.*, 1994).
- Intrusion of dolerite dyke swarms along pre-existing northeast to southwest-trending faults.

SEDIMENTOLOGY

The focus of this project was to investigate the structure and sedimentology of the Mathinna Supergroup. Thus other rock units in the project area, which include Devonian granites, the Permo-Triassic Parmeener Supergroup, Jurassic dolerite and Tertiary deposits are not discussed, except where they serve to clarify relationships within the project focus. The sedimentology of the Mathinna Supergroup will be considered within a geographical framework:

- The first area is to the east of the Catos Creek Dyke and comprises the 1:25 000 scale Beaumaris map sheet (Worthing, 2010*a*) and parts of the Falmouth map sheet (Worthing, 2010*b*) (fig. 1).
- The second area lies to the west of the dyke and comprises most of the 1:25 000 scale Brilliant (Worthing and Woolward, 2010*a*) and Dublin Town (Worthing and Woolward, 2010*b*) map sheets (fig. 1).

Although there is considerable overlap between the sedimentology of these two terrains there are also important differences, particularly in the far west where structural and sedimentological variations are observed that are transitional to project areas further west (e.g. Keele, 1994; Cracknell, 2009; M. Vicary, pers. comm.).

Eastern area

Apart from the Devonian granites, the sedimentology of the Mathinna Supergroup is the best studied aspect of the project area. There are reports by Walker (1957), Williams (1959), Turner and Calver (1987), McClenaghan *et al.* (1992), Taylor (1992) and Powell *et al.* (1993). The rare fossil occurrences have also been described (Rickards and Banks, 1979; Rickards *et al.*, 1993). Powell *et al.* (1993) presented the most comprehensive study of the sedimentary rocks and this is drawn upon in the following section. There is general agreement that the Mathinna Supergroup consists of an interbedded sequence of poorly-sorted sandstone, siltstone and mudstone deposited by turbidity currents in the Palaeozoic.

Two fundamental problems were encountered during mapping of the Mathinna sedimentary rocks. The first was establishing a coherent stratigraphy in the laterally and vertically variable turbiditic succession. The second problem was the identification of mappable horizons within this stratigraphy, a problem exacerbated by the lateral discontinuity of many facies and the obvious overlap in facies between logs. This quest is further complicated by the strong deformation that has resulted in the juxtaposition of thrust stacks whose relationship to each other is often unclear because of the paucity or absence of fossils. Faced with these problems most workers have attempted to use sandstone:siltstone:mudstone ratios to define the different lithofacies in broad terms. They have generally not attempted to map lithofacies boundaries and have drawn cross sections based only on structural data.

In the following section previous contributions to the sedimentology will be outlined, followed by a section dealing with observations made within this project.

Taylor (1992) proposed a four-fold facies subdivision of the rocks in the project area. He based this subdivision on the proportions of sandstone and siltstone plus textural and mineralogical considerations, but used these divisions purely for descriptive purposes, not as a basis for mapping. In summary, his facies, which are distributed from east to west, are as follows:

- Facies 1 is a sandstone-dominated sequence with interbedded mudstone and siltstone outcropping between the coast and the Catos Creek Dyke.

Facies 2 to 4 occupy the ground west of the Catos Creek Dyke.

- Facies 2 is characterised by equal proportions of siltstone and meta-sandstone;
- Facies 3 consists of intercalated siltstone and meta-sandstone with the latter more dominant; and
- Facies 4 is dominated by thickly bedded (up to 5 m) sandstone with lesser amounts of green siltstone. Thin beds of mudstone (<10 mm) cap the siltstone beds.

Using similar criteria, McClenaghan *et al.* (1992) suggested a three-fold stratigraphic subdivision based on lithological and bed thickness criteria:

(a) Sandstone-dominated successions where sandstone beds are >0.4 m thick and the sandstone/mudstone ratio is >1.

(b) Interbedded sandstone and mudstone sequence where sandstone beds are usually <0.4 m thick and the sandstone to shale ratio is about 1.

(c) A mudstone sequence composed dominantly of mudstone with rare siltstone interbeds and occasional thin sandstone laminae.

McClenaghan *et al.* (1992) used this subdivision for mapping a small area centred on 602 500 mE, 5 416 500 mN. D. B. Seymour (pers. comm.) advocates the use of sandstone: mudstone ratios as a means of characterising mappable units.

As noted above the most comprehensive study of the sedimentology of the Mathinna Supergroup was conducted by Powell *et al.* (1993). They documented their work around six detailed logs, four of which are from the east of the project area (fig. 3). In the following section these logs will be summarised in order to document the range of turbidite facies present. In their descriptions and classifications Powell *et al.* (1993) used the Bouma facies system of Walker and Mutti (1973). In this system CD = coarse division and FD = fine division, giving the CD/FD ratio. They also used the ABC index (%) where A = ½B and A and B represent the percentages of beds in a group of beds beginning with Bouma divisions A and B respectively. So for example, if all beds begin with division A, the ABC index is 100%. If all the beds begin with division C, the ABC index is 0. Following these summaries the samples collected by the present authors will be described within the framework established by the logs (fig. 3).

Log summaries (after Powell et al., 1993)

Log 3: Beaumaris Pine Plantation
602 300 mE, 5 415 600 mN

This log shows classical turbidites of facies in the C-D spectrum. These have a relatively high CD/FD (2.6) and a high ABC index (77%). The log was divided into two substages of contrasting character (fig. 3):

Substage 1 comprises thin to medium-bedded, fine to coarse-grained facies C and D turbidite sandstone with CD/FD = 1.3; ABC index = 69%. The sediments were interpreted as turbidite lobe deposits.

Substage 2 comprises medium to thick-bedded, predominantly medium to coarse-grained facies C sandstone with CD/FD = 4.4; ABC index = 87%. These were interpreted as channel or channel lobe transition.

A SSE palaeoflow direction characterises both substages. The section thus records SSE progradation and vertical aggradation of a turbidite lobe with the SSE encroachment of a feeder channel represented by substage 2.

Log 4: Scamander Quarry
605 256 mE, 5 409 009 mN

Powell *et al*. (1993) divided this log into five substages of alternating thick-bedded sandy and thin-bedded pelitic character. Each substage comprises one facies association.

Substages 1, 3, 5: These substages consist of a thick bedded sandy facies which dominates the log, comprising 38 m or 83% of the 48 m total section. The CD/FD ratio is 5.5. This facies association is made up of thick and very thick commonly amalgamated beds of facies B2 and C. Medium to coarse-grained sandstone in packets 10–20 m thick are characterised by high CD/FD (~7–21). These contain sole structures indicating south to southeast flow. Mudstone intraclasts occur in some beds and soft sediment deformed bedding in others. These characteristics indicate a depositional channel (substages 1 and 5) or channel lobe transition environment (substage 3).

Substage 2: A thin-bedded pelitic facies is represented by two 4 m thick intervals. Substage 2 comprises very thin facies D turbidite siltstone and facies G? pelite with CD/FD = 0.1. This is suggestive of a deactivated channel fill.

Substage 4: This comprises very fine to fine-grained thin bedded facies D and sporadic facies C turbidite sandstone (CD/FD = 2.7) with sole structures in some of the thicker AB(D)E and BC(D)E beds indicating palaeoflow towards the SSE. Bouma C cross laminations in other mostly thinner B/C(D)E beds indicate a more variable palaeoflow between S and WSW but mostly towards the latter. These characteristics suggest that the facies represents channel related overbank deposits of the channel margin or interchannel kind.

In summary, the overall history in the Scamander quarry is one of proximal channel fill activity (substages 1 and 5) and channel-lobe transition deposition (substage 3) interrupted by a period of channel deactivation (substage 2) and channel related overbank deposition. Palaeoflow directions vary slightly between south to southeast in substages 1, 3 and 5 to between south and WSW in substage 4.

Log 5: Upper Scamander Road
602 896 mE, 5 409 076 mN

This log has the same facies associations as seen in the Scamander quarry (Log 4). It is of proximal aspect with CD/FD = 2.6 and an ABC Index of 45%. Eight substages comprise three facies associations, two of which are essentially the same as those described in Log 4. These are substages 2, 3, 5 and 7.

Substage 1: This is a thin-bedded pelitic facies but is dominated by facies C turbidites and is interpreted as lobe-like.

Substages 2, 3, 5 and 7: These comprise a thick to very thick-bedded sandy association characterised by fine to medium-grained facies C and ?B2 sandstone interpreted as channel fill and channel lobe-transition deposits. Substage 7 is interpreted as a possible crevasse-splay deposit.

Substages 4, 6 and 8: These comprise a thin-bedded pelitic facies association characterised by very fine grained facies D sandstone and facies mudrock in substages 6 and 8. They are interpreted as channel related overbank and hemipelagic deposits.

In summary the section records proximal depositional channel fill in a channel system trending NNE (substage 2) contracting with time to channel lobe transition facies and associated anticlockwise flow divergent overbank deposition in a channel margin and or interchannel area (substages 4, 6 and 8). Palaeoflow throughout the section is northerly but there is a 60–70° divergence between the NNE direction defined by sole structures in the channel-fill sandstone of substage 2 and the NNW direction defined by Bouma C cross laminations in the thin-bedded facies D turbidites of substage 4.

Log 6: Semmens Road
599 113 mE, 5 408 261 mN

This log is similar to Log 3 in terms of facies associations, stratigraphy and proximal aspect with CD/FD = 2.4 and the ABC index = 91%. It contains palaeocurrent directions opposite to areas to the north and east defined by excellent examples of both sole and top structures defining a palaeoflow direction towards the NNW. Two substages are defined by contrasting CD/FD and average bed thicknesses.

Substage 1: This is characterised by fine to medium-grained, thin to medium-bedded facies C and D sandstone with abundant sole structures and CD/FD = 1.8 and ABC index = 89%. It is interpreted as a lobe deposit.

Substage 2: This is characterised by fine to medium-grained medium to moderately thick-bedded facies C sandstone with CD/FD = 6.4 and the ABC index = 100%. It is interpreted as a channel lobe transition deposit.

In summary, the log records aggradation or NNW progradation of a turbidite lobe and NNW encroachment over this lobe of a feeder channel.

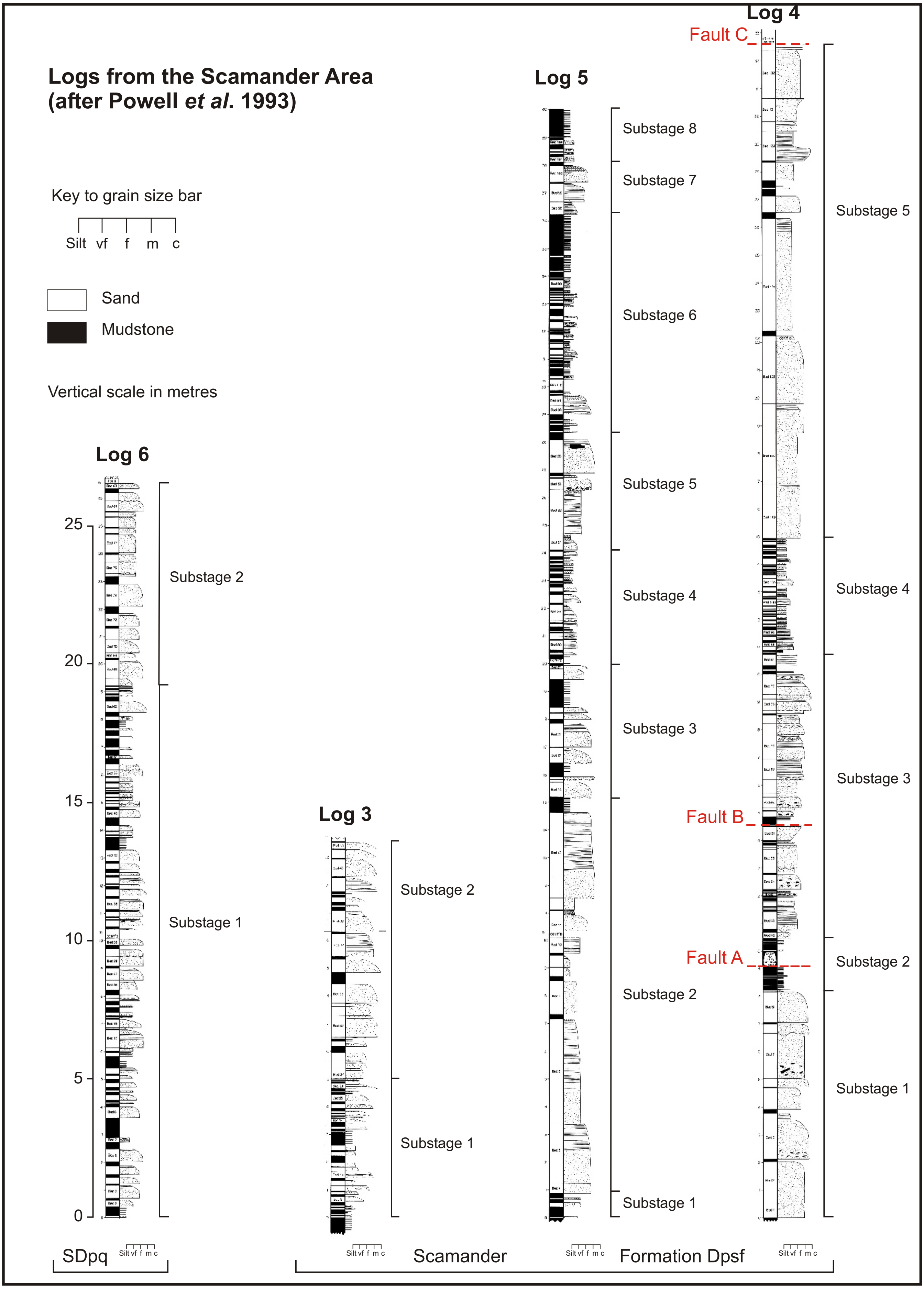

Figure 3

Stratigraphic logs after Powell et al. (1993). The logs are placed geographically left to right from west to east. Log locations are given in Powell et al. (1993), in the text and in Figure 5. Formation names are derived from this report.

In their analysis of the above logs Powell *et al.* (1993) recognised two petrofacies; a quartzose sublitharenite facies found in log 4 which was deposited by SSE palaeoflow and a feldspathic sublitharenite-litharenite facies found in logs 3, 5 and 6. Flow directions are more complex in the latter. Sediments from log 3 were deposited by SSE palaeoflow whereas those from logs 5 and 6 were deposited by NNE palaeoflow turbidites.

In the following section information gathered during the current project will be described.

Sedimentary structures

Sedimentary structures are abundant in well-exposed outcrops, particularly along road cuts and creek sections. These include graded and cross bedding, slump folds, flute castes, tool marks, ripple marks, convolute lamination and rip-up clasts in mudstone bands (fig. 4*a–f*). These structures were very useful for determining way-up but those indicating palaeoflow, such as cross bedding and flute castes, proved quite difficult to measure and in most cases no clear azimuth could be established. The rose diagram insert in Figure 5 shows a plot of these structures. In each case the bedding plane on which they were measured was rotated into the horizontal on a stereogram. Although the resulting lines are not palaeoflow directions, their orientations are in broad agreement with the azimuths shown in Figure 5 (McClenaghan *et al.*, 1992) and also with those measured by Powell *et al.* (1993).

Petrography

Specimens of the Mathinna Supergroup sedimentary rocks were routinely collected during field work with the aim of producing a representative lithological and geographically distributed sample set. A total of 194 samples were collected and 141 of these were thin sectioned for petrographic analysis. A number of these samples were collected from the areas logged by Powell *et al.* (1993); eleven from log 4, eight from log 5 and seventeen from log 6. Systematic sampling of log 3 was not undertaken as it occurs in a cliff face but two samples were collected in an adjacent creek bed. The rest of the samples were geographically distributed across the project area and were collected as representatives of particular rock types. Selected samples were also analysed by X-ray diffraction, including examples from each of the logs.

Log 3

Samples are grain-supported sandstones containing quartz, tourmaline, zircon, muscovite, plagioclase and possibly rutile and apatite. Lithic clasts are rare but consist of chert or devitrified siliceous volcanic rocks. The rocks are poorly sorted and have a low to moderate sphericity. Michel Levy tests on the plagioclase suggested that it is in the andesine range.

Log 4

All samples are grain-supported sandstones with a common mineralogy which consists of quartz, tourmaline, zircon and detrital muscovite. There may also be some apatite present. One section had a single grain of twinned plagioclase. The quartz occurs as single clear, non-composite and mildly strained grains, consistent with an igneous origin. There are also some clasts of cloudy quartz which may be due to fluid inclusions, suggesting an origin as vein quartz. The well-rounded tourmaline grains are pleochroic in shades of pale green to yellow. The zircon grains are also rounded. Rare lithic clasts include foliated siliceous metamorphic rocks and chert fragments. It is possible that the latter are derived from fine-grained siliceous volcanic rocks, as one clast appeared to have included crystallites. The matrix is difficult to resolve but appears to be phyllosilicate-rich.

There are some textural differences. Samples from the massive thick-bedded sandstone of substages 1, 4 and 5 are coarser grained. They also appear to be bimodal in the sense that the quartz clasts belong to two grainsize populations. Larger quartz grains are sub-rounded to rounded with a higher sphericity, while the more abundant smaller grains are angular to sub-angular. This mixture decreases the overall sorting of the rock. The thinner bedded sandstones from substages 3 and 4 are finer grained and are dominated by smaller, more angular quartz grains and are thus moderate to well sorted, although the sphericity is low.

Log 5

The mineralogy is subtly different from log 4. Quartz is the principal mineral but detrital muscovite, rare twinned plagioclase, tourmaline, zircon, opaques and possibly apatite are also present. Some of the tourmaline has a blue to colourless pleochroism. In contrast to log 4, detrital biotite and possibly rutile also occur. Lithic fragments include composite quartz grains, chert and foliated siliceous metamorphic grains. As with log 4, the quartz occurs as single, clear, non-composite and mildly strained grains, consistent with an igneous origin. The matrix is difficult to resolve but appears to be phyllosilicate-rich. Texturally the rocks are more varied than those sampled from log 4 and include grain-supported sandstone and siltstone together with mudstone. The sandstone and siltstone are generally moderately to poorly sorted but the grains are subangular to angular and lack the bimodal distribution seen in log 4.

Log 6

Samples generally have a higher matrix content and are texturally matrix-supported sandstone. They are poorly sorted and sphericity is low to moderate. Detrital minerals include quartz, muscovite, tourmaline and zircon together with probable rutile. In addition they contain biotite and K-feldspar, some showing Carlsbad twinning. Plagioclase is also present and Michel Levy measurements suggest that it is in the andesine range. The abundant quartz occurs as single clear, non-composite and mildly strained grains, consistent with a siliceous igneous rock origin. Lithic clasts include chert fragments, although the presence of what appears to be plagioclase laths within some of them suggests that they are microporphyries with a partially devitrified groundmass. There are also composite quartz grains of probably metamorphic origin. Some may have mylonitic textures. There are also some clasts which are composed of felted laths of chlorite. The matrix is difficult to resolve but appears to be phyllosilicate-rich.

(a) Cross bedding along Skyline Road at 603 659 mE, 5 411 173 mN.

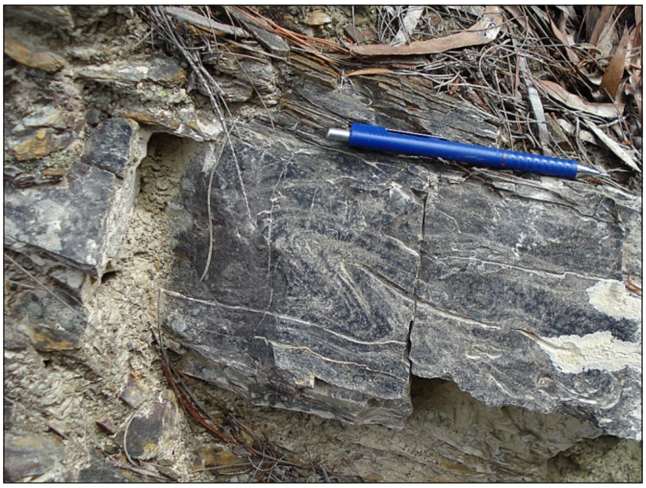

(b) Slump fold at 605 282 mE, 5 409 248 mN.

(c) Flute castes in cross section, Upper Scamander Road at 602 795 mE, 5 409 140 mN. Inset shows flutes on bedding surface.

(d) Ripple marks on bedding plane, Eastern Creek Road at 602 286 mE, 5 415 668 mN.

(e) Convolute lamination, Bolpeys Creek at 598 210 mE, 5 405 895 mN.

(f) Rip-up clasts in mudstone band, Granite Knob Road at 598 184 mE, 5 410 816 mN.

Figure 4

Sedimentary structures.

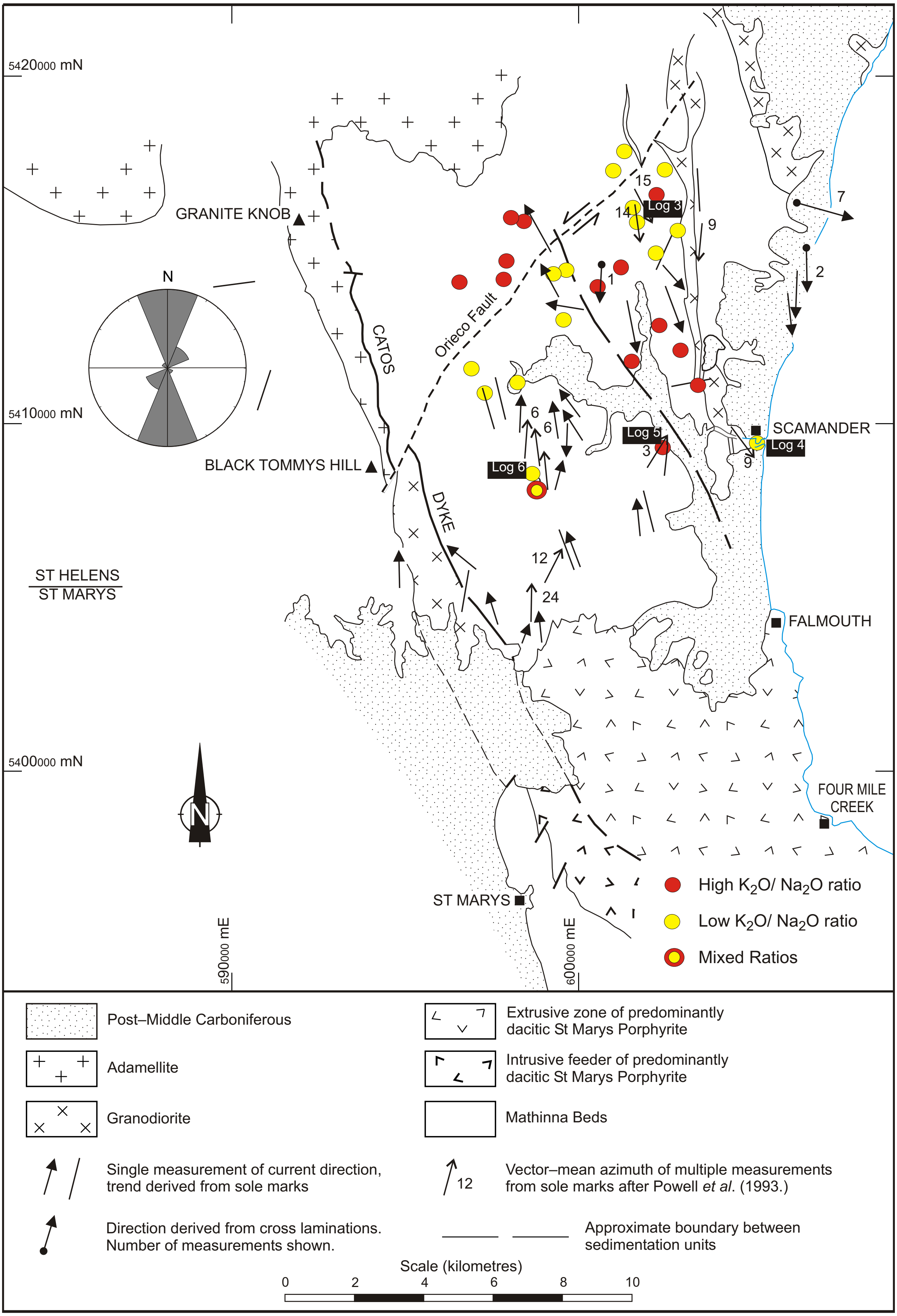

Figure 5

Map showing domains defined by current directions. Red and yellow spots are localities where samples with different K_2O/Na_2O ratios were collected. Position of logs 3, 4, 5 and 6 of Powell et al. (1993) are shown. The rose diagram inset represents data measured in this project (see text for explanation). Map modified after McClenaghan et al. (1992).

It is clear from the above that there are differences in the mineralogy of the four logged sections. These differences are summarised in Tables 1 and 2. All sections contain abundant quartz, muscovite, tourmaline, zircon and probable rutile. Logs 3, 4, 5 and 6 also contain plagioclase although it is rare in logs 4 and 5. Log 6 contains K-feldspar, including grains showing Carlsbad twinning and the characteristic cross-hatch twinning of microcline. Logs 5 and 6 also contain biotite which is absent in the other two logs. Lithic clasts in the four logs tend to be similar with chert, volcanic rocks and siliceous metamorphic rocks present in very subordinate amounts relative to the dominant quartz. Texturally, samples from log 4 are coarse-grained grain-supported rocks with an apparently bimodal distribution of quartz clasts. Large, relatively well-rounded grains are mixed with smaller poorly-sorted fragments with a lower sphericity. Samples in logs 3, 5 and 6 are very fine to medium-grained sandstone and are generally poorly sorted with a higher matrix proportion.

The above observations are more or less consistent with those made by Powell *et al.* (1993). They defined log 4 as part of a quartzose sublitharenite facies containing abundant quartz, various lithic fragments, mica and rare feldspar plus accessory green tourmaline, and considered that the well rounded nature of the clasts suggested a polycyclic origin with the sediments derived from a beach or shallow shoreface environment. They included logs 3, 5 and 6 in a feldspathic litharenite facies in which the quartz grains and lithic fragments are similar to the other facies. However, the present authors have detected only rare plagioclase and no K-feldspar in log 5. Other detrital minerals include green tourmaline, white mica, zircon and biotite. Textural characteristics (Powell *et al.*, 1993) suggest re-sedimentation and mixing of formerly texturally mature beach sands or rounded grains of polycyclic origin and texturally sub-mature sand from either fluvial, deltaic or neritic environments.

Table 1

Mineral content of logs 3 to 6 of Powell et al. (1993) determined in this project. QLF and FLAF are the quartz litharenite and feldspathic litharenite facies respectively of Powell et al. (1993).

	Log 3	Log 4	Log 5	Log 6
Current direction	SSE	SSE	NNE	NNE
Powell's facies	FLAF	QLF	FLAF	FLAF
Mineral determined by petrography (this project)				
Quartz	×	×	×	×
Muscovite	×	×	×	×
Biotite			×	×
Plagioclase	×	rare	rare	×
K-spar				×
Tourmaline	×	×	×	×
Zircon	×	×	×	×

Table 2

Mineral content of logs 3 to 6 of Powell et al. (1993) determined in this project, including data from X-ray diffraction. Also included are the K_2O/Na_2O ratio data for the different logs. QLF and FLAF are the quartz litharenite and feldspathic litharenite facies respectively of Powell et al. (1993).

	Log 3	Log 4	Log 5	Log 6
K_2O/Na_2O	Low	Low	High	Low
Current direction	SSE	SSE	NNE	NNE
Powell's facies	FLAF	QLF	FLAF	FLAF
Minerals determined by petrography (this project)				
Quartz	×	×	×	×
Muscovite	×	×	×	×
Biotite			×	×
Plagioclase	×	rare	rare	×
K-spar				×
Tourmaline	×	×	×	×
Zircon	×	×	×	×
Additional minerals detected by X-ray diffraction				
Rutile	×	×	×	×
Kaolinite			×	
Halloysite		×		
Chlorite/Vermiculite		×	×	×
Anatase		×		
Goethite		×		×

Formation descriptions

Despite the various problems outlined above, one of the aims of this section has been to establish a stratigraphy that can be used to map geological boundaries. During mapping a general impression develops as to the relative distribution of rock types in an area. Such impressions are particularly important during mapping of laterally and vertically variable sedimentary rocks such as the Mathinna Supergroup. The logs of Powell *et al.* (1993) have been very useful in formalising these impressions and assigning the rock types to particular genetically defined turbidite facies. In addition, the deformation structures observed also provided information on the lithologies present, as strain will be expressed differently in, for example, mudstone and sandstone. In the following section these different elements will be drawn together to define and name mappable formations. The criteria used will be supplemented in the following section on structural geology.

The Scamander Formation (DPsf)

This formation comprises the high ground to the east of the area and is characterised by abundant massive sandstone units. In forest outcrops, where exposure is poor, the formation often crops out as lines of bouldery rubble and together with the Scamander Tier Dyke has determined the distribution of high ground. These rocks are seen in logs 3, 4 and 5 of Powell *et al.* (1993) (fig. 3). The existence of distinctive mudstone-rich units within this package has greatly assisted the work by providing mappable units. During deformation the major structural geometry was controlled by the massive sandstone. As a result, the major folds are large, long wavelength, relatively open structures and S_0 plots as a girdle on a stereogram. Outcrop-scale folds tend to occur in the thinner bedded mudstone-rich units. Fossil evidence (Rickards and Banks, 1979) provided clear evidence that these rocks are Devonian in age. This package is thus defined here as the Scamander Formation (DPsf) and based on the cross sections, it must be at least three kilometres thick. Powell *et al.* (1993) estimated a thickness of two kilometres. It is not possible to definitively correlate different elements of logs 3, 5 and 6 across strike because of thrusting and geochemical differences which will be described below.

SDpq

To the west, separated from the Scamander Formation by a major thrust, is a unit represented on the eastern side of its outcrop by log 6. Unfortunately this is the only log within this package of sedimentary rocks. Although massive sandstone is present at the top of log 6, the whole package tends to consist of thinner-bedded sandstone with more abundant mudstone. Outcrop across the strike of this unit is good along Catos Road, Granite Knob Road and the Scamander River (fig. 1). Outcrop to the north of the Orieco Fault is generally poor although there are well-exposed sections along the northern part of Granite Knob Road and Orieco Road where a mudstone-dominated sequence is observed. The distinctive characteristics of this unit are that the sandstone and mudstone are interbedded on a smaller scale. The thick massive sandstone units that are common within the Scamander Formation are generally absent. Mudstone bands are locally mappable although evidence suggests that they are laterally discontinuous. These sedimentological differences are also expressed in the structures formed. The folds have much smaller wavelengths and tend to have a chevron geometry and the incidence of thrusting is much more intense, no doubt facilitated by the more abundant mudstone. No fossils have been found although Powell *et al*. (1993) reported the presence of carbonaceous material and radiolarians in chert clasts in log 6. Since the latter are derived they are of no use in dating the enclosing sediments. The carbonaceous material could be plant remains. Similar occurrences in the Scamander Formation were used to confirm the Devonian age (Rickards and Banks, 1979). This package is therefore defined here as SDpq. The intense folding and thrusting within the unit make estimates of thickness speculative.

Based on the occurrence of Devonian fossils in the Scamander Formation and the fossil plant *Hostimella* at The Sideling (Banks, 1962), Powell *et al*. (1993) considered that both formations defined above represent the undifferentiated equivalents of the Bellingham Formation/ Sideling Sandstone. It should be noted that in a recent revision (Seymour, in prep.) the Bellingham Formation has been replaced by three formations; the Yarrow Creek Mudstone, the Retreat Formation and the Lone Star Siltstone (fig. 2).

Western area

This includes the area west of the Catos Creek Dyke to the western edge of the project area (fig. 1).

SDpd

This unit outcrops in a thrust wedge immediately east of the Catos Creek Dyke but the major outcrop area is immediately west of the dyke through to the Avenue River Fault Zone (ARFZ). It is bounded to the south by the Permian sedimentary rocks around Mount Nicholas on the Dublin Town map sheet, and to the north by the Devonian granitoids on the Brilliant map sheet. East of the Catos Creek Dyke, the unit is thrust over the stratigraphically younger SDpq (Worthing and Woolward, 2010*a,b*). It is well exposed in the steeply incised Avenue River and related creeks and in road sections. Elsewhere outcrop quality is poor to variable. There are two type sections, one along Catos Road at 593 212 mE, 5 404 772 mN (fig. 36) and the other in a forest track at 588 893 mE, 5 408 720 mN (fig. 38).

Lithologically the unit consists of a rhythmically interbedded succession of fine-grained sandstone and cleaved siltstone. Throughout the sequence, medium to thick-bedded massive fine-grained sandstones are intercalated with typically thin to medium-bedded fine to medium-grained siltstone. The incidence of sandstone beds up to six metres thick increases towards the west. Minor shale with sharp bases occurs throughout the sequence. Due to tight folding and variable outcrop, the lateral extent of these units was difficult to determine although along-strike creek sections and LiDAR images indicate that some are extensive enough for inclusion on the geological map.

The sandstone is moderate to variable in maturity and typically comprises approximately 20% of white mica matrix. Minor detrital plagioclase clasts are visible in many sandstones towards the west of the outcrop. In thin section, the rocks are dominated by quartz but accessory minerals include biotite, some of which is slightly chloritised, muscovite, zircon, rutile and tourmaline. In this respect the mineralogy is similar to the Scamander Formation and SDpq, but unit SDpd is distinguished by a much higher content of modal feldspar which includes plagioclase (andesine) and alkali feldspar with exsolution lamellae. Minor lithic clasts include chert and some foliated metamorphic rocks.

The interbedded siltstones have a similar mineralogy to the sandstones, but typically with a smaller ratio of quartz to matrix. Texturally they are somewhat more mature than the sandstones. Sedimentary structures are common. The siltstone may be thinly laminated or massive. Normal grading is common in both sandstone and siltstone and some beds are terminated at the top by mudstone or shale. The very thickly bedded sandstone usually displays negligible grading but ungraded and basal reverse-graded beds are also present. Other sedimentary structures include flutes, cross beds and rare mud rip-up clasts at the base of some sandstone beds. Bioturbation was not observed and macro-fossils were not found during the mapping nor have they been documented by other workers. The unit is not readily distinguishable from surrounding units by geophysics or geochemistry.

Although detailed sedimentary logs of these units have not been prepared, field evidence suggests that the sediments were deposited by turbiditic flow processes. Many beds show features commonly associated with the Bouma sequence (Walker and Mutti, 1973). Divisions Ta, Tb, Tc and Td are ubiquitous. The lack of coarse-grained sand and granules at the base of the sandstone beds is typical of the Mathinna Supergroup beds in northeast Tasmania and is interpreted to be the result of deposition from a mature source. Normal grading of massive sandstone beds is also recognised by critics of the Bouma model as being characteristic of turbidite deposits. Although the very thickly bedded sandstones and probably some other more poorly sorted sandstone beds may represent sandy debris flows, such units are best interpreted as being products of deposition from moderate to high energy turbidite flows. The absence of pelagic sediments and bioturbation, together with structures indicating bottom currents, suggests that there are no significant muddy contourites. These features, together with the maturity and areal extent of the sediments, are consistent with moderately distal deposition. The widespread presence of feldspar, together with accessory minerals found in neighbouring units, suggests derivation from a granitic source.

SDpf

Unit SDpf lies entirely within the eastern area of the SDp and is exposed in the headwaters of the Avenue River and in eastward-flowing rivers to the north and south (Worthing and Woolward, 2010*a,b*) (fig. 1). Outcrop is generally poor and the fine-grained rocks are preferentially weathered. The unit is dominated by grey, foliated, very fine to medium-grained siltstones. Slate has developed locally and sandstone, which is typically fine grained, is rare. This contrasts with the sandstone-dominant SDp that encloses the SDpf. Fossils and bioturbation were not recorded. Thin planar laminations were the primary means by which bedding was recognised, although weathering and shear fabrics make these laminations difficult to recognise with confidence. Locally the slaty cleavage has been transposed into parallelism with bedding and boudinaged laminations have also been observed. Small-scale folds and outcrop-scale faults are common and these structural features, together with the TDR image (fig. 12), suggest that the unit may have preferentially accommodated strain within the ARFZ.

Interpretation of the depositional environment of SDpf is compromised by its limited areal extent, poor outcrop and lack of geochemical data. The dominant thin planar laminated siltstone and lack of sandstone that characterise the unit are consistent with deposition from distal turbidite flows. The presence of detrital plagioclase in the sandstone probably indicates that the unit has the same source as the surrounding SDp. More work is required to characterise the SDpf and its depositional environment, although the unit shares similar sedimentary characteristics with the basal portion of the Lone Star Siltstone (fig. 2).

The unit is distinguishable locally from SDpd by its yellow colour on the radiometric image (fig. 16). The loose association between the SDpf and long wavelength high amplitude magnetic signatures in Figure 16 may indicate an increased density of faulting within the less competent siltstones that characterise the lithology. This is consistent with the features described above.

SDp

This unit is exposed in the comparatively flat terrain between Evercreech Road and the headwaters of the Avenue River (Worthing and Woolward, 2010*a, b*) (fig. 1). Most of the unit lies within the Avenue River Fault Zone and is bounded to the south by Permian and Quaternary cover and to the north by the Blue Tier Batholith. Exposure is poor to moderate but rivers and creeks extending six kilometres west of 586 902 mE, 5 409 633 mN provide a representative type section (fig. 34*a*). This generic unit replaces the previous ODqp, ODq, ODqq and ODp and their metamorphic equivalents (McClenaghan *et al*., 1993), and has been created to account for geological discrepancies across previous map sheet boundaries and to accommodate observations made during this project. Units SDp, SDpf and SDpd have been emplaced along a series of thrusts over the stratigraphically underlying unit SDpq. It is possible that the overlying unit SDpsa, west of SDp, has also been structurally emplaced.

SDp comprises undifferentiated sandstone, siltstone and mudstone. Fine-grained sandstone dominates in the east (Domain 2 in fig. 34*a*) and very thick, laterally extensive sandstone beds up to six metres thick crop out on the upper slopes of the Avenue River headwaters (fig. 15, 34*a*). These are typically separated by two to ten metre thick intervals of rhythmic thin to medium-bedded fine to medium-grained siltstone. Siltstone tends to dominate in the west, although this area is poorly exposed (Domain 3 in fig. 34*a*) and is interpreted as the shallow limb of a fold, making the ratio of sandstone to siltstone difficult to assess. Where weathering and the effects of deformation allow observation, the siltstones are typically thinly laminated. Carbonaceous mudstone is relatively rare and is not extensive along strike.

Limited thin section work showed that the sandstones are poor to moderate in maturity with a 30–40% mica and patchy chlorite matrix. Quartz is the dominant mineral but macroscopic plagioclase clasts are a notable but rare feature. Accessory minerals include rutile, tourmaline, zircon and probably ilmenite. The siltstones comprise a similar mineralogy and the modal content of mica is often similar to that of quartz. Texturally the siltstones are somewhat more mature than the sandstones.

Sedimentary structures are common. Flutes and cross bedding are abundant in the rhythmic sandstone-siltstone interbeds. Normal grading is present in both sandstone and siltstone and some beds are terminated at the top by mudstone or shale. The very thickly bedded sandstones usually display minor normal grading, and commonly have sharp tops. Rare mud drapes are also present. Siltstone is typically laminated and rare bioturbation is also present. The fossil *Protovirgularia nereitarum* was tentatively identified by Banks (1992) from a float sample two kilometres north of the project area at 582 900 mE, 5 411 800 mN (± 100 m). Rickards *et al*. (1993) have also documented the presence of Ludlow graptolites at Golden Ridge (586 300 mE, 5 415 000 mN) which lies within the outcrop area of SDp.

The unit is distinguished from SDpd and younger units by its yellow colour on the radiometric image (fig. 16). The unit's signature on the magnetic images is complicated by the effects of intrusive bodies and faults (fig. 12). Geochemical data for SDp was not obtained.

Interpretation of the depositional environment of SDp is also compromised by its limited areal extent, poor outcrop and lack of geochemical data. It is probable that the unit represents a range of depositional environments. Banks (1992) suggested a deep marine environment for the rocks hosting the fossil *Protovirgularia nereitarum* near Evercreech. Rickards *et al*. (1993) envisaged the graptolite locality at Golden Ridge as a local sediment-starved portion of a turbidite-dominated submarine fan. The intercalated rhythmically interbedded sandstone and siltstone exhibit features consistent with Bouma divisions Ta, Tb, Tc and Td (Walker and Mutti, 1973). The extensive, very thick fine-grained sandstone beds may represent sheet flows. The detrital plagioclase and other accessory minerals are consistent with a provenance that includes a granitic source. Based on features that include the presence of Ludlow graptolites, lithological similarities, sedimentology and radiometric signatures, this unit is tentatively correlated with the Lone Star Siltstone (fig. 2) west of the Sideling Range.

Sedimentary geochemistry

Selected examples of rocks from the project area were thin sectioned and subdivided petrographically into sandstone (85), siltstone (27) and mudstone (27). Major and trace element geochemistry was determined using X-ray fluorescence, giving a total of 141 fully-analysed rocks. Hornfels were not included in this data set. In addition, selected samples were analysed for mineral and modal content using X-ray diffraction. The purpose of these studies was three-fold: to characterise the geochemistry of the rocks; to use this information to assist with structural interpretations, correlations and provenance studies; and to compare the geochemistry of the rock units in the project area with other areas within the Mathinna Supergroup outcrop.

Whole-rock geochemistry

The geochemical classification of Herron (1988) was used to classify the sediments (fig. 6*a*), with the samples ranging across the diagram from the sublitharenite field through to shale. Sandstone of the Scamander Formation tends to plot in the sublitharenite field whereas the sandstone of the SDPq and SDpd plot in the litharenite field. The siltstone of all groups trend into the wacke field and the mudstone into the shale field. This distribution reflects quite well the grainsize allocations determined by petrographic study. Figures 7*a–i* are variation diagrams showing major elements plotted against SiO_2 for all sandstone and siltstone. Much of the spread on the diagrams is related to the nature of turbidites whose grainsize ranges and textures are determined by gravitational settling from turbidity flows. In the Mathinna sediments the dominant clastic mineral is quartz, thus the depositional process produces a range from grain-supported quartz sandstone through to matrix-supported quartz sandstone and siltstone with higher proportions of phyllosilicate-rich matrix. Mudstone forms the lightest fraction. Figure 7*a–i* shows that these geochemical transitions are also closely linked to grainsize.

SiO_2 values tend to be higher for the Scamander Formation which is consistent with dominance of quartz-rich sandstones in this unit. The TiO_2, Al_2O_3, Fe_2O_3T and K_2O diagrams (fig. 7*a–c*,*h*) show coherent trends that may broadly be explained as mixing lines between quartz and mica. TiO_2 is also present in rutile which has been identified by X-ray diffraction. It may be present within rutilated quartz but has also been identified as a separate phase. The CaO and Na_2O diagrams (fig. 7*f*,*g*) show similar but more scattered distributions that may be partly related to the presence or absence of modal plagioclase in the sandstones. The P_2O_5 diagram (fig. 7*i*) shows considerable scatter but two linear trends are apparent, one for the sandstone at higher SiO_2 and one for the siltstone and mudstone at lower SiO_2 content. This may provide a means of distinguishing between the SDpq and the Scamander Formation and SDpd which have similar P_2O_5 signatures. The phosphorus may be partitioned in apatite, the presence of which has been suspected in the sandstones but not detected by X-ray diffraction studies. The very low CO_2 values in the analyses (range 0 to 1.4 wt%) suggests insignificant biogenic influence, although there is a tendency for mudstone from the SDpq to have slightly higher values which may indicate a minor calcareous biogenic input.

The A-CN-K diagram of Nesbitt (2003) shows that the sandstone and siltstone lie along the weathering trend for an average granite and have CIW values of about 80 (fig. 6*b*). The rocks do not seem to have undergone further advanced weathering which would have resulted in a trend towards kaolinite with resultant breakdown of feldspars. This is consistent with the observation that plagioclase is common in many sandstones and rare grains of fresh microcline and K-feldspar with Carlsbad twinning have also been recorded. This clearly shows that detrital feldspars survived weathering and transport from the source area. This has an important bearing on arguments presented below.

PAAS normalised spider diagrams

Berry *et al.* (1997) studied sediments associated with the three depositional cycles of the Mount Read Volcanics. Using PAAS (Post-Archean Australian Shale) normalised trace element and major element diagrams they recognised various degrees of mixing of volcanogenic detritus as well as inputs from compositionally mature basement terrains. PAAS represents an average granodiorite, thus normalised samples with a positive slope to the right reflect source rocks with mafic characteristics whereas those with a negative slope to the left indicate more felsic compositional inputs (Berry *et al.*, 1997). In addition, spikes and troughs of individual elements may indicate detritus from particular terrains. For example, positive Cr and Ni spikes may suggest clastic material from mafic-ultramafic complexes. This approach was adopted for the Mathinna sediments in the project area.

PAAS normalised diagrams for sandstone, siltstone and mudstone are shown in Figure 8*a–c*. Patterns are broadly similar, with flat normalised values clustering around one and a similar disposition of positive and negative spikes. In the case of the mudstones (fig. 8*c*) this is significant as it suggests that they are part of the turbidite package rather than being products of pelagic deposition. They were probably deposited from late-stage diluted fractions of the turbidite flows. The Scamander Formation sandstones plot at the bottom of the normalised traces (fig. 8*a*) because the abundant quartz (up to 80%) dilutes the other elements but the characteristic positive and negative spikes are retained. Each of the patterns show positive spikes for Zr and Y and negative spikes for P_2O_5 and to a lesser extent TiO_2.

There are subtle differences between the three rock types which probably reflect the fact that minerals such as zircon, which have an abundant trace element content, are selectively concentrated in the sandstones due to their higher specific gravity. For example, the sandstones have a strong positive spike for Zr which weakens with decreasing grainsize. Sandstones also have a positive spike for Y which appears to persist into the finer-grained rocks. This is undoubtedly related to the presence of zircon but this

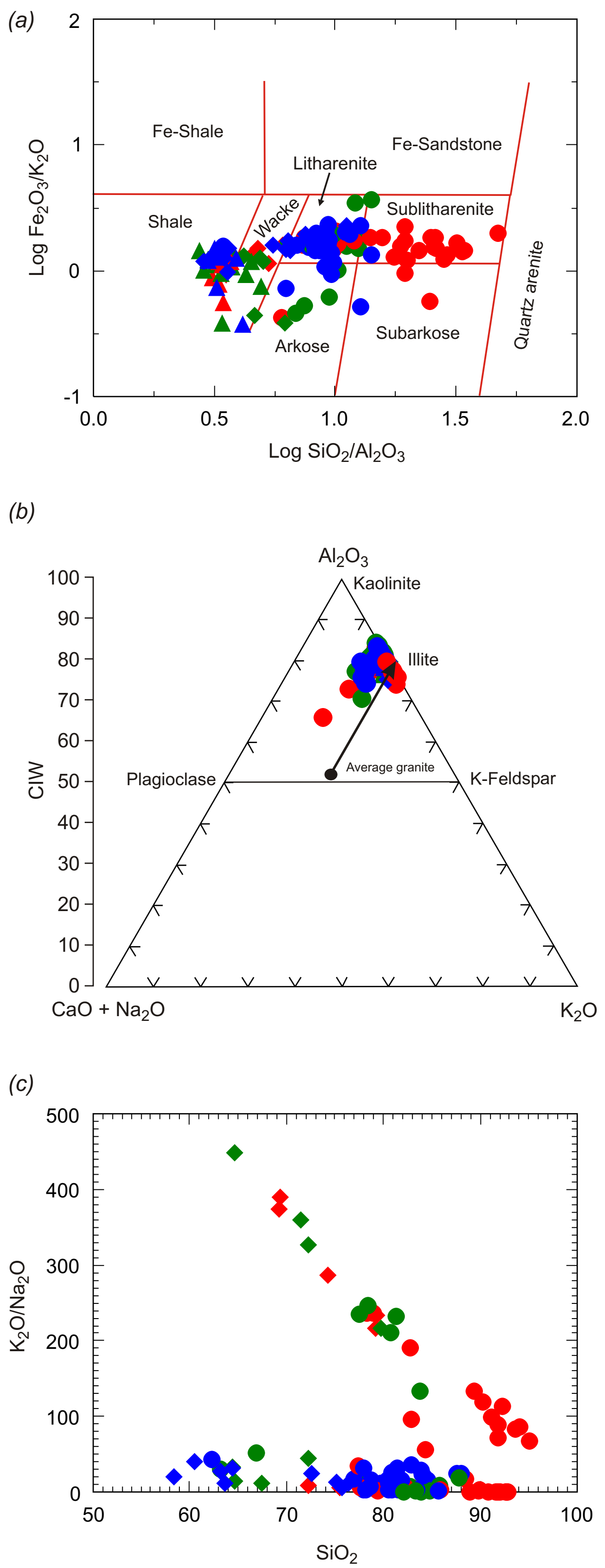

Figure 6

(a) Sediment classification diagram after Herron (1988).

(b) Triangular plot of wt% Al_2O_3–(CaO^*+Na_2O)–K_2O (Nesbitt, 2003) for sandstones only. All analyses have very low CO_2 so wt% CaO is assumed to equal CaO^* (the CaO content of silicates). Chemical Index of weathering plotted on y axis.

(c) Plot of K_2O/Na_2O vs SiO_2. Symbols: sandstone (circles), siltstone (diamonds), mudstone (triangles). Dpsf Scamander Formation (red), SDpq (green) and SDpd (blue).

element also partitions in tourmaline which is common in the sandstone and siltstone (Deer *et al.*, 1992). All rock types have a strong negative spike for P_2O_5. V shows a negative spike in the sandstones only and there is a strong negative spike for Ni, particularly in the mudstones. There is also a weak positive spike for Cr in the mudstones which could be caused by rutile which may contain significant Cr in its lattice (Deer *et al.*, 1992). X-ray diffraction of the mudstones showed that rutile is a common phase.

The patterns described above are similar to some of those documented by Berry *et al.* (1997) from sediments associated with the Mount Read Volcanics, in particular those from the Stitt Quartzite. Berry *et al.* (1997) concluded that such patterns are characteristic of sediments where the principal detrital input is from compositionally mature basement sources lacking contribution from basaltic or felsic volcanic rocks.

K_2O/Na_2O ratios

A plot of K_2O/Na_2O against SiO_2 for sandstone and siltstone shows some interesting relationships (fig. 6*c*). The samples divide into two sets; one consisting of some of the sandstones and siltstones of the Scamander Formation and the SDpq. These show a relatively high ratio with a linear negatively sloping trend. The other set, which consists of the remainder of the Scamander Formation, the SDpq and all of the SDpd shows a very low ratio and a flat trend. In two localities, where multiple samples were collected, rocks with both ratios were present but in each case one ratio was dominant.

In order to investigate this observation further, the composition and approximate mineral content of eighteen of these rocks were studied by X-ray diffraction. Samples from logs 3, 4, 5 and 6 of Powell *et al.* (1993) were included. An average mode for each mineral was calculated using the means of the modal percentages. The results are shown in the histogram (fig. 9*a*). Samples with a high K_2O/Na_2O ratio contain kaolinite but plagioclase is rare or absent. Samples with a low K_2O/Na_2O ratio contain plagioclase, vermiculite and chlorite. Very little kaolinite is present (in only one sample) but halloysite is present in two samples from log 4. K-feldspar was not detected by X-ray diffraction but line overlaps with rutile may have obscured its presence. Paradoxically, the low K_2O/Na_2O rocks contain more mica than the high K_2O/Na_2O group. This is probably related to the higher proportion of phyllosilicate-rich matrix. Samples with the high K_2O/Na_2O ratio also show a linear relationship between whole rock wt% K_2O and modal % mica (fig. 9*b*) and modal % kaolinite (fig. 9*c*), suggesting that the potassium is hosted in both the mica and the kaolinite. Kaolinite may contain up to 0.51 wt% K_2O (Deer *et al.*, 1965, 1992). These data are broadly supported by petrographic study of sandstones that were not analysed by X-ray diffraction. The two groups can be recognised qualitatively by correlating the presence or absence of modal plagioclase with the K_2O/Na_2O ratio.

The origin of the kaolinite in the high K_2O/Na_2O group is important in understanding the significance of the chemical differences described above. Kaolinite can be produced by *in situ* breakdown of feldspars, muscovite and other Al-rich

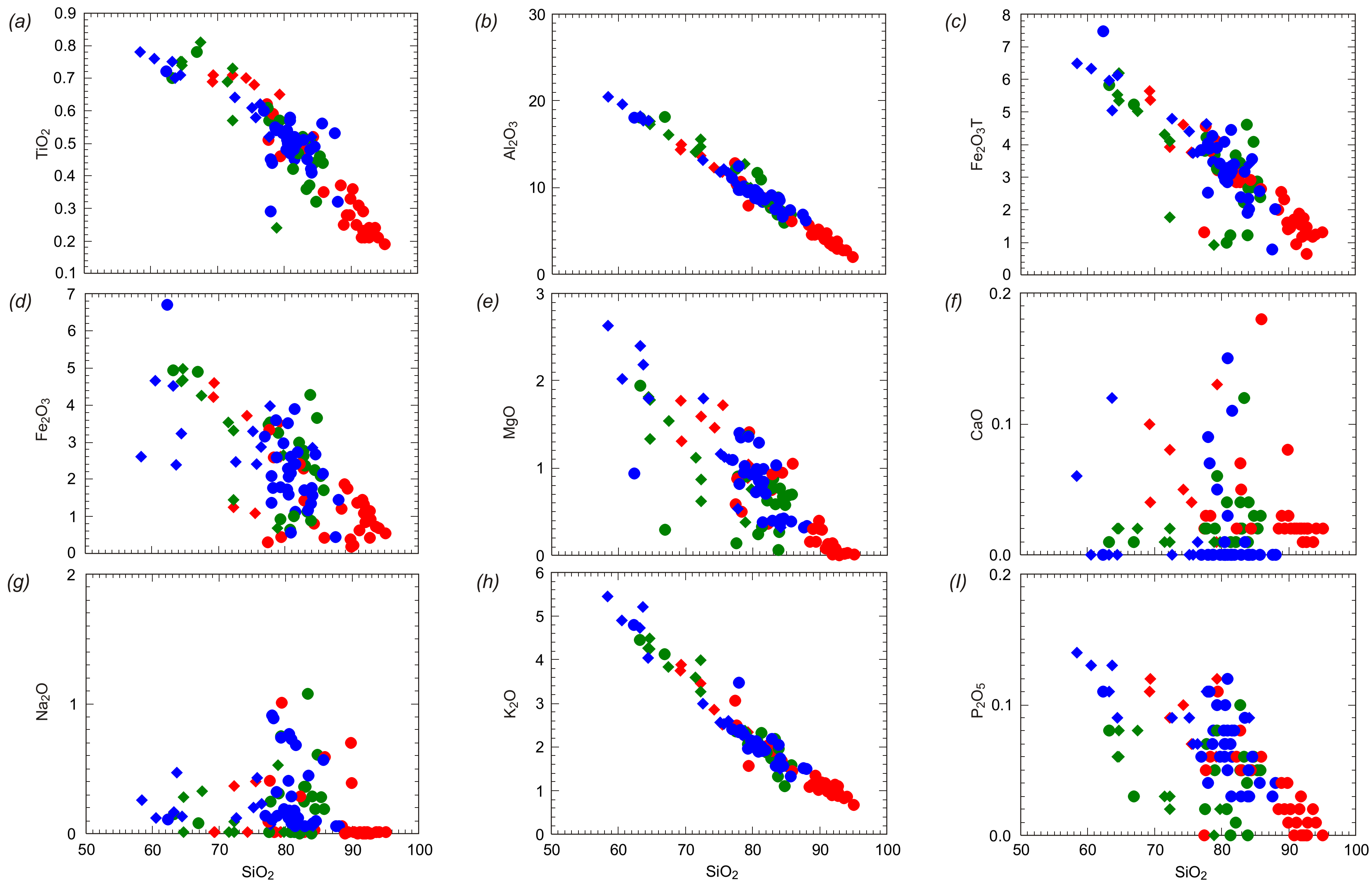

Figure 7

Variation diagrams of wt% oxide plotted against wt% SiO_2 for sandstone (circles) and siltstone (diamonds). Scamander Formation (red), SDpq (green) and SDpd (blue).

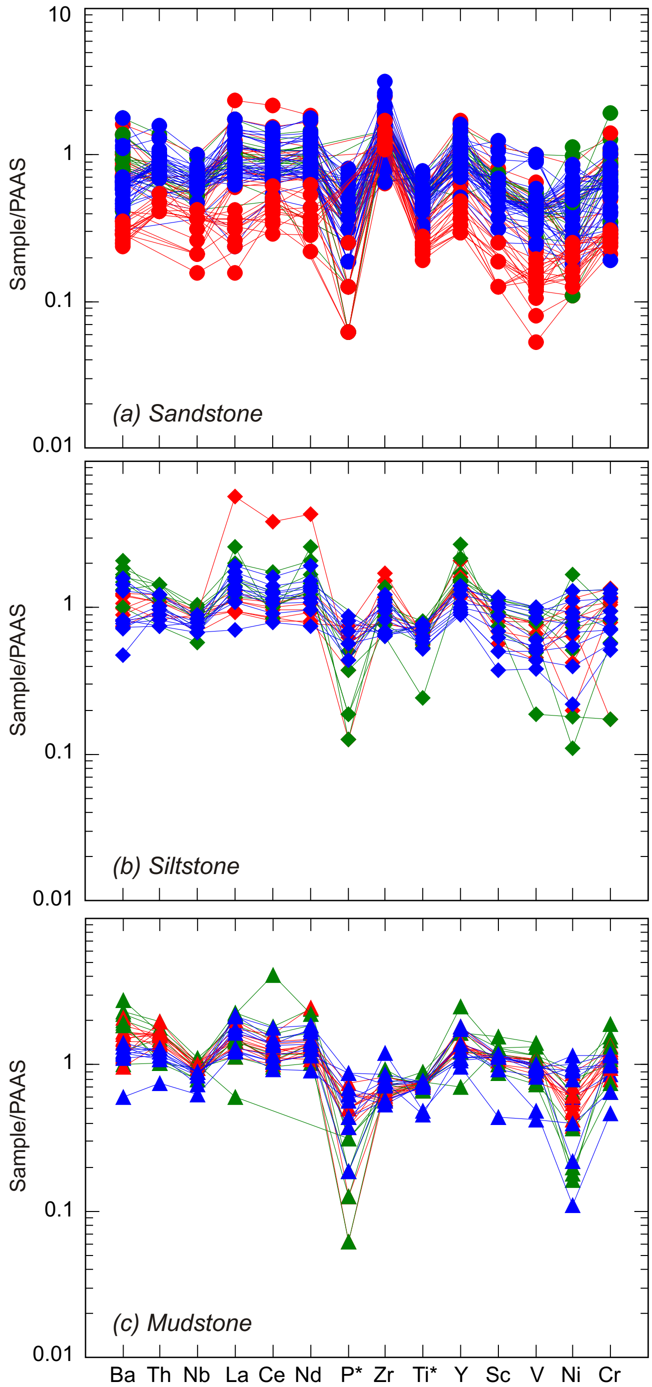

Figure 8

PAAS (Post-Archean Australian Shale) normalised trace and major elements plots of sandstone, siltstone and mudstone. Symbols as for Figure 6. P is P_2O_5 and Ti* is TiO_2.*

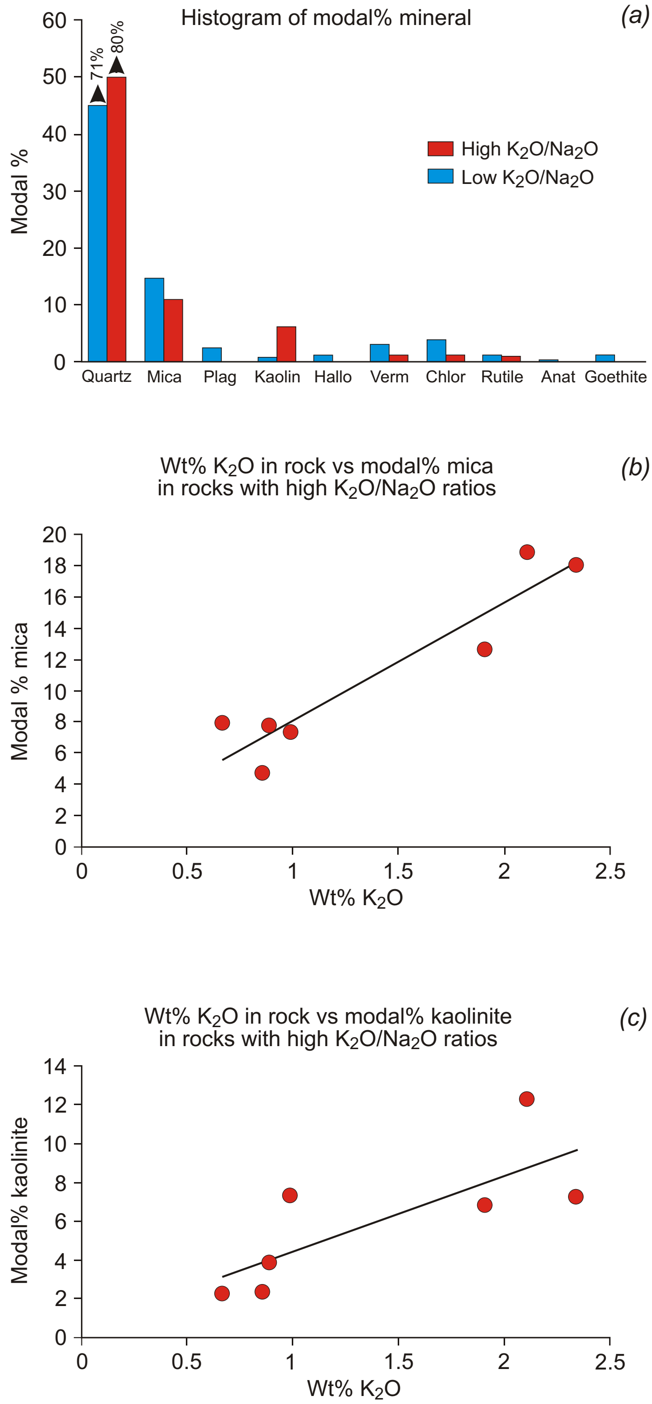

Figure 9

(a) Histogram of modal % of minerals in samples with low and high K_2O/Na_2O ratios. Mineral modes determined by X-ray diffraction.

(b) Modal % mica determined by X-ray diffraction vs wt% whole rock K_2O.

(c) Modal % kaolinite determined by X-ray diffraction vs wt% whole rock K_2O.

silicates usually in acid rocks (Deer *et al.*, 1965, 1992). In sediments it can be either detrital, formed by *in situ* breakdown of K-bearing minerals during weathering or in the transition plagioclase to K-feldspar to kaolinite or halloysite during K-metasomatism in a weathering environment (Fedo *et al.*, 1995). The presence of fresh feldspars in all groups shows that these minerals were stable in the Mathinna Supergroup sedimentary environment and during subsequent transport and weathering. It is thus concluded that the kaolinite is detrital in origin.

Summary and discussion

Table 2 shows a data summary that includes the mineral data derived from the petrography, the X-ray diffraction work and the K_2O/Na_2O ratio data. The two petrofacies based on feldspar content and the palaeoflow directions (Powell *et al.*, 1993) are also included. The K_2O/Na_2O ratio data provides additional insights into this picture. The high ratio group, exemplified by log 5, contains ubiquitous kaolinite which is absent from all other samples, although a small amount of halloysite was detected in log 4. This log also included anatase which is absent from all other samples where rutile is the main titanium-bearing phase. The most significant differences are therefore that the high K_2O/Na_2O group contains kaolinite + rare plagioclase whereas the low K_2O/Na_2O group contains plagioclase ± rare K-feldspar ± rare halloysite. It is interesting to note that many samples from the SDpd contain fresh, relatively abundant K- feldspar grains yet all K_2O/Na_2O ratios are low. It thus appears that the presence of significant kaolinite, not K-feldspar, is a marker for a high ratio.

Figure 5 shows the distribution of samples with similar K_2O/Na_2O ratios together with the palaeoflow directions (McClenaghan *et al.*, 1992). The K_2O/Na_2O data plots in linear domains that have no obvious relationship to granite contacts, suggesting that potassium metasomatism during granite emplacement was not a factor in determining K_2O/Na_2O ratios. This spatial coherence lends further credence to the authenticity of the two geochemically defined groups. South of the Orieco Fault the domains subdivide into alternating high and low ratio bands that are slightly oblique to the regional strike. The apparent sinistral displacement of the high ratio group to the north of the Orieco Fault may be due to the folds and thrusts here bringing to the surface rocks that are sedimentologically related to the high ratio band to the south and east of the fault. The known displacement on the fault cannot by itself account for the relatively large apparent sinistral displacement observed.

The domains appear to show a relationship to the zones defined by palaeoflow current directions, although this relationship is more complex than that recognised by Powell *et al.* (1993). The disposition of the K_2O/Na_2O ratio domains suggests that within the southeasterly palaeoflow domain, sediments from the two geochemically defined groups are intercalated or have been juxtaposed by thrusting. Those from the westerly domain appear to be more homogeneous. The stratigraphic order of the two palaeoflow domains is not certain, although structural considerations indicate that the westerly domain lies stratigraphically below but structurally above the easterly domain. The occurrence of domains with both low and high K_2O/Na_2O ratios in the east suggests that the two are intercalated, with one possibly enclosing the other at a regional map scale. The compositional differences described are subtle and overlapping, which is to be expected in sediments that are the product of cycles of erosion, transport and deposition followed by *in situ* weathering. Perhaps the most significant observation is the distinctive differences in feldspar and kaolinite content between the two groups.

In summary, the geochemical and mineralogical data tentatively suggest the possibility that the Mathinna sandstones were derived from two provenances with subtly different mineralogies. The abundant monocrystalline quartz, plagioclase and K-feldspar, together with micas and accessory zircon and tourmaline, suggest that these terrains were dominantly granitic (Berry *et al.*, 1997). There is no simple relationship between palaeoflow directions and mineralogy but the balance of evidence suggests that sediments from the two inferred provenances are interbedded or juxtaposed by thrusting.

Provenance studies

The provenance of the Mathinna Supergroup sediments has been a matter of some debate. Sr isotopic studies by Gray and Webb (1995) and structural studies by Reed (2001) have suggested that they were derived by erosion of the Neoproterozoic to Early Palaeozoic Delamerian mountain chain. Uplift and erosion of Delamerian sedimentary and igneous rocks shed detritus eastwards into a turbiditic basin adjacent to a passive continental margin. This is supported by age patterns in detrital zircons which are dominated by Late Neoproterozoic and Early Palaeozoic ages (Black *et al.*, 2004). These sediments were subsequently deformed in the Lachlan Orogenic Belt (Foden *et al.*, 2002).

A number of authors have devised geochemical diagrams which attempt to discriminate between turbidite sandstones and argillites derived from different volcano-sedimentary provenances (Roser and Korsch, 1986, 1988) and plate tectonic settings (Bhatia, 1983; Bhatia and Crook, 1986; Bahlburg, 1998; Armstrong-Altrin *et al.*, 2004). These studies were based on analysis of ancient sediments from well-defined provinces and in some cases, on study of sediments from known modern tectonic environments. The authors used a combination of Harker variation diagrams and discriminant function analysis to characterise different provinces and tectonic settings. These studies suggest that this may be a useful approach in investigating the provenance of the Mathinna Supergroup.

Bhatia (1983) attempted to define the tectonic environment of sediments using major element plots and discriminant function analysis. He observed that passive margin sandstones are generally enriched in SiO_2 and depleted in Na_2O, CaO and TiO_2, consistent with their highly recycled and mature nature. Mathinna sandstones plot in the passive margin fields on his discriminant function diagram (fig. 10*a*). Roser and Korsch (1986) described four sediment provenance groups from New Zealand based on their mineralogical and geochemical compositions. Using a whole rock K_2O/Na_2O vs SiO_2 diagram (fig. 10*b*) on both sandstones and argillites, they characterised sediments into different provenances. They also showed that similar protolith volcanic rocks plot in the same fields on the diagrams as the derived sediments (Roser and Korsch, 1986). They concluded that protolith geochemistry is reasonably accurately reflected in the derived sediments particularly where there are minimal biogenic calcareous and siliceous components. Using their diagrams, the Mathinna sediments plot in the passive margin field (fig. 10*b*) (Roser and Korsch, 1986) and the quartzose igneous province field (fig. 10*c*) (Roser and Korsch, 1988).

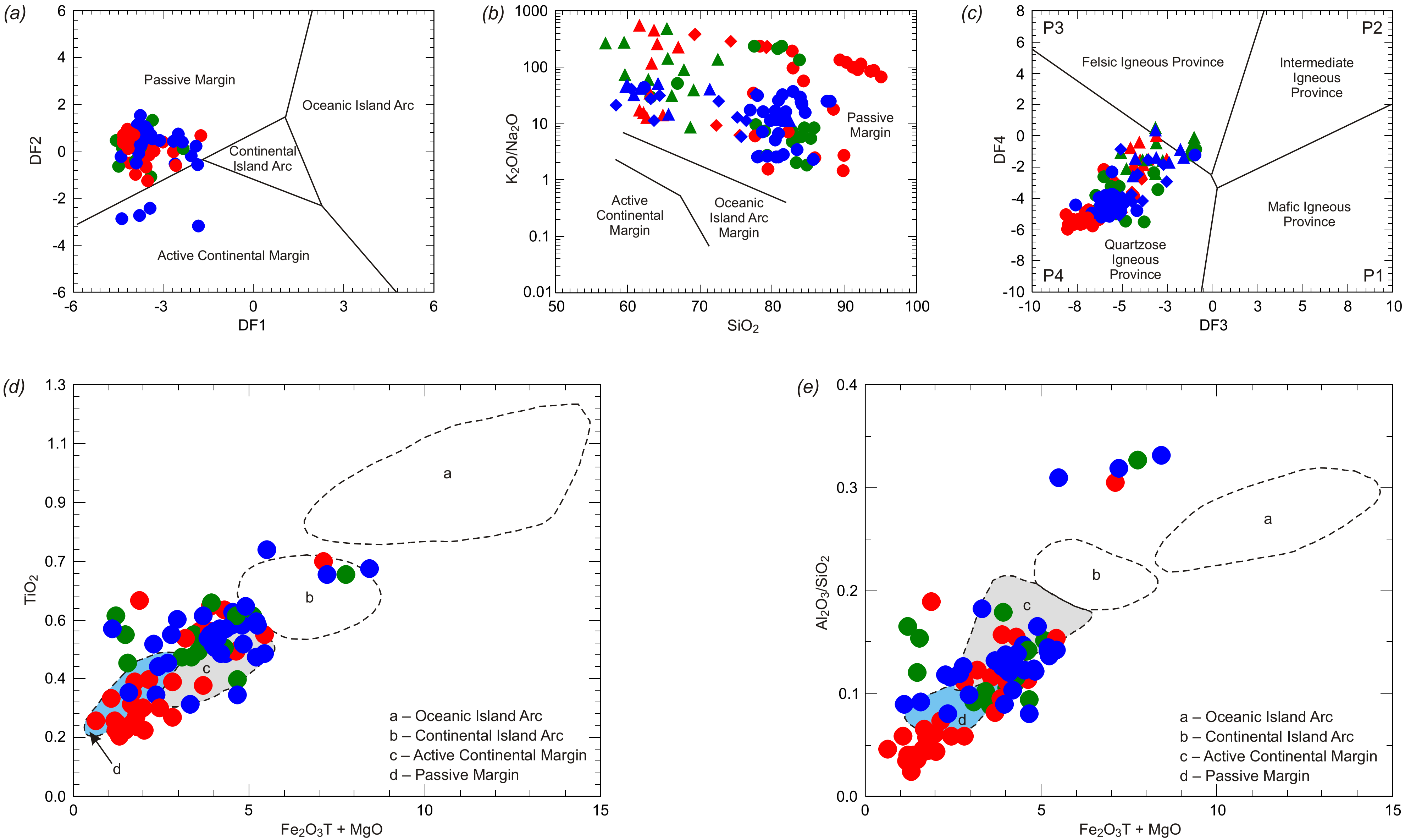

Figure 10

Provenance discriminant diagrams. (a) Discriminant Function diagram for tectonic provenance after Bhatia (1983). (b) Tectonic provenance discriminant diagram of K_2O/Na_2O vs SiO_2 after Roser and Korsch (1986). (c) Discriminant Function diagram for sediment provenance after Roser and Korsch (1988). (d) Tectonic discriminant diagram of TiO_2 vs $Fe_2O_3T + MgO$ after Bhatia (1983). (e) Tectonic discriminant diagram of Al_2O_3/SiO_2 vs $Fe_2O_3T + MgO$ after Roser and Korsch (1988). Symbols as for Figure 6.

Bhatia (1983) and Roser and Korsch (1988) also used major element plots to define provenance. Figures 10*d* (Bhatia, 1983) and Figure 10*e* (Roser and Korsch, 1988) show examples and in each case the Mathinna Supergroup sediments, although showing some scatter, mostly plot in the passive margin fields. Bhatia and Crook (1986) used immobile trace elements such as La, Ce, Nd, Th, Zr, Nb, Y, Sc and Co in their discriminant diagrams. The Ti/Zr vs La/Sc, La/Y vs Sc/Cr and Th-Sc-Zr/10 diagrams give a scattered fit for the passive margin field for the Mathinna sandstones and siltstones.

In summary, the above data suggest that the Mathinna sandstones were derived from a quartzose igneous province consisting of two possible sources which were broadly granitic in composition. The sediments were deposited in a turbidite basin adjacent to a passive margin. PAAS normalised diagrams also suggest that the Mathinna sediments were derived from compositionally mature basement sources lacking significant contribution from basaltic or felsic volcanic rocks. Turbidite lobes from these two provenances may be intercalated in the Scamander Formation and the SDpq. These conclusions are consistent with the work of Gray and Webb (1995) and the structural studies of Reed (2001).

Metamorphism

Patison *et al.* (2001) conducted an east to west illite crystallinity survey across the entire outcrop of the Mathinna Supergroup. Their data suggest a decrease in temperature from west to east from borderline epizonal conditions (>300°C) in the west to dominant anchizonal conditions in the east (200–300°C), including in the project area. X-ray diffraction studies and petrographic studies indicated that muscovite is a common phase in the rocks across the whole project area, with the petrographic studies suggesting that most is detrital in origin. There is a distinct change in the intensity of S_1 across the area. It is poorly developed in the east but in the west S_1 is penetrative and many pelitic rocks are phyllitic in appearance. X-ray diffraction of selected pelitic rocks across the area suggested that there were no structural differences in the muscovite present although Patison *et al.* (1994) showed that there is a close correlation between the b_0 lattice parameter for muscovite and the illite crystallinity index along the Avenue River west of the Catos Creek Dyke. They concluded that anchizonal temperatures in the lower pressure range of the intermediate pressure facies series prevailed across this zone. This implies minimal metamorphic recrystallisation.

Igneous geochemistry

A regional dolerite dyke swarm was intruded into the Mathinna sediments and the Devonian granites during the Carboniferous (Mid-Mississippian). This is based on a recent $^{40}Ar/^{39}Ar$ date on a dyke from southwest of Ansons Bay which yielded an excellent plateau age of 330.2 ± 5.6 Ma (McClenaghan and Everard, in prep.). The dykes are generally not well-exposed but their presence is defined by strong regional magnetic linears (Leaman, 2008). A regional study by McClenaghan and Everard (in prep.) divided the dykes into two groups. Group I dykes are clearly tholeiitic

Table 3

Analytical data for dolerite dyke at 601 181 mE, 5 416 629 mN.

Oxide	*Wt% Oxide*
SiO_2	48.86
TiO_2	2.92
Al_2O_3	13.51
Fe_2O_3	3.27
FeO	10.50
MnO	0.22
MgO	4.72
CaO	6.68
Na_2O	3.15
K_2O	1.70
P_2O_5	0.57
SO_3	0.04
CO_2	0.20
H_2O	3.05
Total	**99.69**
LOI	2.08
FeO_T	13.44
Fe_2O_{3T}	14.94

Trace elements	*(ppm)*
Th	18
Sr	510
U	10
Rb	83
Y	56
Zr	250
Nb	10
Mo	5
Cr	11
V	380
Sc	31
Co	48
Ga	23
Zn	175
W	10
Cu	19
Ni	18
Sn	9
Pb	11
Ba	470
La	20
Ce	55
Nd	36
P	2 486
K	14 113
Ti	17 505

on an AFM plot and show a linear trend with decreasing MgO on an FeO_T/MgO vs MgO diagram. Group 2 overlap into the calc-alkaline field on an AFM diagram and show a scattered pattern at lower MgO values on the FeO_T/MgO vs MgO diagram. McClenaghan and Everard (in prep.) conclude that the dykes crystallised from a tholeiitic magma that was subjected to varying amounts of olivine and pyroxene fractionation, with the variability of Group 2 being attributed to assimilation of crustal material.

A dolerite dyke crops out along the line of the Orieco Fault at 601 181 mE, 5 416 629 mN. In thin section the rock is medium grained, holocrystalline and hypidiomorphic in texture and there is no evidence of flow alignment of the prismatic minerals. It is dominated by interlocking subhedral laths of plagioclase which are clouded by alteration, making Michel Levy determinations inconclusive. Intergranular anhedral clinopyroxene comprises about 10% of the mode and is locally uralitised. The groundmass is peppered by anhedral granular to skeletal opaque minerals. Anhedral, granular, interstitial quartz is also present in small amounts.

Table 3 shows an analysis of this rock. The dyke plots in the basalt field on an alkali-silica diagram and in the tholeiite field on an AFM diagram. Figure 11 shows the field defined on a chondrite normalised (Thompson, 1982) trace element plot of Group 1 dykes from the regional study of McClenaghan and Everard (in prep.). Superimposed on this field is the plot of the dyke represented in Table 3. It is clear that this rock is similar in its trace geochemistry to Group 1. The HFS elements show a flat pattern clustering around seventy times chondrite. The hydrothermal alteration is reflected in the significant LOI value (2.08 wt%) in a rock which in its unaltered condition would be anhydrous. This is probably responsible for the variability shown by the LILE.

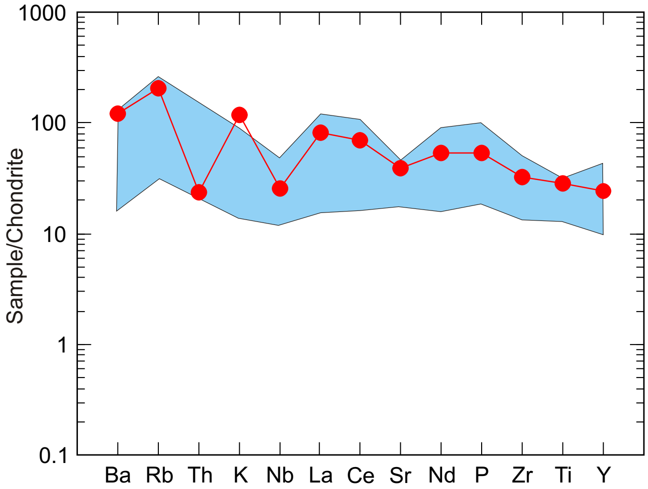

Figure 11

Chondrite normalised (Thompson, 1982) trace element plot of dolerite sample from the Orieco Fault along Cramps Road at 601 181 mE, 5 416 629 mN. The blue field is that of all analysed Group 1 dolerites from northeast Tasmania as defined by McClenaghan and Everard (in prep.).

The vertical and lateral variability of the Mathinna Supergroup turbidites has meant that the identification of mappable lithological units has been difficult. This has made structural interpretations more problematic. Geophysical and remote sensing techniques have thus proved to be valuable aids in interpretation. In the following section each technique is illustrated by a map covering the same area as the location map (fig. 1). The radiometric diagram (fig. 16) covers a slightly smaller area because the dataset is incomplete in the west.

Aeromagnetics

Regional magnetic data for northeast Tasmania was acquired by Mineral Resources Tasmania in 2007 using a combination of fixed wing aircraft and helicopters flying east to west traverses at 200 metre intervals with a nominal terrain clearance of about 80 metres. Data interpretation was done by Leaman (2008) with further in-house processing by MRT. The tilt angle derivative (TDR) proved to be of particular interest. Magnetic derivatives show the rate of change of the magnetic field in the vertical (Z) and horizontal directions (X, Y). Vertical derivatives enhance high frequency gradients such as narrow features that are usually associated with shallow magnetic anomalies. In contrast the horizontal derivative for a given direction (X or Y) will enhance linear features which trend at 90° to that direction, while diminishing those that lie parallel to that direction. The TDR is an amplitude-normalised derivative that enhances large and small-scale amplitude anomalies. Positive TDR responses indicate features above a source, with zero responses indicating the edge of a source. The TDR is used primarily for mapping the continuity of shallow structures.

Figure 12 shows a TDR diagram for the project area. One of the striking features of this image is the number of northeast to southwest-trending linear anomalies which Leaman (2008) modelled as dykes. These are part of a regional dyke swarm that intruded during the Carboniferous (McClenaghan and Everard, in prep.). One of these dykes parallels the trend of the Orieco Fault which clearly displaces the outcrop of the Scamander Tier Dyke and the Catos Creek Dyke (McClenaghan *et al*., 1992). Another similar magnetic lineament occurs to the southeast. Dykes have been observed in outcrop along both lineaments, one along the trace of the Orieco Fault (at 601 181 mE, 5 416 629 mN) and another at the Great Pyramid mine site (at 599 557 mE, 5 413 234 mN) (Groves, 1972).

It is apparent that the coherence of the magnetic signature changes across the northeast to southwest-trending lineaments. To the northwest, particularly around 596 000 mE, 5 416 000 mN, tight arcuate structures strongly suggest the presence of folds. These features appear to be offset in a sinistral sense at about 594 500 mE, 5 416 300 mN, which is consistent with the sinistral strike-slip movements along the Orieco Fault. The presence of these folds has been confirmed by mapping along Granite Knob Road immediately east of the Catos Creek Dyke and also in the Avenue River (Worthing and Woolward, 2010*a*). This lends credence to a similar interpretation of anomalies further to the east where structural data is either sparse or absent. The arcuate structures are lost in magnetic noise to the south of the Orieco Fault. Similar structures also occur west of Beaumaris (at 604 500 mE, 5 414 000 mN); Leaman (2008) modelled these as synclinal folds.

Another striking feature of the TDR is the presence of a strong NNE-trending linear anomaly along Trout Road. This anomaly is truncated and apparently offset in a sinistral sense by the Orieco Fault. The anomaly was noted by Duffet (1992), who referred to company exploration work which modelled part of it as a tabular magnetic body limited in strike with a depth to top of around 70 metres and an apparent magnetic susceptibility equivalent to 0.5% magnetite. Drilling intersected a weakly pyrrhotite-veined system which is considered to explain the anomaly. Structural mapping has shown that pelitic rocks are common in this zone, dips are steep, and there is evidence of shearing. The zone has thus been modelled as a thrust.

The signature associated with the Scamander Tier and Catos Creek dykes suggests that these rock types are less magnetic than might be expected from a granodiorite-adamellite suite. They are certainly less magnetic than the enclosing Mathinna sediments. Using combined gravity and magnetic profiles, Duffet (1992) produced a contour map of the subsurface granite-sediment interface. This surface deepens from northeast to southwest across the area. This may partly explain the coherent magnetic signature in sediments to the north discussed above. Here the sediments are relatively close to the granite contact such that metamorphic reactions, probably in the pelites, have enhanced the magnetic signature thus revealing the folds referred to above. This is supported by magnetic susceptibility readings across the area which showed that pelitic rocks yield higher values than the associated sandstones. More significantly, rocks in the contact aureole yield the highest values which may be more than two orders of magnitude above background values away from the aureole. The magnetic signature of the structures west of Beaumaris, interpreted by Leaman (2008) as synclinal folds, may likewise have been enhanced by proximity to the George River Granodiorite (Duffet, 1992; McClenaghan *et al*., 1992).

The terrain west of the Catos Creek Dyke has been subdivided on structural and lithological criteria into a series of domains and subdomains (fig. 12). Domain 1 consists of the outcrop area of SDpd. The Avenue River Fault Zone (ARFZ) is defined by domains 2 and 3 which are further subdivided into subdomains 1 to 6. Domain 4 lies to the west. These subdivisions were recognised in traverses along the Avenue River and associated creeks and will be discussed in detail later. The TDR image models a change in magnetic signature across the contact of SDpd and the ARFZ, which comprises SDpf and a significant part of SDp to the west. The magnetic texture of the SDpd is characterised by attenuated high frequency anomalies. These contrast with the extensive lower frequency, very high amplitude linear magnetic highs within Domain 2, the eastern part of the ARFZ (fig. 12). The latter anomalies are most typically associated with areas of siltstone dominance. Clear evidence of significant dextral

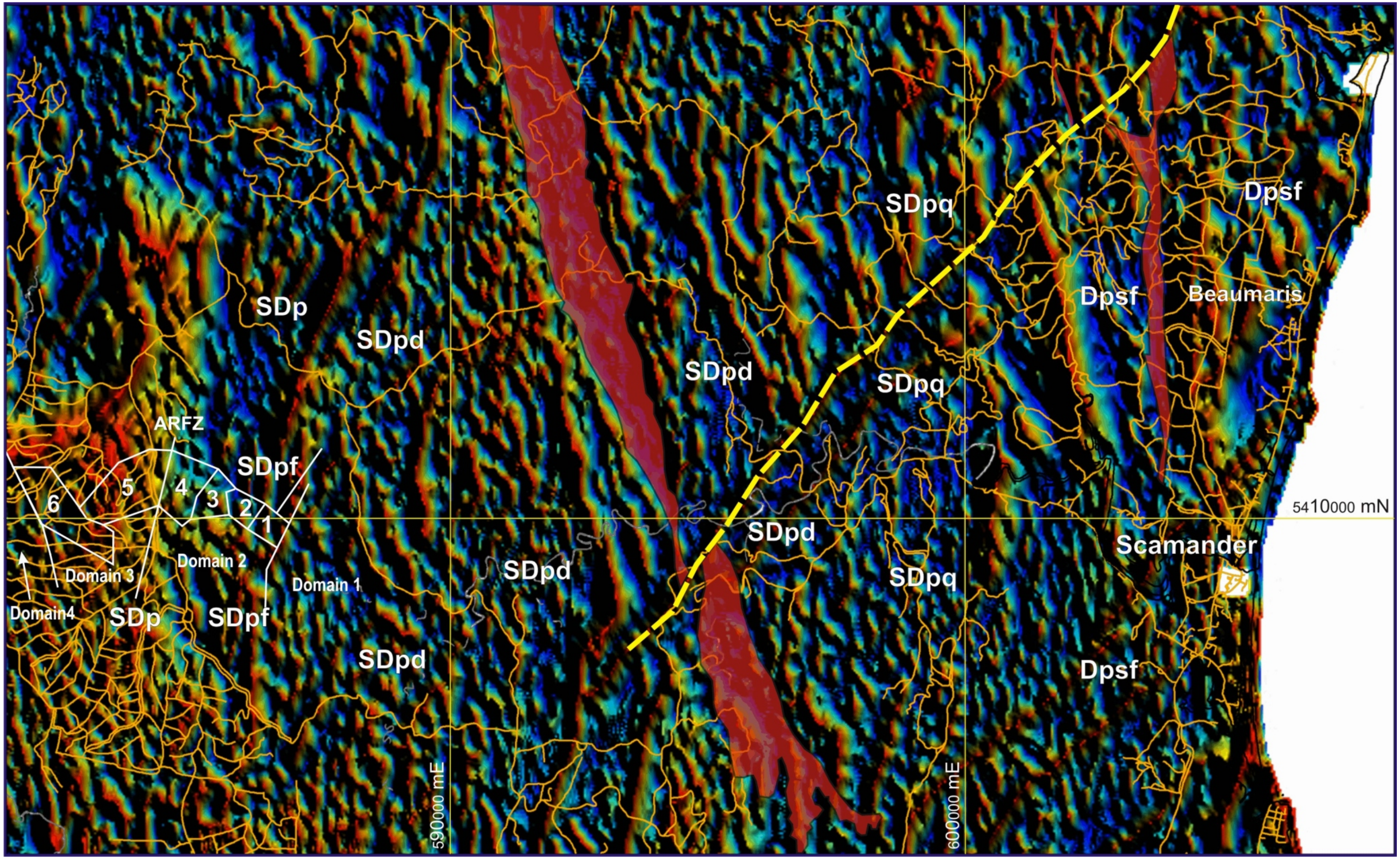

Figure 12

Aeromagnetic tilt angle derivative (TDR) map of the project area. The Orieco Fault is shown in yellow. The Scamander Tier and Catos Creek dykes are shown in red. Structural domains 1 to 4 and the subdomains 1 to 6 associated with the Avenue River Fault Zone are shown in white.

strike-slip faulting can be found in an outcrop at 587 022 mE, 5 412 450 mN which is situated on such a high amplitude anomaly. These linear anomalies probably represent faults within the less competent siltstone which dominates parts of the ARFZ. Such anomalies may have been enhanced within the SDpf by fluid penetration. Faults within the ARFZ further west of the siltstone-dominant SDpf are typically located in areas with significantly more sandstone outcrop. Such sandstones generally have lower magnetic susceptibilities and hence linear highs are less common.

Further to the west in Domain 3, a prominent broad, long wavelength, low amplitude anomaly is interpreted by Roach (1992) to represent the northern edge of a subsurface body of granodiorite with similar magnetic properties to exposed parts of the Pyengana pluton. To the north of this anomaly, Roach (1992) modelled the depth to the granite surface as 200 m below the current ground level. The high frequency anomalies in the southwest of Figure 12 are also consistent with Roach's (1992) interpretation of a granodiorite underlying the Mathinna sediments. However no spotting was observed in the Mathinna sediments over the proposed granodiorite intrusion during the course of this project.

Worms

Magnetic and gravity worms are derived from potential field data using a multi-scale wavelet-based edge detection technique. The worms depend on the existence of a magnetic susceptibility or density contrast across a geological surface or edge such as a fault plane or intrusive boundary. Their upward continuation above the ground surface is determined from potential field data in the wavelet domain and can be thought of as calculating what would be observed at higher and higher levels. The worm traces thus provide three-dimensional relative dip direction and angle on source bodies related to those edges in the subsurface.

Magnetic worms

Figure 13 shows magnetic worms for the project area. The northeast to southwest-trending dyke lineament modelled on the TDR diagram (fig. 12) is present although slightly displaced to the southeast. It is possible that the worm is modelling both the dyke along the Orieco Fault and the two dykes which are sub-parallel and adjacent to the anomaly. Steep southeasterly dips are suggested. To the northwest of the dyke lineament are two NNW to SSE-trending worms which correspond to mapped fold hinges that are also visible on the TDR image (fig. 12).

The western side of the Catos Creek Dyke is also modelled. Here the worm corresponds to the metamorphic aureole to the west of the dyke. This aureole is absent from the eastern contact of the dyke where it has been removed by faulting (McClenaghan *et al*., 1992). The worm to the north of the Orieco Fault suggests an ambiguous dip; to the west in the northern part and to the east to the south. South of the fault a shallower dip to the east is suggested. This picture is at variance with Duffet (1992) and Taylor (1992) who, based on gravity profiles, suggested a steep westerly dip for the Catos Creek Dyke. Towards the coast, the Scamander Tier Dyke is modelled although the anomaly is displaced to the east. It is interesting to note that this worm continues south of the Scamander River into unexposed ground, suggesting continuity of the dyke. The very strong NNW–SSE trending magnetic anomaly along Trout Road is also represented as a worm although slightly displaced to the east. The dip is very steep to vertical. It is possible that the displacements described above may be caused by the heat of intrusion overprinting the pyrrhotite mineralisation which caused the anomaly. This may have displaced the anomalies into zones where the primary anomaly is unaffected.

A set of north-trending worms clearly define the faulted contact of ARFZ in the west of the project area (Worthing and Woolward, 2010*a,b*). The shallowest of these worms is approximately coincident with the eastern contact of the ARFZ where Patison *et al.* (2001) recorded the only rapid change in illite crystallinity across the whole Mathinna outcrop area. They suggested that the implied change in grade indicates a post-D_1 thrusting event post-peak metamorphism. The worms have been used here to define the lateral extent of the contact between SDpd and SDp. They appear to be sub-vertical and have been deflected to the north by the affects of Devonian granodiorite and by Tertiary basalts to the south. In the absence of any exposed structure they are interpreted as representing a steep thrust along which subsequent strike-slip movement cannot be discounted. They also model the boundary between a change of magnetic intensity within the ARFZ (SDp) and the unit SDpd (fig. 12).

In the far west of the area the worms define a 'v'-shaped structure (fig. 13). No lithological distinction was observed on either side of these structures, although they coincide with the long wavelength, low amplitude anomaly interpreted above as a granodiorite intrusion (Roach, 1992). The worms also define the eastern edge of a structure interpreted as the faulted boundary between domains 2 and 3. These relationships will be discussed further in the following section. Subdomain 6 is a distinctive zone where minor fold hinges have been rotated into a vertical orientation. Its contact with Domain 4 is interpreted as a fault which appears to be associated with truncated worms. There is also a weak association between worms and dioritic enclaves within the Blue Tier Batholith in the north of the Brilliant map sheet (Worthing and Woolward, 2010*a*).

Gravity worms

The gravity worm model (fig. 14) is based on an inadequate coverage of gravity stations which may have skewed the data. The model is based on residual data from which the mantle signature has been removed. The diagram is much more difficult to interpret than the magnetic worms. The Scamander Tier Dyke appears to be modelled by an anomaly as well as some of the magnetic lineaments southwest of Scamander.

No conclusive correlations were recognised between structures, rock types and magnetic or gravity worms in the west of the project area.

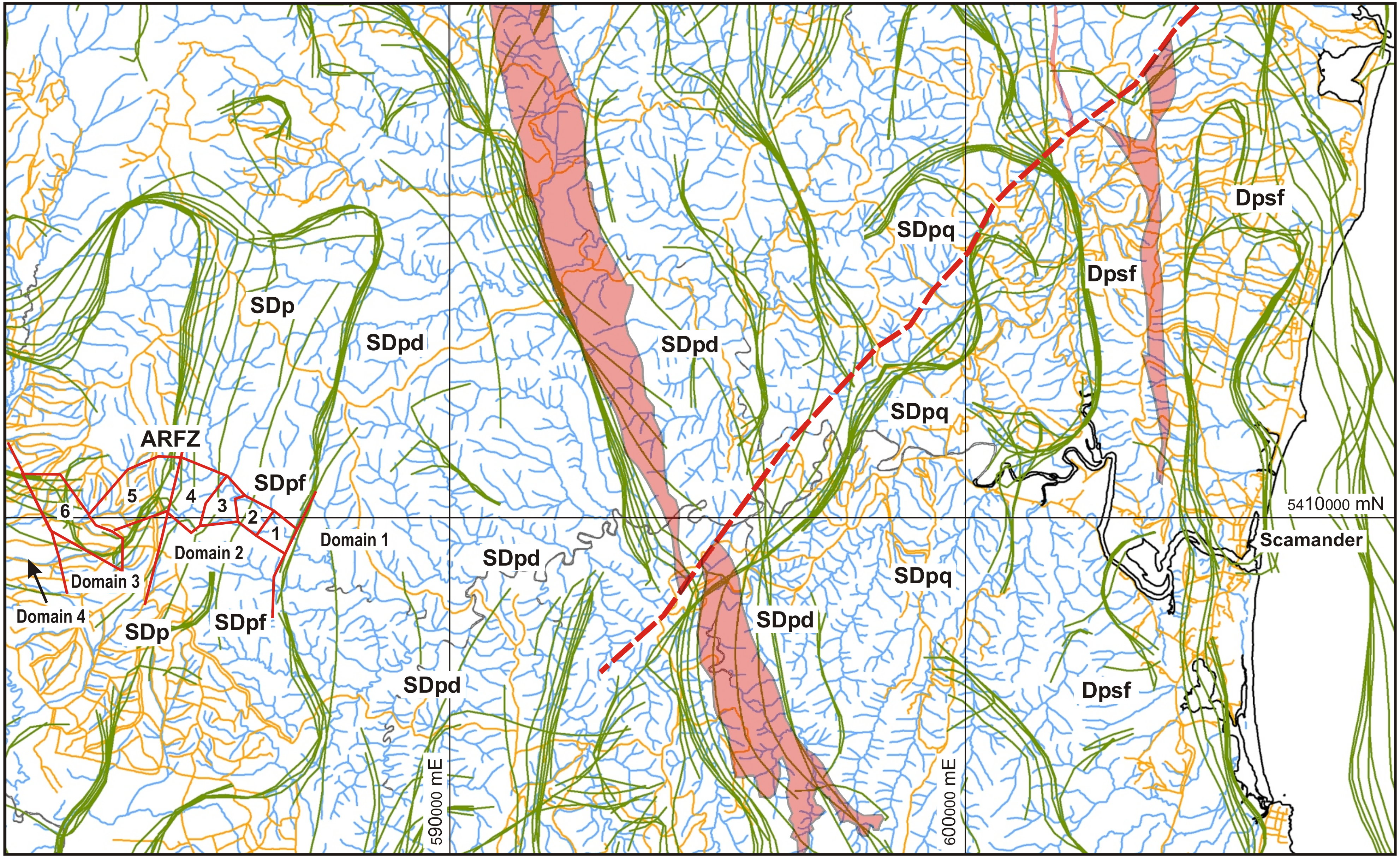

Figure 13

Magnetic worms of the project area. The Orieco Fault is shown in red. The Scamander Tier and Catos Creek dykes are in red. Structural domains 1 to 4 and subdomains 1 to 6 associated with the Avenue River Fault Zone are shown in red.

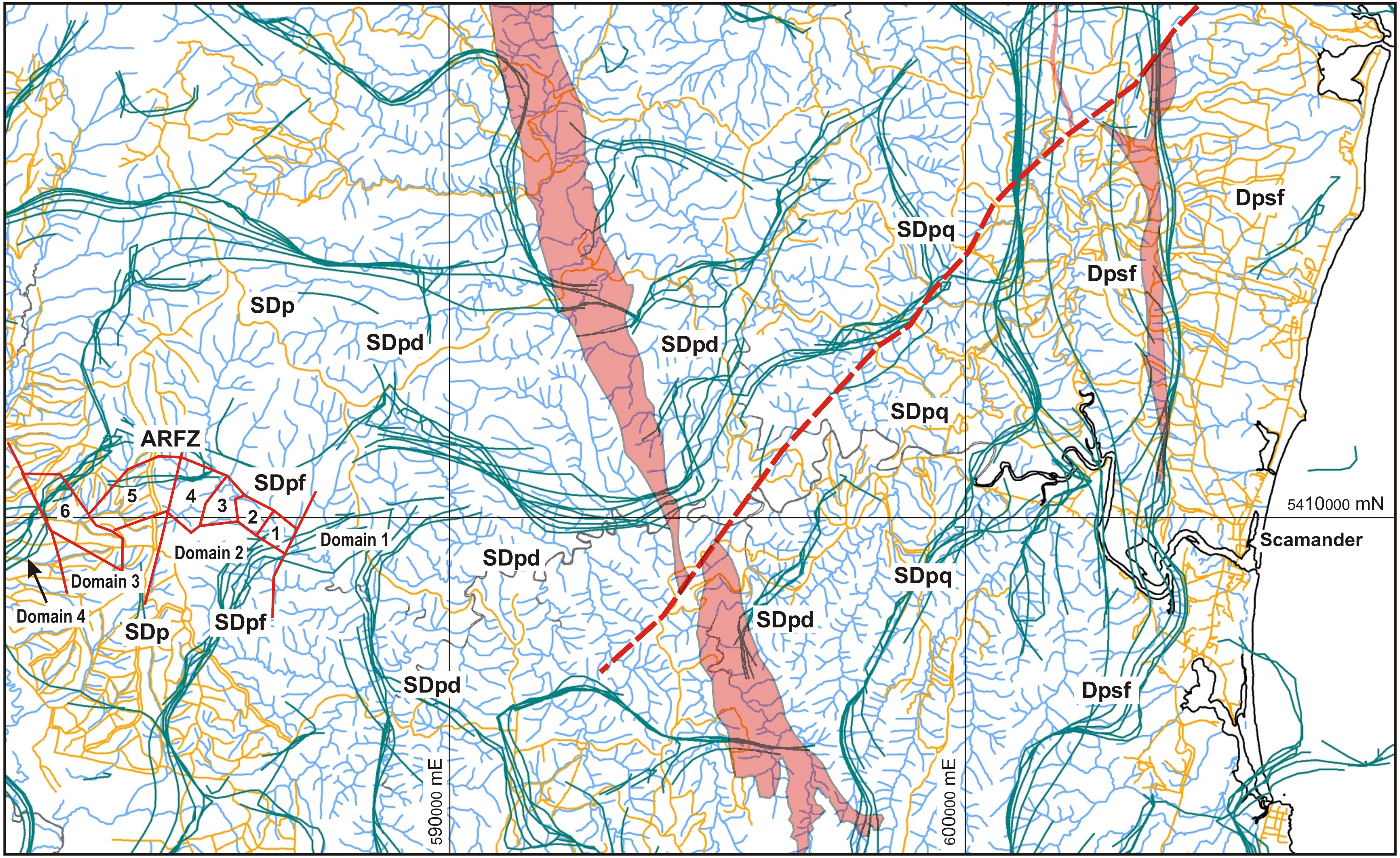

Figure 14

Gravity worms of the project area. The Orieco Fault is shown in red. The Scamander Tier and Catos Creek dykes are in red. Structural domains 1 to 4 and subdomains 1 to 6 associated with the Avenue River Fault Zone are shown in red.

LiDAR

LiDAR (Light Detection And Ranging) is a system that rapidly transmits pulses of light that reflect off landscape features, including the ground surface and tree canopy. The return pulses are converted from photons to electrical impulses and collected by a high-speed data recorder. Because the formula for the speed of light is known, time intervals from transmission to collection can be calculated. These time intervals are converted to distance based on positional information obtained from ground/aircraft GPS receivers, and the on-board Inertial Measurement Unit (IMU) that continually records the attitude of the aircraft. The LiDAR system thus collects positional (X,Y) and elevation (Z) data at pre-defined intervals. The resulting data is a very dense network of elevation postings. The accuracy of the data is a function of flying height, laser beam diameter, the quality of the GPS/IMU data, and post-processing procedures. Accuracies of ± 150 mm (horizontal) and ± 150 mm (vertical) can be achieved with a density of approximately two hits/square metre.

LiDAR data were acquired by MRT in November and December 2008 in conjunction with Forestry Tasmania. The primary data were processed from X, Y, Z point data using cubic spline interpolation at 0.5 metre resolution. The ability of LiDAR to distinguish between returns from both the forest canopy and the ground means that it is capable of producing very accurate digital elevation models (DEM). It thus has considerable potential for mapping in areas with thick vegetation cover.

In the project area, LiDAR has proved useful in recognising linear geological features such as massive sandstone strike ridges and in some cases fold structures. Figure 15 shows an oblique LiDAR image of a thickly forested area centred on 586 000 mE, 5 412 200 mN. The Parmeener Supergroup unconformity is clearly visible on the image. Prominent linear strike ridges and an apparently eastward-verging asymmetric fold are also visible in the underlying Mathinna sediments. Ground verification of some of these ridges showed that they are formed by massive sandstone benches up to three metres high that are not visible on orthophotos. Two such ridges could be traced into the Avenue River at 593 140 mE, 5 409 880 mN where the rock type could be examined in outcrop. Where these and other similar ridges could be verified in this way, they were included on the geological map as massive sandstone horizons. Unfortunately the vertical and lateral variability in the Mathinna turbiditic sediments has meant that many of these ridges cannot be traced laterally to allow delineation of major structural features.

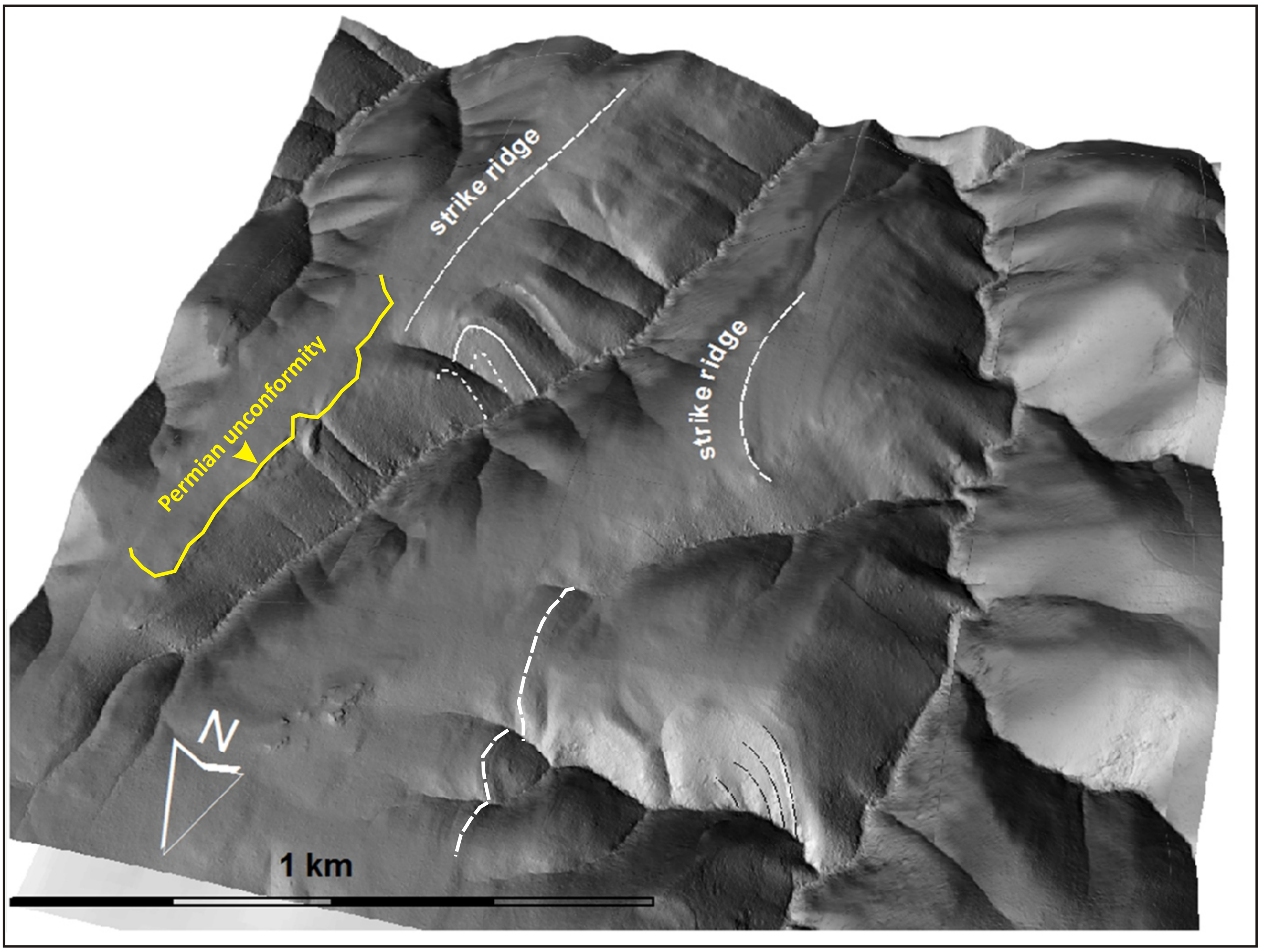

Figure 15

LiDAR image of heavily forested area, west of project area centred on 586 000 mE, 5 412 200 mN. White dashed lines are strike ridges and the yellow solid line is the Parmeener unconformity. Note the apparently eastward-verging asymmetric fold.

Other more subtle features are also evident on the DEMs. For example the outcrop of the Catos Creek Dyke is apparent from differences in surface textural features which again are not visible on the orthophotos.

Radiometrics

An airborne regional radiometric survey of the area was flown by GPX Airborne in 2007 along 200 m spaced lines with an average terrain clearance of 83 metres. Radiometric surveys measure the spatial distribution of three radioactive elements (K, Th and U) in the top 300–450 mm of the Earth's crust. The average crustal abundances of K, Th and U are relatively low at 2%, 8.5 ppm and 2.7 ppm respectively. However they are the only naturally occurring elements with isotopes that produce gamma rays with sufficient energy and intensity to be detected at airborne survey heights. Data are collected using gamma-ray spectrometers with 33 litre sodium iodide crystal detectors which record gamma-ray arrivals in 256 energy channels. Measurements are made every second which corresponds to 40–70 m along the aircraft survey track. The processed data normally comes in four bands; the gamma-ray radiation counts per second, plus gamma-ray radiation counts per second for K, Th and U. Data may be displayed in map form by combining datasets for the three elements using a red-green-blue ternary ratio. This produces a colourful display with each shade representing different relative amounts of potassium, thorium and uranium (fig. 16).

Minerals likely to host K, Th and U include the alkali feldspars, micas, apatite, zircon, rutile and possibly tourmaline which have all been recorded in the sandstone and granitoids. Figure 17*a* shows ranges of K, Th and U in three formations in parts per million (ppm). Clearly there is considerable overlap in the values and perhaps the only significant difference is that SDpq appears to have lower K and higher U than the other two formations. Figure 17*b* shows the ternary colour chart used to code the colours on the map.

Geochemical data from the project area show that there is a covariance between K and Th in the sedimentary rocks (fig. 17*c*). This diagram also shows that the abundance of these two elements increases with decreasing grainsize, suggesting that the trend may be related to the phyllosilicate content of the rocks. A similar trend is also noted for K and U (fig. 17*d*) although the uranium content of the rocks is barely above detection limits and data were available for less than half the analysed samples, and most of these are from the SDpd west of the Catos Creek Dyke (fig. 17*d*).

The granitoids show the clearest relationships between radiometric signal and rock type (fig. 16). Relative resistance to erosion, resulting in more exposed surface rock and a thinner soil cover at higher elevations, may have contributed to this clarity. For example, the Scamander Tier Dyke, the southern outcrop of the Catos Creek Dyke and the St Marys Porphyrite all show a strong K signal. Turner *et al.* (1986) and McClenaghan *et al.* (1992) reported between 3 and 4 wt% K_2O in these rocks, although the white colour that characterises the northern outcrop of the Catos Creek Dyke indicates a change in composition. This is consistent with the general variation in rock types described by McClenaghan *et al.* (1992), although their analyses show that the amount of K_2O is not significantly different from the southerly outcrop. This suggests that the change in signal is caused by changes in the relative proportions of the elements such that high K values are accompanied by higher Th and U levels in the northern part of the Catos Creek Dyke.

The sedimentary rocks are more difficult to interpret. The geochemical data suggest that sandstone should have lower levels of K relative to siltstone and mudstone (fig. 17*c*) and this should correspond to blue and green colours on the ternary colour diagram. This appears to be borne out by the relative abundance of these colours in the outcrop area of the Scamander Formation. SDpq also has higher U levels but this is based on very few analyses.

However this also appears to be modelled by the blue tones in the outcrop area of the SDpq between the Dpsf and the thrust contact of the SDpd south of the Orieco Fault. The blue signal also models the thrust wedge of SDpd which has lower U levels than the SDpq. It is interesting that the apparent displacement of this zone just east of the Catos Creek Dyke fits the sinistral sense of movement of the Orieco Fault (fig. 16).

The bluer tones are also found along the Scamander River valley and along Trout Road where they may be related to phyllosilicate-rich alluvial deposits. The Parmeener Supergroup outliers, the coastal piedmont and the lower parts of the Scamander River flood plain show dark colours indicating low concentrations of all three radioactive elements.

Immediately to the west of the Catos Creek Dyke the SDpd is characterised by mottled green with some blue, while the contiguous SDp shows yellow, with minor mottled pink and rare blue. Although geochemical analyses of SDp and SDpf are not available, the colours suggest a higher ratio of potassium and thorium to uranium in these units when compared with the SDpd to the east. In the case of SDpf this may be related to the higher proportion of siltstone in this lithology. There also appears to be a correlation between the mottled pink signatures shown by the SDp and sandstone dominated outcrops, but this relationship is not clear enough to allow its use as a mapping tool. A pink signature in the SDpf is often observed adjacent to the overlying unconformable Permian rocks that cap many ridges in this elevated area. This is interpreted as representing the signature of a veneer of Permian float covering the SDpf.

An anomalous mottled green signature characterises the relatively flat-lying terrain in the far southwest (fig. 16). Outcrop of the Mathinna sediments in this area is very poor but where present the rocks are typically very weathered siltstone, often with a distinctive pink hue in the field. A thin veneer of angular and rounded quartz grains and pebbles is scattered over the ground surface and Permian sedimentary rocks occur to the north and Tertiary sediments and basalt to the south. The thin veneer of Permian float appears to be inadequate to explain the radiometric signature. It is probable that the Mathinna sediments here were at or near the plane of unconformity prior to deposition of the Permian and possibly also the Tertiary, and were thus exposed to weathering. Surface processes therefore may have removed

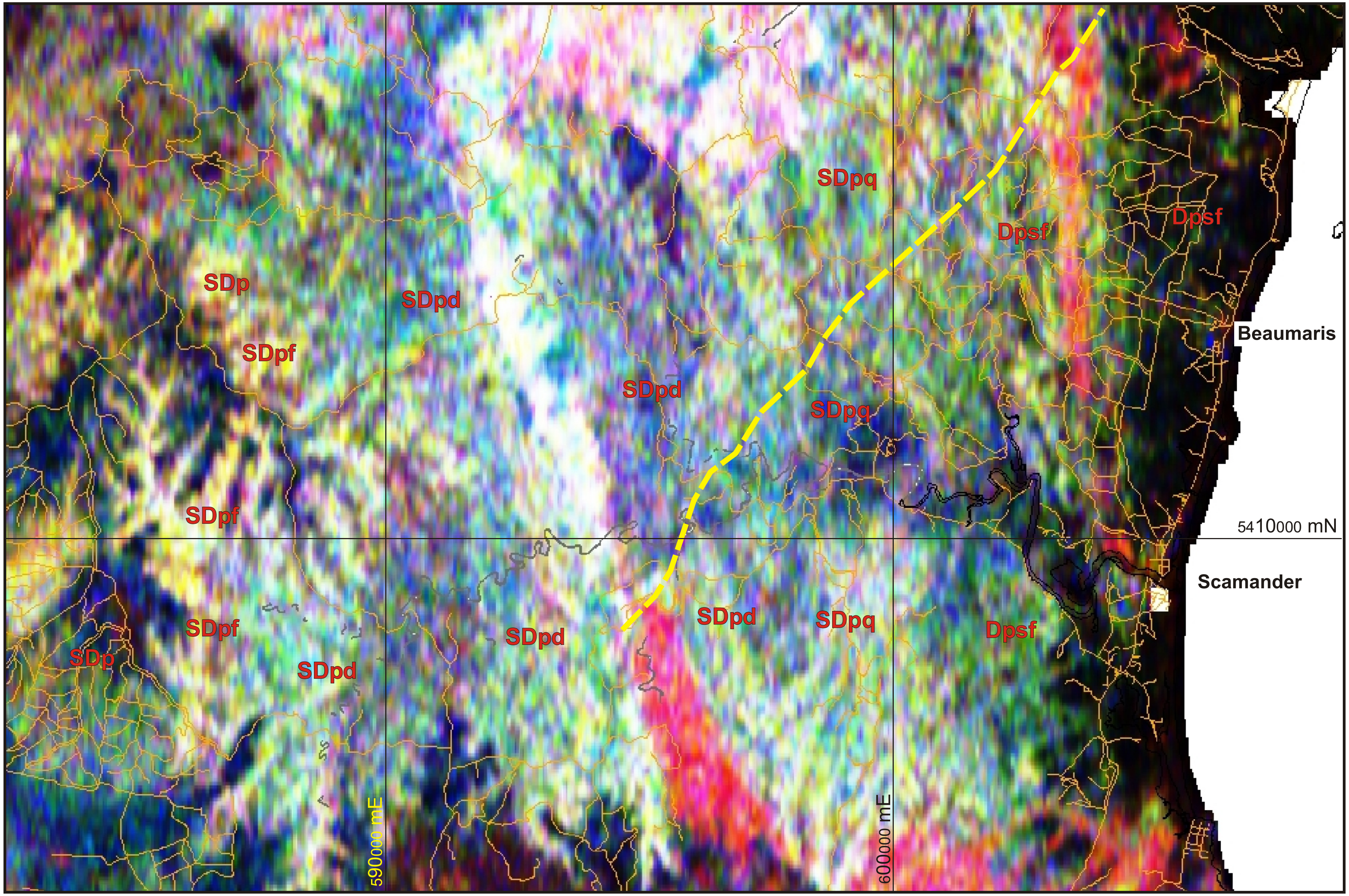

Figure 16

Radiometric map of the project area. The Orieco Fault is shown in yellow. See text for explanation. Colour scheme: (see fig. 17b). Black – low K, U, Th. White – high K, U, Th. Magenta – high K, U, low Th. Yellow – high K, Th, low U. Red – high K, low U, Th. Blue – high U, low K, Th. Green – high Th, low K, U. Cyan – high Th, U, low K.

LILE such as potassium (e.g. McQueen, 2006) resulting in the observed signal. The strong yellow radiometric signature that characterises the rest of this unit is best developed in the steep gullies around the headwaters of the Avenue River, where the rocks are being rapidly eroded and newly exposed from underneath the cap of Permian sedimentary rocks.

In conclusion, it may be said that there is some correlation between the radiometric map (fig. 16), the geochemistry and the lithologies, particularly with the granitoids, although in the case of the sedimentary rocks this correlation is not always definitive. This could partly be a function of the inadequate geochemical coverage, particularly with respect to uranium, but also the effects of surface weathering and contamination from surficial deposits such as soil and float derived from overlying rock units.

(a)

	K	Th	U
Dpsf	600–4300	5–25	1.5–2.2
Sdpq	1200–1400	9.5–27	2.2–14
Sdpd	1050–4600	9–19.5	2.5–7

(b)

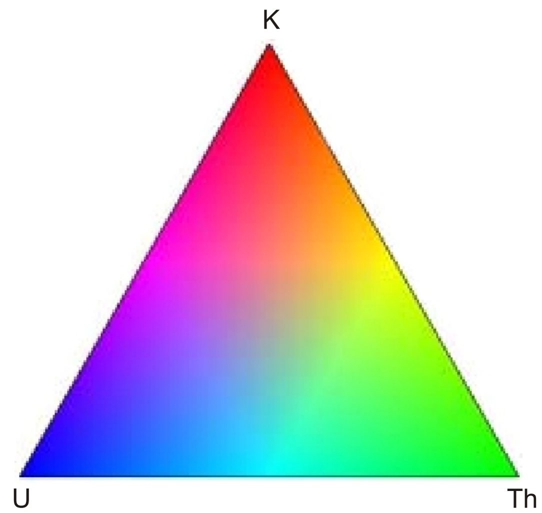

(c) (d)

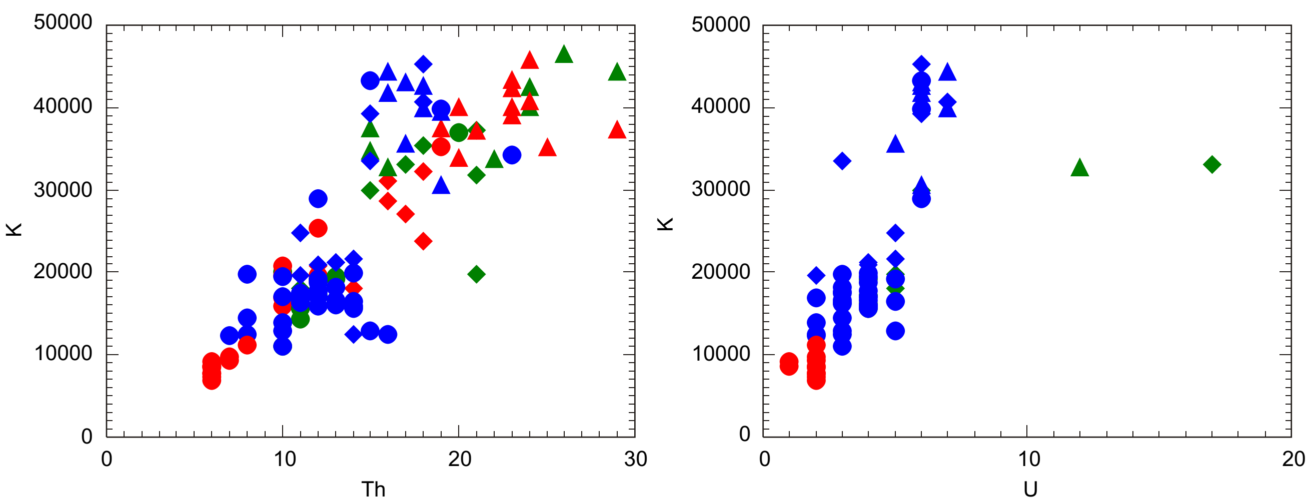

Figure 17

(a) Range of concentrations (ppm) of the elements K, Th and U for the different formations on the project area.
(b) Ternary colour chart used to colour code map (see also Figure 16).
(c) Variation diagram showing covariance of K and Th.
(d) Variation diagram showing covariance of K and U. U data was not available for all samples analysed.
Symbols as for Figure 6.

The structure of the Mathinna Supergroup in the project area will be considered within the same geographical framework adopted for the sedimentary rocks. Deformation structures will be discussed sequentially as they relate to the evolving structural history. Each phase will be denoted by a deformation phase D_N and the associated structures will be described within that framework. Bedding is denoted S_0. Folds and cleavages linked with each deformation phase will be denoted F_N and S_N respectively. Structural studies further west (e.g. Keele, 1994; Patison *et al*., 2001; Cracknell, 2009; M. Vicary, pers. comm.) have shown that there are significant differences between the structures observed in those areas and the project area, with the western part of the project area appearing to be a transition zone between these two structural domains. For this reason the deformation phases for the eastern area are not numerically chronological because an important structural event was only recorded in the west. These relationships will be clarified at the end of the section. Stereograms were all plotted with the lower hemisphere Schmidt net using Spheristat™ 2.2. Contouring uses the Gaussian K=100 method.

Eastern area

D_{1A} major structures

It is clear that the lithological divisions described in previous sections have exercised considerable control over the geometry of deformation structures. Massive sandstone tends to behave as competent slabs whereas units with a higher pelite content deform more incompetently, forming folds with chevron geometries. For example, the Beaumaris map sheet (Worthing, 2010*a*) is dominated by the sandstone of the Scamander Formation. Within this formation, massive sandstone units have imposed a broad, open fold style but within this overall package more pelitic units may fold disharmonically. Massive sandstone-pelite contacts are also used as décollement surfaces to accommodate this type of deformation. The pelite units are also the locus of much internal thrusting. Some of these relationships are illustrated by the small outcrop shown in Figure 18 which hints at some of the complexities involved in both folding and faulting in the project area.

The large scale structure of the area is represented by the three cross sections (A–B, C–D and D–E, fig. 19). These sections were compiled using field and geophysical data combined with SpheriStat™ profiles. The section locations are given in Figure 1. Sections A–B and C–D were chosen to illustrate structural differences either side of the major northeast to southwest-trending strike-slip Orieco Fault. To the west of the Scamander Tier Dyke, on the south side of the Orieco Fault, the structure within the Scamander Formation is relatively simple, consisting of a series of broad, open, inclined, east-facing F_1 folds broken by steep westerly dipping thrusts (fig. 19*b*). It is likely that the Scamander Tier Dyke was intruded along such an F_1 thrust. Immediately to the west of the Scamander Tier Dyke there is a major syncline which plunges at a low angle to the south. This is bounded on the west by a steep westerly dipping thrust which follows mudstone outcrops along Trout Road valley. These structures, and those to the east of the Scamander Tier Dyke, strike southwards into unexposed ground. To the west of the Trout Road thrust zone a hanging-wall anticline is interpreted which passes westwards into a major south-plunging syncline. This structure can be traced southwards onto the Falmouth map sheet area (Worthing, 2010*b*) where it is truncated by the basal units of the St Marys Porphyrite with strong angular unconformity, indicating that it formed prior to eruption of the porphyrite (Turner and Calver, 1987). However projection of the axial trace into the porphyrite corresponds to a zone where mylonitic fractures are common. The basal units of the porphyrite sweep round in a broad synclinal structure that is superimposed on the earlier syncline in the sediments described above. The cross sections of Turner and Calver (1987) also showed that one of the eastward-facing inclined asymmetric folds in the porphyrite has an interlimb angle of about 50° suggesting that it is the product of strong deformation. They concluded

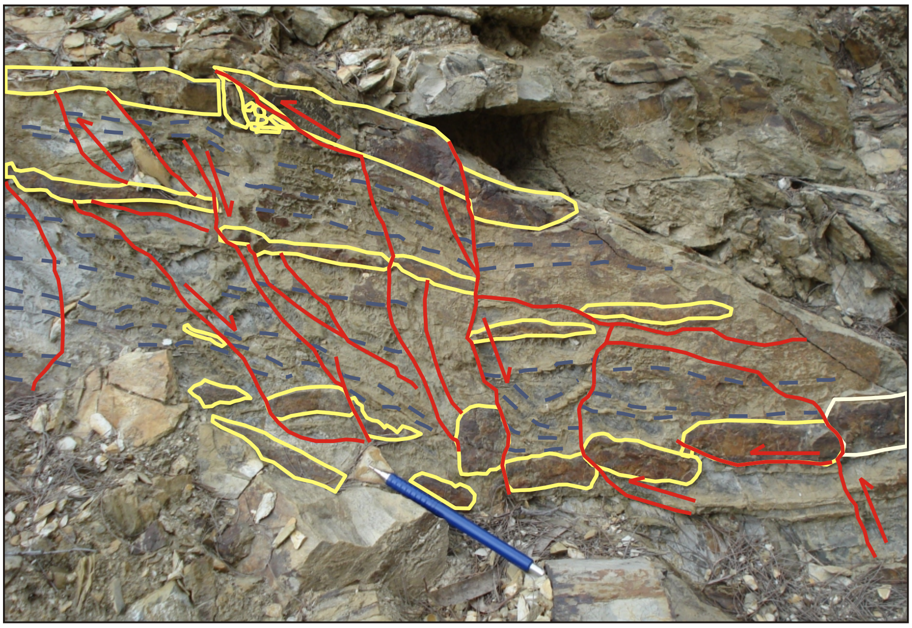

Figure 18

Photograph of outcrop in SDpq at 597 036 mE, 5 410 522 mN close to the causeway where Granite Knob Road crosses the Avenue River. The darker layers outlined in yellow are sandstone and the other layers are siltstone. Red lines are faults. The photograph hints at some of the structural complexities in the area.

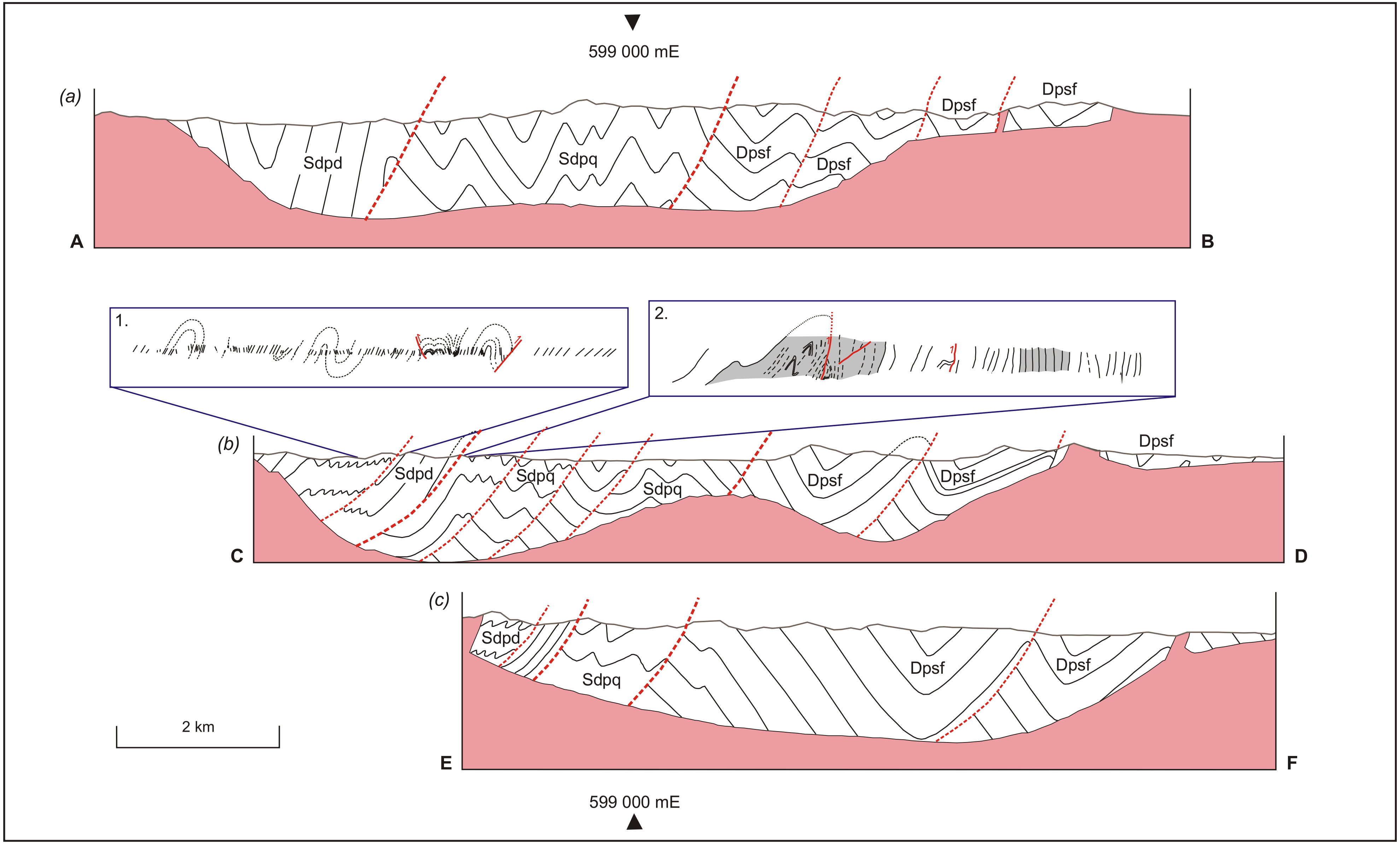

Figure 19

Structural sketch cross sections A–B, C–D and E–F. Line of sections given in Figure 1. The pink areas are granite and are based on the latest available granite model. In some cases this does not fit the surface geology and has thus been modified. The insets are details along section C–D. Length of section of inset 1 is 225 metres. Length of section of inset 2 is 130 metres. The grey areas are mudstone rich.

that these structures provide important evidence that most of the shortening in the Mathinna Supergroup occurred or was resumed after emplacement of the St Marys Porphyrite.

The Scamander Formation is terminated to the west by a thrust which juxtaposes it against SDpq (fig. 19*a*, *b* and *c*). This lithology is much richer in mudstone and is the locus of intense thrusting and folding. The SDpq is terminated to the west by another thrust which separates it from the SDpd. This contact has also been observed in creek sections in the ground to the south. There is also a striking change in minor fold styles across this structure which are illustrated in insets 1 and 2 of Figure 19*b*. These will be discussed further below.

Figures 19*a* and 19*b* suggest that there is a mismatch between the structures on either side of the Orieco Fault, particularly in the SDpq. For example, the large mappable folds that occur on the western side of the SDpq and SDpd outcrops on the north side of the fault cannot be traced into the ground to the south of the fault. Here the folds in SDpq and SDpd have much shorter wavelengths than those along strike to the north (compare fig. 19*a* and 19*b*). In addition, SDpq appears to have been the locus of more intense thrusting south of the fault. This is particularly apparent in the zone immediately to the west of the outcrop of the Scamander Formation approximately along the north–south line of Semmens Road (fig. 19*b*). One possible explanation for this apparent change in geometry is that the Orieco Fault is a more complex structure than previously thought. McClenaghan *et al.* (1992) recorded it as a strike-slip fault displacing the outcrop of Devonian granitic intrusions, but the mismatch described above suggests that it may have originated as a lateral ramp during D_1. It is interesting to note that Keele (1994) used a similar explanation to account for a fault near Mathinna some 20 km to the west of the project area. This structure has the same sinistral displacement and northeast to southwest trend as the Orieco Fault and there is also a mismatch in the geology across it. Keele (1994) traced this structure for about 50 km and recorded a possible six kilometre sinistral displacement. He suggested that it is a D_1 transfer zone that has been reactivated during later mega kinking (Goscombe *et al*., 1994). It is noteworthy that the South Esk River valley between Fingal and Avoca has the same northeast to southwest trend as the above structures, suggesting the possible existence of a basement lineament that has been reactivated during D_1 as a lateral ramp in the overlying Mathinna Supergroup. Keele (1994) also relates the Mathinna structure to various mineral deposits and concludes that it may be a mantle tapping structure. The scale and size of this is not matched by the Orieco Fault although the trend and sense of displacement are the same. More will be said about this later.

Fermor (1999) and Pohn (2000) discussed the geometry and influence of lateral ramps in the evolution of the Alberta and Appalachian fold and thrust belts respectively. Pohn (2000) suggested the following criteria for recognising their presence. Firstly, there is an abrupt change in wavelength or a termination of folds along strike and secondly there is a conspicuous change in the frequency of mapped faults or disturbed zones at the surface. As noted above, both these criteria apply to the areas either side of the Orieco Fault.

The geometry of such thrust systems also requires the existence of a frontal ramp (Pohn, 2000). This accommodates movement parallel or at a high angle to the direction of tectonic transport. It is possible that the intense east-directed thrusting that is apparent immediately east of the Scamander Formation along the north-south line of Semmens Road (fig. 19*b*) and further west is such a frontal ramp that has accommodated the relative sinistral movement of the block to the south of the fault.

D_{1A} minor structures

The geometry of D_1 minor structures is clearly controlled by lithology so for this reason the structures will be described within a lithological framework.

Scamander Formation (Dpsf)

Figure 20*a* shows a plot of S_0 for the outcrop area of the Scamander Formation west of the Scamander Tier Dyke, where lithologies are dominated by massive sandstone. The girdled distribution of points suggests that the major folds are asymmetric with an open inclined east-facing geometry. Statistically the folds have a low plunge towards 173°. Outcrop on the coastal piedmont to the east of the Scamander Tier Dyke is poor but Leaman (2008) modelled an upright F_1 synclinal structure based on the regional magnetics. Data collected from the limited outcrop to the north of this syncline suggests the presence of a number of other similar major F_1 structures trending and plunging slightly east of south (fig. 19*b*). Compared with structures to the west of the dyke the diagram suggests an upright chevron-like geometry with a low plunge towards 170° (fig. 20*b*). The differences in fold geometry suggested by these diagrams may be caused by lithological variations, with the area to the east of the Scamander Tier Dyke having more pelitic intercalations. The poor outcrop here precludes a definitive answer although such outcrop as does occur suggests that there are no major differences in the lithologies present. A further complication is that there is an order of magnitude difference in the number of S_0 data points between the two areas which may have imposed a statistical bias on the data.

Figure 21*a-f* shows photographs of representative examples from the Scamander Formation. As with the major structures, these folds are generally eastward facing and inclined, with open to tight interlimb angles, and are typical of those formed in the medium-bedded sandstones of this formation. The orientation of F_1 folds and axial planes in the Scamander Formation is shown in Figure 20*c* and 20*d*. The folds mostly plunge at a low angle to the south and the axial planes have a dominant steep dip to the west.

Outcrop-scale folds are less well developed in more thickly bedded sandstone. This is illustrated by a detailed 250 m section measured along Skyline Tier starting at 603 409 mE, 5 413 562 mN (fig. 22). Apart from two exceptions, which occur in thin-bedded sandstone with pelitic intercalations, the folds have wavelengths of tens of metres and an open to gentle style, such as the broad synclinal structure whose hinge zone is indicated in Figure 22*a*. In Figure 22*b*, S_0 shows a girdle pattern with a low plunge to the south, similar to the patterns observed for most of the outcrop area of the Scamander Formation described above (fig. 20*a*). This is in

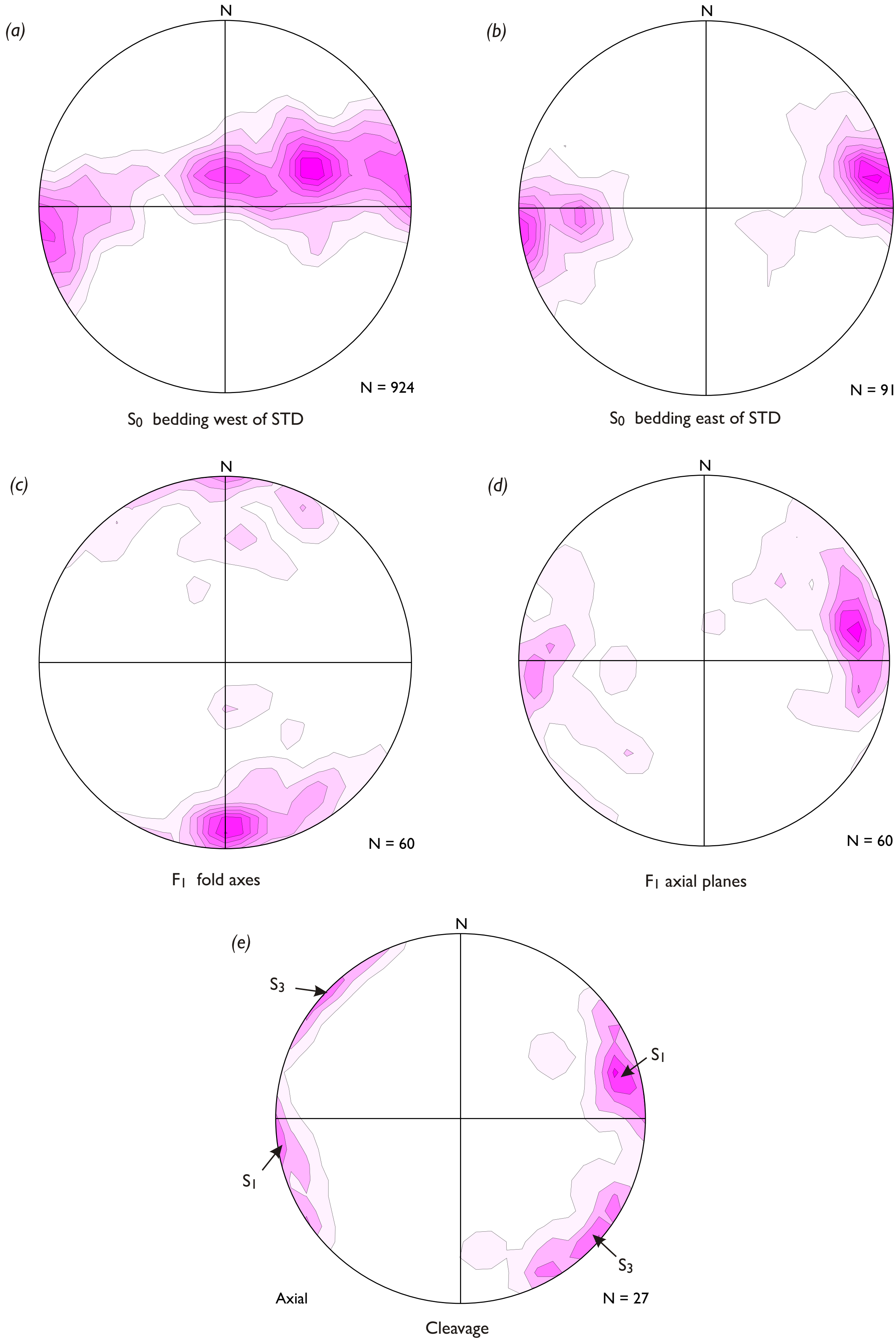

Figure 20

Structural data from the Scamander Formation (Dpsf).
(a) Poles to S_0 west of the Scamander Tier Dyke. (b) Poles to S_0 east of the Scamander Tier Dyke.
(c) F_1 fold axes all areas. (d) Poles to F_1 axial planes all areas. (e) Poles to S_1 all areas.

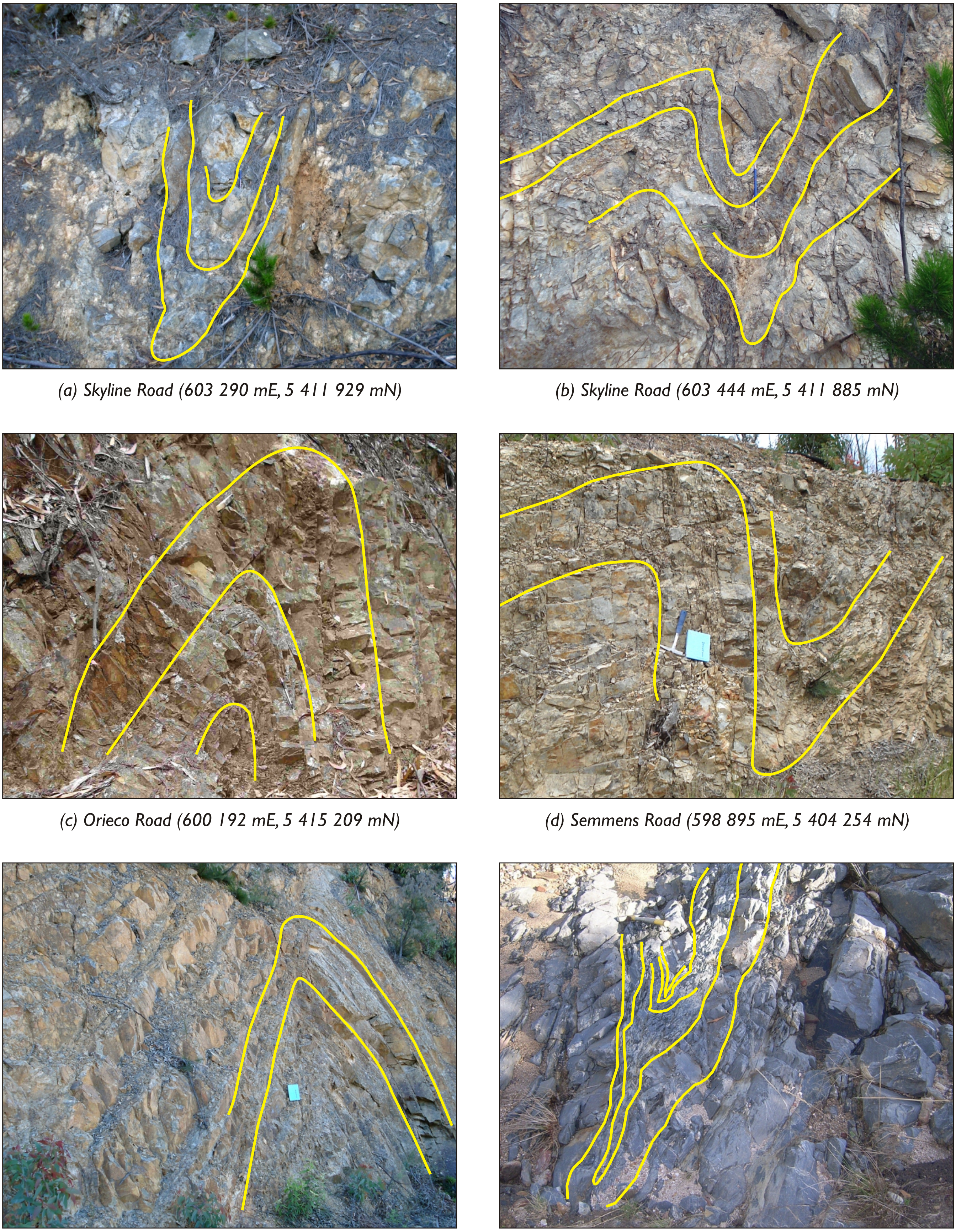

(a) Skyline Road (603 290 mE, 5 411 929 mN)

(b) Skyline Road (603 444 mE, 5 411 885 mN)

(c) Orieco Road (600 192 mE, 5 415 209 mN)

(d) Semmens Road (598 895 mE, 5 404 254 mN)

(e) Semmens Road (598 905 mE, 5 404 279 mN)

(f) Sub-vertical view of deformed isocline along East Creek Fault at 602 158 mE, 5 415 558 mN

Figure 21

F_1 folds in the Scamander Formation (Dpsf). Photographs (a) to (e) look approximately north.

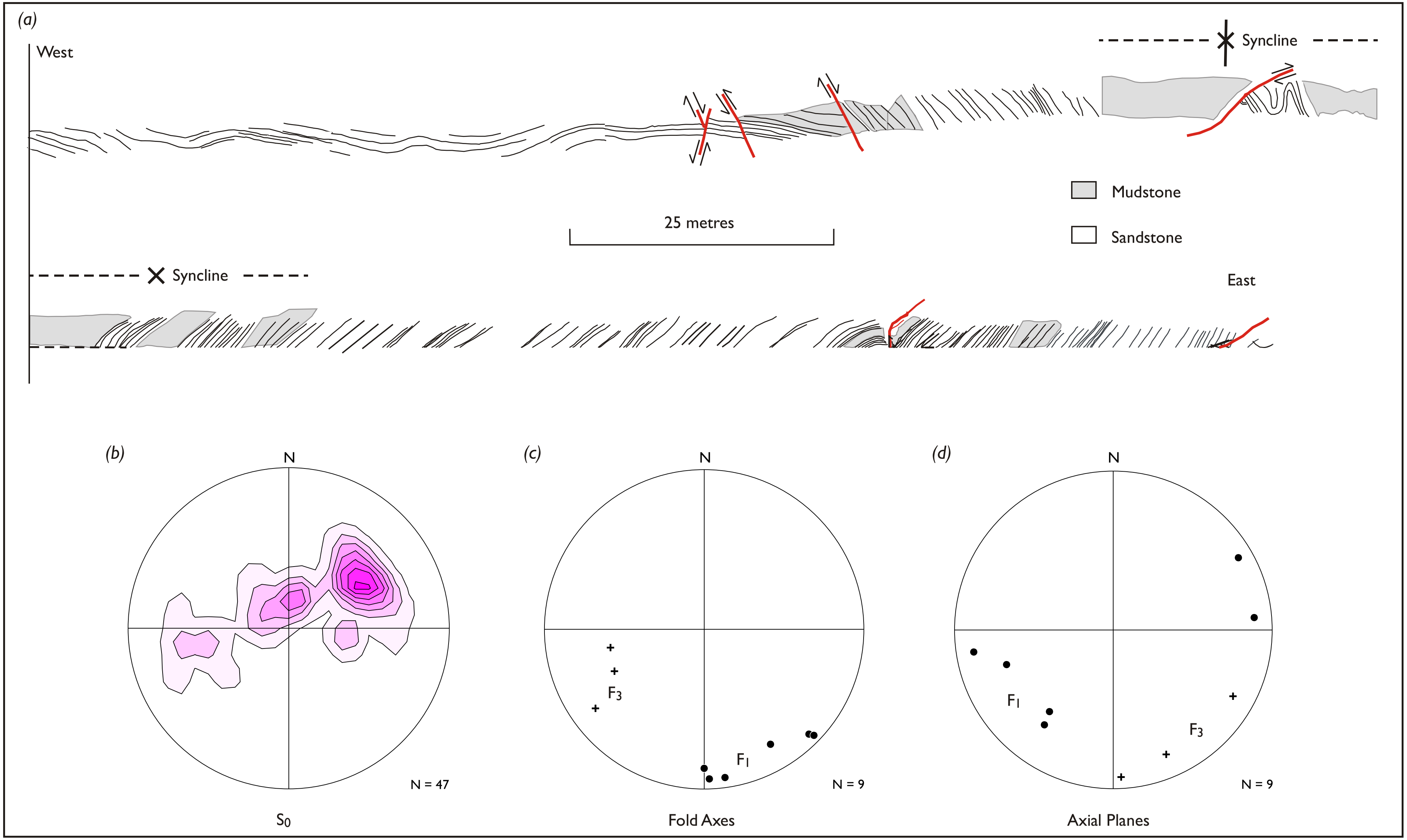

Figure 22

(a) Sketch of road section along Skyline Tier. The section has been transformed electronically such that west is on the left hand side. Western end of section is at 603 218 mE, 5 413 566 mN, eastern end at 603 409 mE, 5 413 562 mN.
(b) Plot of poles to S_0 for the section. (c) Plot of fold axes. Note the difference in orientation of F_1 and F_3.
(d) Poles to fold axial planes. See text for explanation.

marked contrast with more mudstone and siltstone-rich lithologies to the west where the folds are usually characterised by more complex geometries.

Minor fold orientations are shown in Figure 22*c* and 22*d*. The data suggest a low plunge to either north or south with sub-vertical axial planes.

Cleavage is generally not well developed in the Scamander Formation and is confined to pelitic units where it is not ubiquitous. This is consistent with the observations of Powell *et al.* (1993) and Patison *et al.* (2001). Cleavage does increase in intensity towards the west across the whole area. Figure 20e shows a plot of data for the Scamander Formation and shows a bimodal distribution. On this diagram one set has a strike west of north and is consistent with the axial plane orientation of the F_1 folds and is thus designated S_1 on the diagram. The other is labelled S_3 and will be discussed in more detail below.

SDpq and SDpd

S_0 plots of these two lithologies show that their structural geometry defines three domains between the Scamander Formation and the Catos Creek Dyke (fig. 23). Domain 1 is to the north of the Orieco Fault and includes SDpq and SDpd (fig. 23*a*). Domain 2 is to the south of the fault, west of the thrust that separates the two lithologies, and includes SDpq (fig. 23*b*). Domain 3 is to the east of this thrust and includes only SDpd (fig. 23*c*).

Figure 23*a* shows S_0 for Domain 1 and suggests a chevron geometry for the folds. To the south of the fault the picture is more complex. West of the thrust that divides the two lithologies the rocks comprising unit SDpd dip more or less homoclinally to the west (fig. 23*b*), while to the east of the dividing thrust, the SDpq plot shows an incomplete girdle (fig. 23*c*). The three domains could not be separated on plots of F_1 fold axes, F_1 axial planes and S_1 cleavage and these are shown in Figures 23*d*, 23e and 23*f* respectively.

A selection of minor folds in SDpq is shown in Figure 24*(a-f)*. These have open to tight interlimb angles and are generally eastward facing. Comparison with the F_1 structures in the Scamander Formation (fig. 21*a-f*) suggests that they are not very different, although the SDpq is distinguished by its higher pelite content. These observations can be explained by the fact that outcrop-scale folds in the Scamander Formation only form in the presence of mudstone or siltstone-rich lithologies but the large-scale structure is controlled by the abundant massive sandstone whose relative absence in SDpq means that no such control existed (see also Figure 22*a*).

To the west of the thrust that separates SDpq and SDpd the rocks dip more uniformly to the west (fig. 23*b*) and outcrop scale folds are difficult to detect in the fine-grained sandstone, siltstone and mudstone. Figure 25*a* shows a detailed section along Catos Road (at 596 728 mE, 5 408 631 mN) which shows tight easterly-verging D_1 folds with short wavelengths. Figures 25*b* and 25*c* show associated plots of S_0 and S_1 respectively.

There is clear evidence for cleavage fanning in this section. For example, the cleavage associated with the fold depicted in Figure 26*a* is refracted through layers of different competence. This clearly shows that it is contemporaneous with the folds and was not imposed by a later deformation event. There is some evidence that a minor deformation event occurred subsequently and this will be discussed below.

The above section is placed in the larger scale structural context in the insets of Figure 19*b*. Another F_1 thrust has been mapped in this domain. This crops out along Catos Road at 596 741 mE, 5 408 637 mN and appears to separate the homoclinally dipping sandstone and siltstone to the east from the folded rocks to the west (see fig. 25*a*). When this domain is traced northwards along strike across the Orieco Fault there is a mismatch in the structural styles compared with the area to the south. This mismatch and change in structural style supports the suggestion that the Orieco Fault was a transfer zone during D_1. The more intense shortening suggested by the thrusting to the south of the fault also supports the suggestion that this was part of a frontal ramp.

The orientations of F_1 fold axes in SDpq and SDpd are also similar to those in the Scamander Formation (fig. 23*d*), indicating a low plunge slightly east of south or west of north. There is however a greater spread of orientations compared with the Scamander Formation. This may be explained by the influence of a later deformation event and will be discussed below. F_1 axial planes have a similar orientation in all three sedimentary units (fig. 23e). S_1 is strongly developed in the pelite and siltstone, particularly in SDpd towards the west (fig. 23*f*), and shows a sub-vertical distribution which is broadly parallel with F_1 axial plane distributions. Some examples of cleavage in SDpq and SDpd are shown in Figure 26(*a-d*).

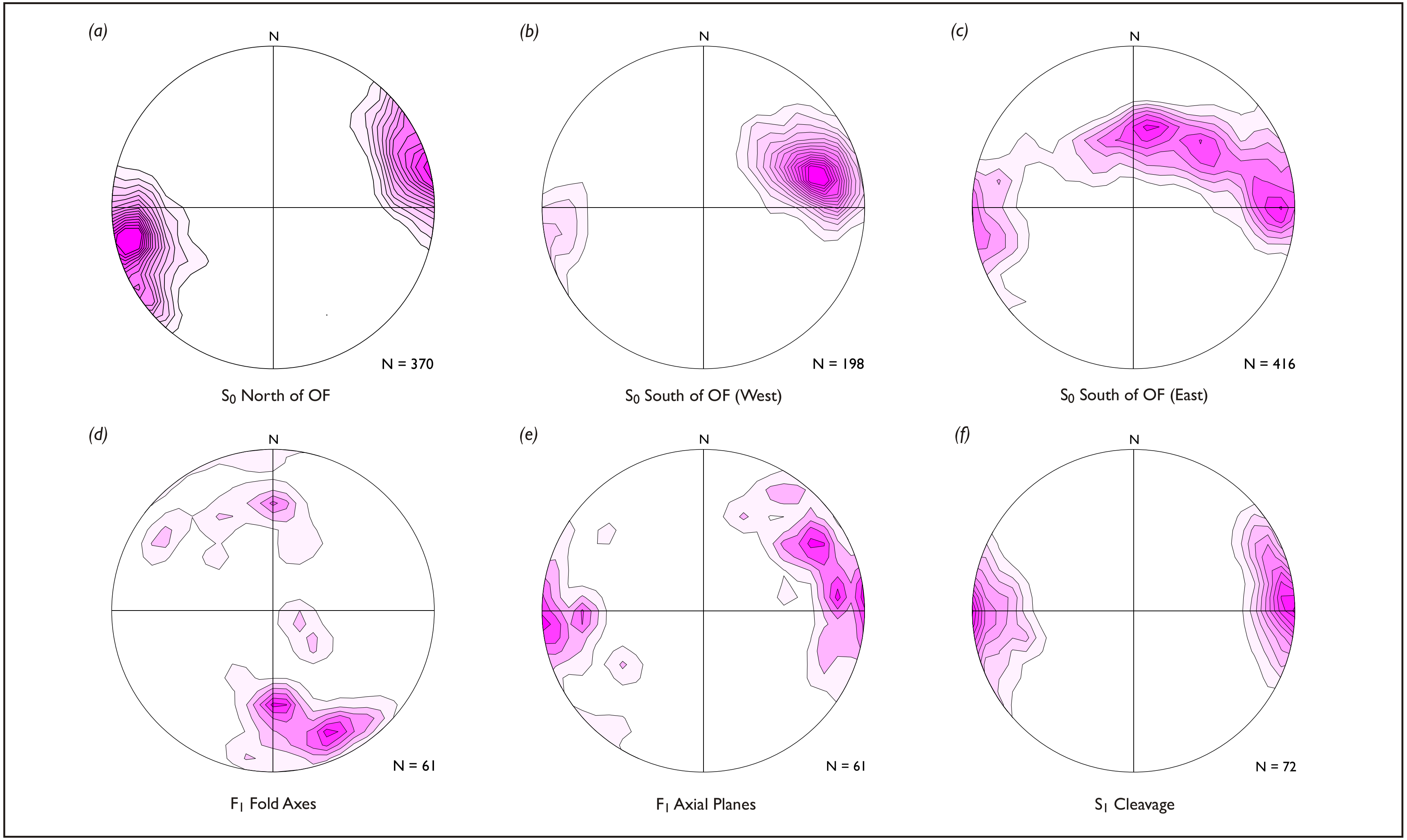

Figure 23

Structural data for SDpq and SDpd east of the Catos Creek Dyke. (a) S_0 north of the Orieco Fault. (b) S_0 south of the Orieco Fault to west. (c) S_0 south of the Orieco Fault to east. (d) F_1 fold axes all areas. (e) F_1 axial planes all areas. (f) S_1 cleavage all areas.

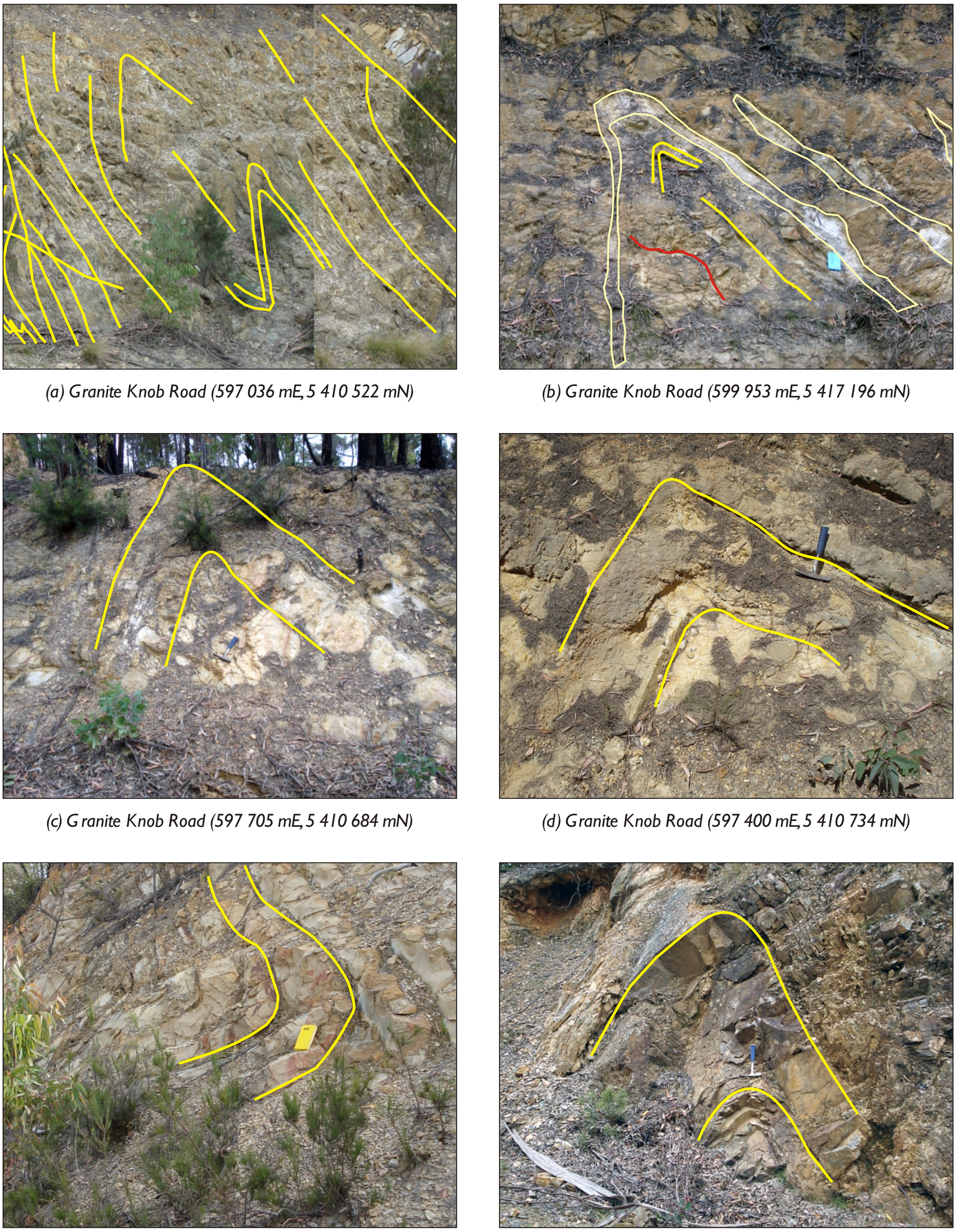

(a) Granite Knob Road (597 036 mE, 5 410 522 mN)

(b) Granite Knob Road (599 953 mE, 5 417 196 mN)

(c) Granite Knob Road (597 705 mE, 5 410 684 mN)

(d) Granite Knob Road (597 400 mE, 5 410 734 mN)

(e) Semmens Road (599 319 mE, 5 407 793 mN)

(f) West of Semmens Road (599 386 mE, 5 406 300 mN)

Figure 24

F_1 folds in SDpq. Photos (a) to (e) looking approximately south, (f) looking approximately north.

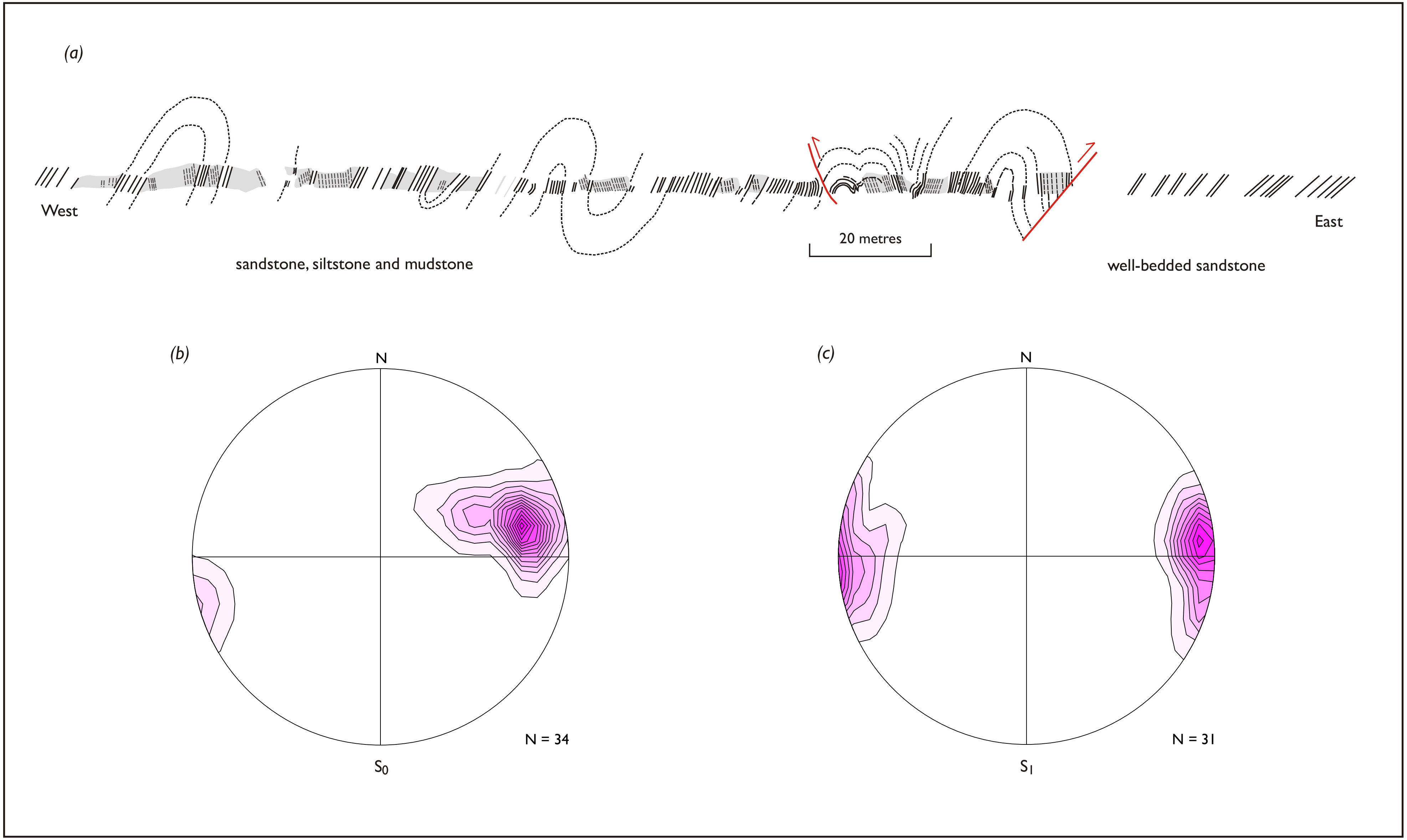

Figure 25

(a) Sketch of road section along Catos Road within SDpd. The section has been manipulated electronically such that west is on the left hand side. The western end of the section is at 596 589 mE, 5,408,605 mN, the eastern end at 596 774 mE, 5 408 652 mN . (b) Poles to S_0 for section. (c) Poles to S_1 for section. Solid lines in outcrop are bedding, broken lines are cleavage.

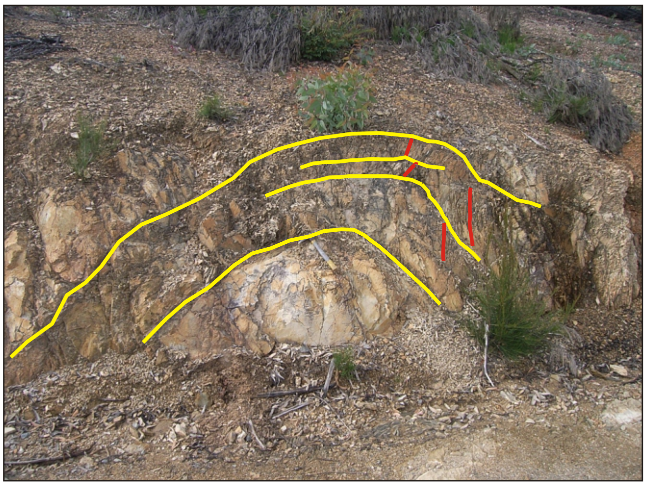

(a) Catos Road (596 710 mE, 5 408 627 mN). Note the cleavage refraction in this outcrop.

(b) Avenue River (596 033 mE, 5 410 121 mN)

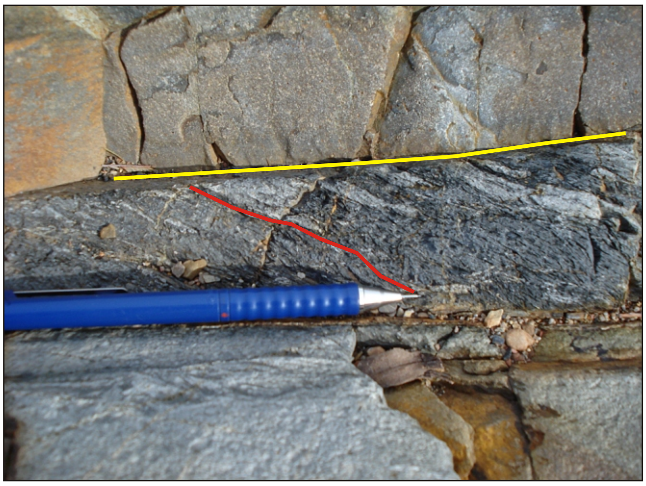

(c) Orieco Road (601 861 mE, 5 415 606 mN)

(d) Avenue River (594 858 mE, 5 409 954 mN)

Figure 26

Examples of S_1 cleavage. Yellow lines are bedding, red lines are cleavage.

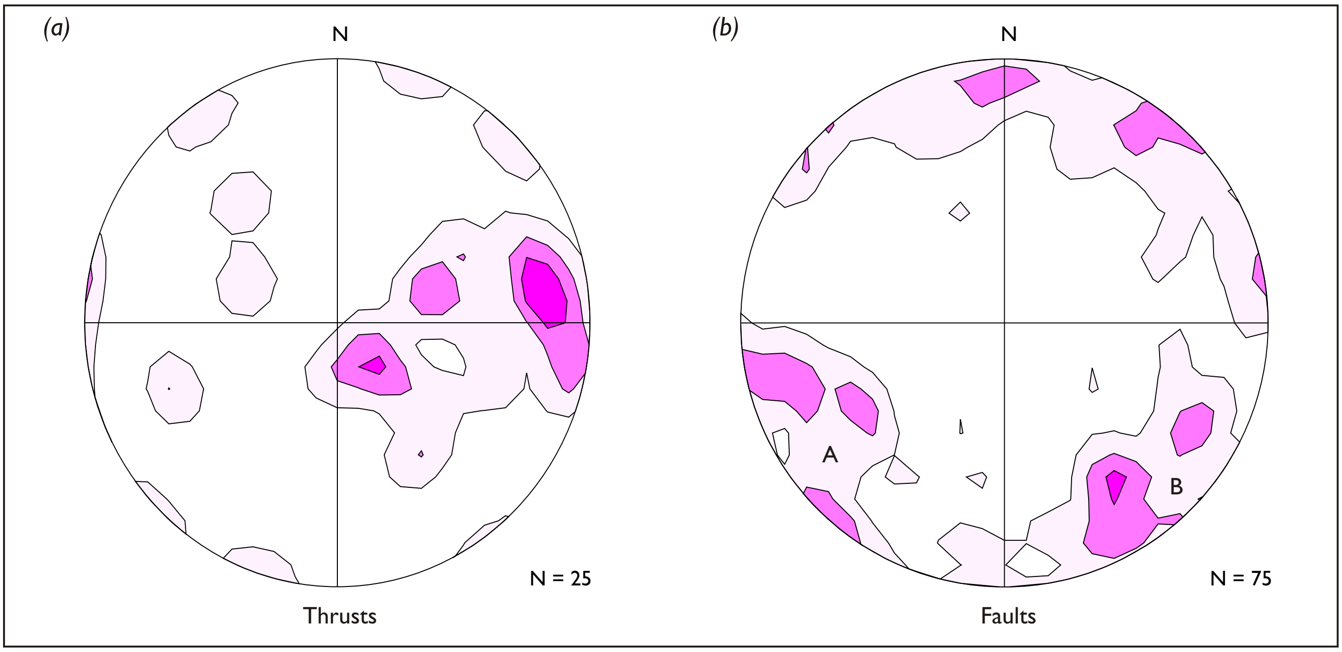

Figure 27

Structural data on faults. (a) Poles to thrust faults. (b) Poles to other faults.

D_{1A} thrusts

The distribution of thrusts in Figure 27*a* suggests a variable dip to the west, which is consistent with the information presented above. This variation may be explained by the ramping of thrusts up through the succession, with consequent dip change. The presence of recumbent folding and penetrative cleavage in the western part of the Mathinna Supergroup outcrop suggests a higher ductility implying a deeper crustal level during deformation (Powell and Baillie, 1992). In the project area D_{1A} structures show many features of a classical thrust tectonic terrain (Boyer and Elliott, 1982; Butler, 1982) (fig. 28*a*-*e*). These structures include outcrop-scale décollement surfaces with hanging wall anticlines (fig. 28*a,b*), the ramping of thrusts up through bedding giving rise to pinch-out features (fig. 28*c*-*e*) and duplexing (fig. 28*d,e*). Although these structures are relatively common on the outcrop scale, most of the major thrusts in the area were inferred from structural mapping and SpheriStat™ profiles (fig. 19*a*-*c*).

There does appear to be a significant association between thrusting and mudstone-rich lithologies in SDpq. For example, thrusts appear to be particularly well developed within lithologies cropping out immediately to the west of the Scamander Formation. Figure 29*a* (597 863 mE, 5 410 542 mN) shows a mixed sandstone-mudstone lithology with a hanging-wall anticline defined by grey mudstone. Above this fold is a mudstone horizon whose contacts are interpreted as thrusts. Intense micro-thrusting can be seen within the mudstone, with the thrusts ramping up across the bedding (fig. 29*b*). Similarly sheared bedding and disrupted fold closures were also observed in a similar lithology along Trout Road (at 602 153 mE, 5 412 430 mN) (fig. 29*c*). This zone has been interpreted as a major D_{1A} thrust zone and is also a prominent north-south trending magnetic lineament. The presence of folding within the St Marys Porphyrite (Turner and Calver, 1987) suggests that D_{1A} was a protracted event interrupted by intrusion of the porphyrite. It is probable therefore that the Scamander Tier and Catos Creek dykes were intruded along thrusts that formed early in the D_{1A} event.

D_{1B} quartz veins

Routine mapping across the whole project area revealed the presence of ubiquitous linear quartz-filled veins in sandstones. They most commonly occur as isolated veins (fig. 30*a*) but have also been observed as parallel (fig. 30) or *en echelon* arrays (fig. 30*d*). Conjugate intersecting sets (fig. 30*c*) have also been recorded and more rarely, linear types may be associated with sigmoidal veins (fig. 30*d*). The linear veins are lenticular and up to 300 mm in length and range in maximum thickness from a few millimetres up to thirty millimetres. Their thickness to length ratio ranges up to 1:30. All veins are filled with pale-coloured syntaxial quartz crystals orientated perpendicular to the walls. The quartz may also be layered with lighter and darker types juxtaposed. The veins show consistent cross-cutting relationships, indicating that they are late features, and have proved useful as time markers assisting in unravelling the structural history of the area. They are present in the massive hornfels along the Avenue River section west of the Catos Creek Dyke which is the same age as the associated St Marys Porphyrite. This would place their age as post 388 ± 1 Ma (Turner *et al.*, 1986). Statistical orientations suggest two steeply-dipping conjugate planes trending about 042° and 281° respectively (fig. 30e).

Groves (1972) described the orientation of mineralised lodes in the Scamander mineral field. According to his data these strike between 20° and 100°, broadly perpendicular to the dominant NNW–SSE regional strike, and Groves interprets them as tension fractures. The spread of his data is not inconsistent with the orientations presented above but the occasional examples of layered quartz in the veins described above are the only hint that some are mineralised. Keele (1994), working further to the west in the Mathinna area, described a complex array of veins, none of which can be correlated with the examples described above. This is not surprising as Keele's area is part of the Mathinna–Alberton gold lineament, a zone which has undergone complex deformation and mineralisation.

The literature on veins suggests that there is little agreement on their mode of formation (e.g. Beach, 1975; Rickard and Rixon, 1983; Hancock, 1985; Ramsay and Huber, 1987; Rothery, 1988; Smith, 1996; Fischer *et al.*, 2009). Most of these papers refer to the work of Beach (1975) who proposed a geometric scheme for classifying *en echelon* vein arrays. In his Type 1, the vein fractures form after the development of a shear zone and the veins of one array are parallel to the boundary of the complementary conjugate array. In Type 2 the shear zone develops after fracture formation and the veins are parallel to a bisector of the conjugate array. Smith (1996) argued that these two types are only specific cases within a geometric continuum in which the vein arrays can be classified according to whether they are convergent or divergent relative to the principal bisector. Study of published data led him to conclude that convergent arrays are the most common. Smith (1996) documented six vein arrays in turbidites from New South Wales and found that poles to veins were close to the poles of the complementary conjugate arrays. He also found that the trend of the principal shortening direction (ε_1) is approximately perpendicular to the axial surfaces of the dominant folds, suggesting that the veins and folds are linked by a common stress field. In this context, Fischer *et al.* (2009) also recorded a close association between different vein types and evolving flexural slip folding at Monterrey, Mexico. It is interesting to note that the conjugate arrays that most closely resemble those described here form in the most competent units and the principal compressive stress responsible for the folding bisects the angle between the conjugate arrays.

Smith (1996) also argued that Beach's (1975) geometric classification had influenced interpretations of fracture mechanisms, leading to the conclusion that Type 1 veins are shear fractures and Type 2 are extension fractures. He argued that a new model is required to explain how extension fractures can form in convergent conjugate arrays as the principal strain axes cannot be parallel in such arrays. He proposed a model involving conjugate faults which, when modified by local variations in competence, break down into *en echelon* fracture arrays with convergent conjugate geometry. Sigmoidal veins develop by rotation of the overlap

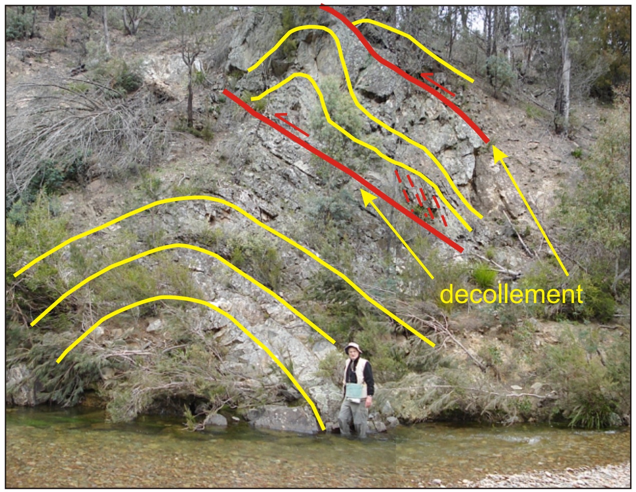

(a) Avenue River (591 186 mE, 5 408 840 mN)

(b) Scamander Tier (603 335 mE, 5 413 534 mN)

(c) Trout Road (601 974 mE, 5 412 974 mN)

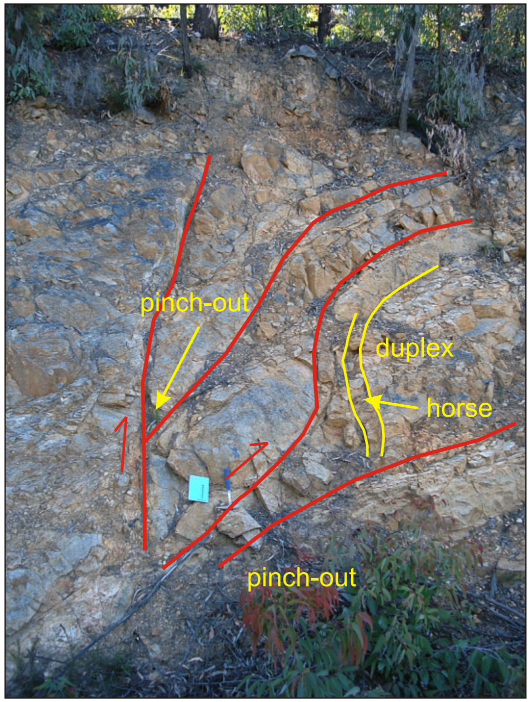

(d) Semmens Road (598 908 mE, 5 404 302 mN)

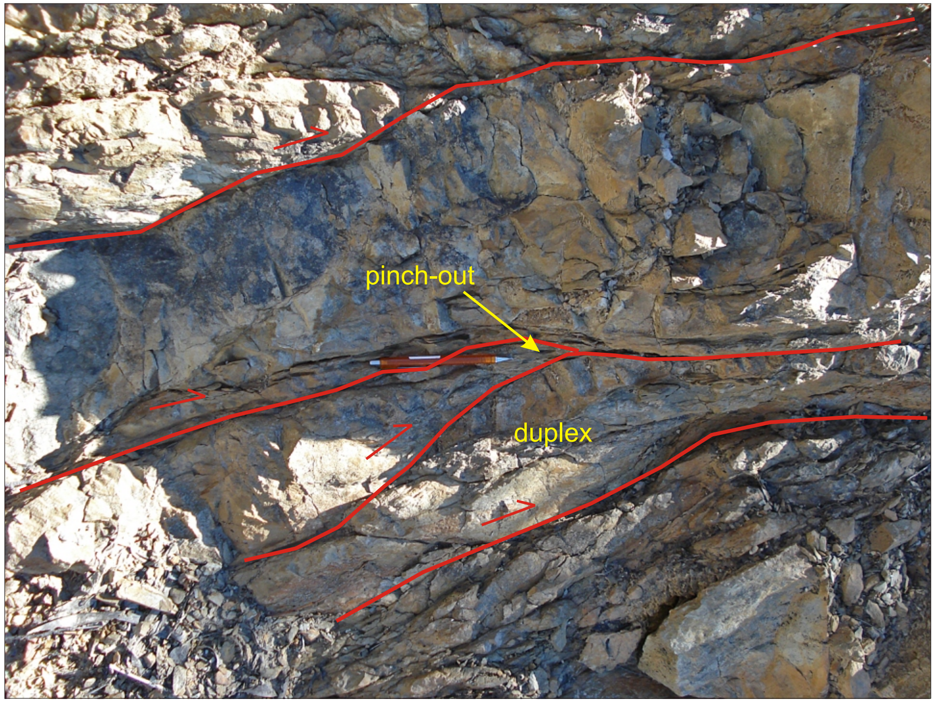

(e) Semmens Road (598 939 mE, 5 404 392 mN)

Figure 28

Outcrop scale F_1 thrusts. Thrusts are solid red lines, bedding is yellow. In (a) cleavage is broken red lines.

(a) Sdpq along Granite Knob Road (597 868 mE, 5 410 528 mN).

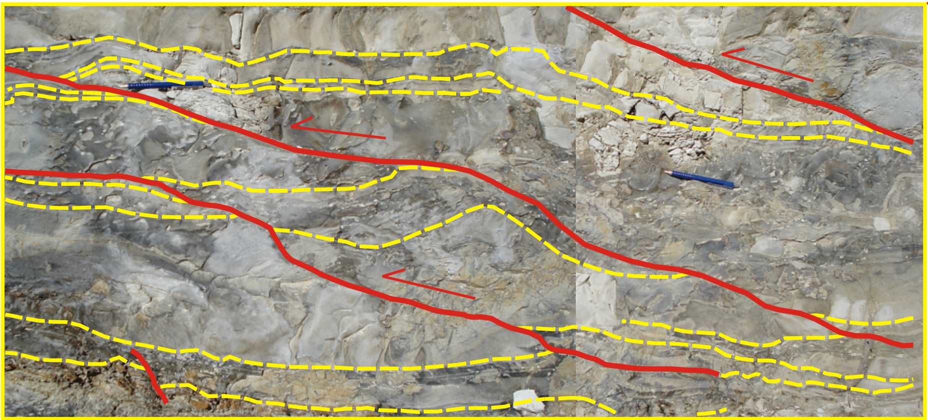

(b) Inset from (a). Scale is given by pen.

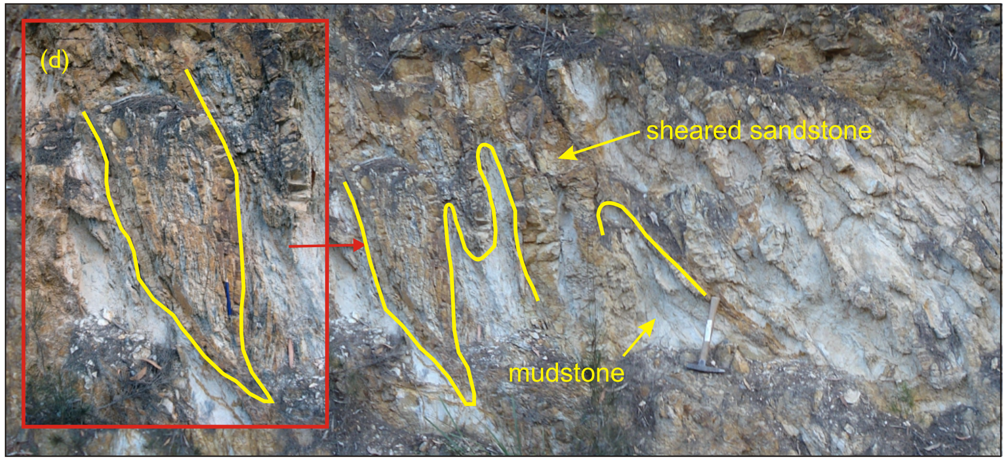

(c) Dpsf along Trout Road at 602 106 mE, 5 412 587 mN showing tight F_1 folds in thrust zone.
(d) Inset showing detail from (c).

Figure 29

F_1 thrusting in mixed sandstone-mudstone lithologies. (a), (b) and (c) looking approximately south. See text for explanation.

(a) Dpsf along Loila Tier Road at 599 953 mE, 5 417 196 mN.

(b) SDpq along Bolpeys Creek at 598 485 mE, 5 406 517 mN.

(c) Dpsf along Cramps Road at 602 304 mE, 5 415 856 mN.

(d) SDpd in Avenue River at 595 166 mE, 5 409 916 mN.

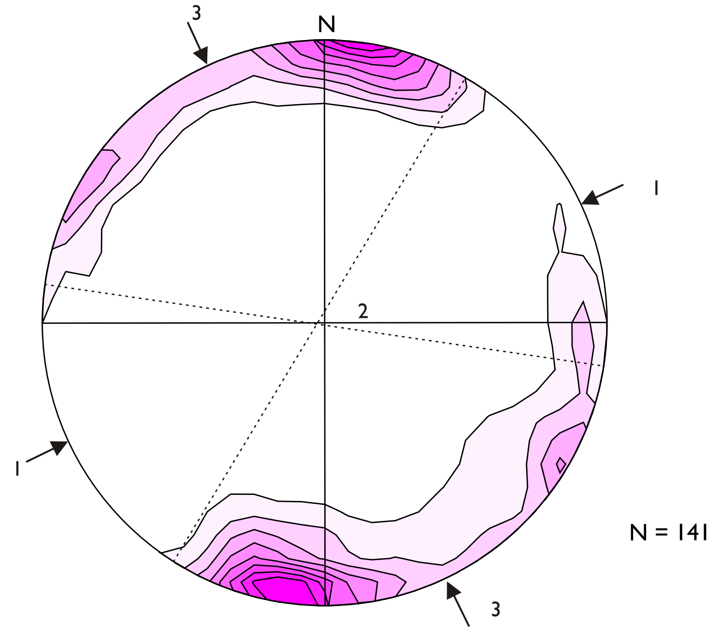

(e) Plot of poles to quartz-filled gashes with constructed $_1$, $_2$, $_3$ stress directions.

Figure 30

Structural data on quartz-filled gashes.

zones or bridges between adjacent *en echelon* veins. Serial sections through vein arrays suggested that linear veins may pass laterally into sigmoidal types.

Smith's (1996) conclusion that the most common natural conjugate vein arrays are convergent suggests that it is likely that the array described in this section is also convergent, although this would require further detailed work to determine conclusively. Smith (1996) also found that poles to one set of veins were close to poles of the bounding surface of the complementary conjugate array. The three principal strain axes ($\varepsilon 1$, $\varepsilon 2$, $\varepsilon 3$) were derived from the bisectors to these arrays. If this is applied to Figure 30*e* (using the principal stress axes $\sigma 1$, $\sigma 2$, $\sigma 3$) a steeply dipping $\sigma 3$ and sub-horizontal $\sigma 1$ orientated to 068° are obtained. The principal compressive stress direction ($\sigma 1$) is approximately the same as that responsible for the earliest deformation structures (D_1) which has imposed the dominant NNE regional structural grain (compare Figures 30*c* and 30*e*). This relationship is similar to that observed by Smith (1996) and Fischer *et al.* (2009). It was noted above that there was evidence of post-extrusion folding of the St Marys Porphyrite and the presence of mylonitic shears in that body. Turner and Calver (1987) suggested that this provides important evidence that the stress field responsible for the D_1 deformation continued or was resumed into the period post-dating emplacement of the porphyrite. The similarity of the maximum compressive stress derived from the veins and that responsible for D_1 suggests that the veins may have been produced during such an extended or resumed phase of deformation. More will be said later about the relationship of these vein arrays to other deformation structures.

D_3 faults and folds

A complex picture has emerged from study of the faults in the area. Faults and other brittle structures were commonly observed at outcrop scale but the rarity of kinematic indicators, such as slickensides, and the often confusing nature of displaced lithological markers made it difficult to assess true displacement vectors. Where possible this distinction has been made and Figure 27*b* is based on these inferences.

D_3 faults

The bimodal distribution of faults on Figure 27*b* is difficult to interpret. McClenaghan *et al.* (1992) considered that the contact of Dbgsp, which is intruded by the Scamander Tier Dyke on the northern part of the St Helens map sheet, is locally faulted with downthrow to the west. Similarly, the eastern contact of the Catos Creek Dyke is mapped as a fault because there is virtually no metamorphic aureole here compared with a thick aureole on the western side. McClenaghan *et al.* (1992) considered that this fault downthrows to the east and has faulted out the aureole. They concluded that the Mathinna sediments were dropped down between these two bounding faults in response to cauldron subsidence caused by magma withdrawal related to extrusion of the St Marys Porphyrite. The trend of the faults approximates to concentration A on Figure 27*b* and was probably determined by D_{1A} thrusts. Groves (1972) also noted the presence of faults with this trend north of the Scamander River. Although inconsistent slickenside orientations made movement directions difficult to interpret, Groves noted that they were parallel to the mean regional axial surface trend.

The trend of concentration B (fig. 27*b*) is parallel to the Orieco Fault and may be related to strike-slip movements associated with that structure or to D_1 movements related to lateral ramping, or both. A fault which approximates to this trend is mapped as displacing the outcrop of the Scamander Tier Dyke at 603 450 mE, 5 413 415 mN and is clearly a late structure (McClenaghan *et al.*, 1992). In addition, Taylor (1992) and Keele (1994) described NNW trending sinistral strike-slip faulting on the outcrop scale. Taylor (1992) stated that these structures post-date the intrusion of the Catos Creek Dyke. Notwithstanding the clear sinistral displacement of the two major dykes, the present author has not observed clear evidence for such wrench movements along the minor faults represented in Figure 27*b*.

D_3 — the Orieco Fault

Evidence has emerged that the Orieco Fault may have a longer and more complex history than suggested by the obvious strike-slip displacement. It was noted above that differences in the structure across the fault suggested that it may have acted as a lateral ramp during D_1.

The Orieco Fault is a sinistral strike-slip fault that trends northeast to southwest across the northern part of the area east of the Catos Creek Dyke. Movements along it have added considerably to the structural complexity of the enclosing Mathinna sediments. The fault is the best documented of a series of parallel sinistral strike-slip structures that displace other magnetic lineaments (Worthing, 2010 *a, b*; Worthing and Woolward, 2010*a*). The sinistral displacement has been demonstrated by previous authors in relation to the Scamander Tier and Catos Creek dykes (McClenaghan *et al.*, 1992). Similarly, displacement of the Mount Pearson granite contact at 595 500 mE, 5 417 600 mN provides further outcrop evidence, although the dip of the intrusive contact is not clearly known here. McClenaghan *et al.* (1992) represented the fault as two separate segments on their map. Recent geophysical work has shown that the structure is also defined by a strong magnetic lineament (Leaman, 2008) (fig. 12) which, together with other geophysical evidence, provides further proof of its lateral continuity. Other offset features along the strike of the lineament supporting such continuity include displacement of a major NNW–SSE trending magnetic lineament along the line of Trout Road (fig. 12). Similarly, there is an apparent displacement of the radiometric signal in the Mathinna sediments close to the outcrop of the Catos Creek Dyke (fig. 16). In addition, structures have been observed that confirm the presence of the fault, and it has thus been possible to define the trace of the fault across much of the area.

Leaman (2008) suggested that the magnetic lineament is related to dyke intrusion along the fault. These dykes have been dated by the Ar-Ar method at about 330 Ma (mid-Carboniferous) (McClenaghan and Everard, in prep.), although there is some suspicion that Ar-loss may have reset the dates by up to 10 Ma.

Dyke intrusion along the fault is supported by the outcrop of dolerite along the line of the lineament at 601 181 mE, 5 416 629 mN. Leaman's (2008) modelling of this dyke suggests that it is vertical, implying a similar orientation for the fault. However some swings in the outcrop pattern of the fault with topography suggest a variable but steep dip to the southeast. The sinistral movements are clearly late as they post-date intrusion of the Scamander Tier and Catos Creek dykes which have been dated at 388 ± 1 Ma (Turner *et al.*, 1986). Other northeast to southwest-trending parallel magnetic lineaments are also present in the area (Worthing, 2010*a,b*; Worthing and Woolward, 2010*a*). These are also probably related to dyke intrusion along sub-vertical faults; for example, Groves (1972) recorded a dolerite dyke at 599 575 mE, 5 413 190 mN along a magnetic linear. However strike-slip offsets along this and other similar lineaments are not clear from the tilt angle derivative map (fig. 12).

D_3 — the East Creek Fault

Another major fault has been mapped along Eastern Creek Road and is here referred to as the East Creek Fault. This fault occupies a valley between 601 000 mE, 5 413 800 mN and 602 000 mE, 5 415 400 mN and a narrow band of mudstone with sub-vertical dips crops out along it. Evidence for movement is provided by a strong discordance in the orientation of S_0 in the sandstone on either side of the valley and one occurrence of a steeply-plunging periclinal fold. In addition, there is abundant quartz veining and a deformed F_1 isocline along the trace of the fault at 602 174 mE, 5 415 508 mN. The dip on the fault is difficult to ascertain but it appears to be steep. Mudstone outcrops at 601 000 mE, 5 413 800 mN suggest that the strike of the fault changes here to east–west. Further westwards, in forest creek outcrops at 599 392 mE, 5 414 065 mN, there is also a distinctive change in strike of the sediments from the normal NNW to SSE trend to east–west.

D_3 — minor folds and thrusts

A small number of folds were recorded in the Scamander Formation which have anomalous orientations relative to F_1 folds. These crop out along Skyline Tier and Orieco Road (fig. 1) particularly close to the trace of the Orieco Fault. Examples are shown in Figure 31*a–c*. These folds have open upright styles with variable plunges towards 240° and steeply dipping axial planes (fig. 31*d,e*). Where three-dimensional outcrop is available they may have a periclinal geometry. The variable axial plunges shown by these structures may be due to the deformation being imposed on bedding, with variable dips related to the earlier F_1 folding. It was noted above that cleavage in the Scamander Formation shows a bimodal distribution which is quite atypical of the area as a whole. One of these directions fits the normal S_1 trend (see fig. 20e), but the other direction, which strikes approximately 225°, is consistent with it being an S_3 axial plane cleavage to the F_3 folds described above.

McClenaghan *et al.* (1992) also noted the presence of 'gentle cross folding' associated with a rotation of the strike to the northeast along the Upper Scamander Road. They quote the orientation of these folds as 38° towards 222° which is consistent with the folds described in Figure 31. They also stated that the timing of these structures is unclear but suggested that they may be related to a roughly north to south compressional stress associated with the late sinistral movements along the Orieco Fault. This implies a post-Scamander Tier and Catos Creek dyke age for these movements. In this context it is significant that six of the above folds are close to the magnetic lineament that defines the Orieco Fault for most of its length. As noted above these folds have a variable plunge towards 240° with steeply dipping axial planes (fig. 31*d,c*).

A number of small thrust splays crop out on a bedding plane of massive sandstone close to the outcrop of the fault at 600 196 mE, 5 415 141 mN (fig. 31*f*). This bedding plane strikes 322° and has a sub-vertical dip and the orientation of the thrust splays suggests a transport direction towards 132°. In the footwall of these structures are a number of periclinal folds that are part of the suite of F_3 folds noted above. These are shown as black crosses on Figure 31*d* and an example is illustrated in Figure 31*a*. The sterogram shows that these folds trend towards 240° with variable plunges, which is approximately normal to the observed transport direction on the thrusts. This is also the trend expected from folds related to the movement along such an imbricate thrust system. It is therefore concluded here that the F_3 folds in the Scamander Formation are related to a late thrusting event associated with movements along the Orieco Fault, a conclusion supported by McClenaghan *et al.* (1992). The geometry of the structures suggests transport towards 132°. With respect to the timing of this event, Figure 31*g* shows an outcrop close to the above thrusts. Here D_{1B} quartz veins are cut by flat-lying shears which are probably related to the thrusting. This implies that the thrust movements are post the quartz veins and thus relatively late in the structural chronology.

A possible alternative interpretation for the above observations is that the F_2 folds may have developed during localised compression in a restraining bend during strike-slip movements along the Orieco Fault. However the widespread occurrence of the D_2 folds indicates that deformation was not restricted to domains adjacent to the fault.

During mapping along Semmens Road a regular juxtaposition of east–west striking domains and more normal NNW–SSE domains was observed. A similar juxtaposition also occurs in creek outcrops around 599 529 mE, 5 414 134 mN, just south of the Orieco Fault and along strike from the Semmens Road structures. The explanation for these observations was found in well-exposed sections along Semmens Road (fig. 32*a*), where a north–south striking fault separates two domains, a NNW–SSE striking domain to the west and an east–west striking domain to the east.

Figure 32*b* is a sterogram of all the east–west striking domains along Semmens Road. Figure 32*c* shows a section in the NNW–SSE striking domain at 599 126 mE, 5 409 334 mN looking approximately towards 353°. Here there are well-exposed asymmetric easterly-verging F_1 folds which conform to the general F_1 trend. These folds have been truncated by a later flat-lying thrust that has displaced the hanging wall to the south.

(a) Dpsf along Orieco Road at 600 224 mE, 5 415 124 mN showing F_3 fold.

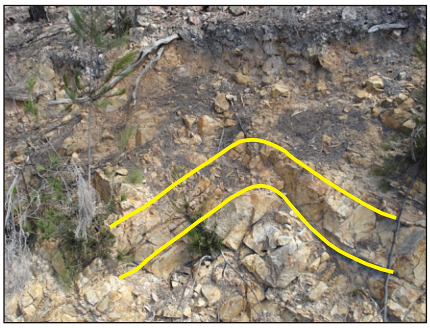

(b) Dpsf along Skyline Road showing F_3 folds (603 691 mE, 5 411 072 mN).

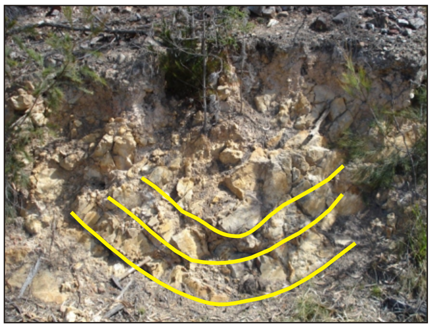

(c) Dpsf along Skyline Road showing F_3 folds (603 686 mE, 5 411 081 mN).

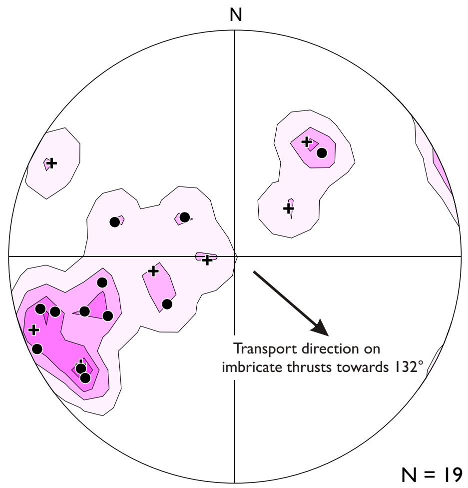

(d) F_3 fold axes

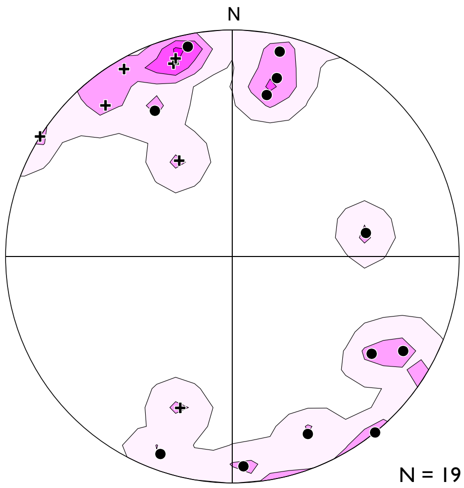

(e) poles to F_3 axial planes

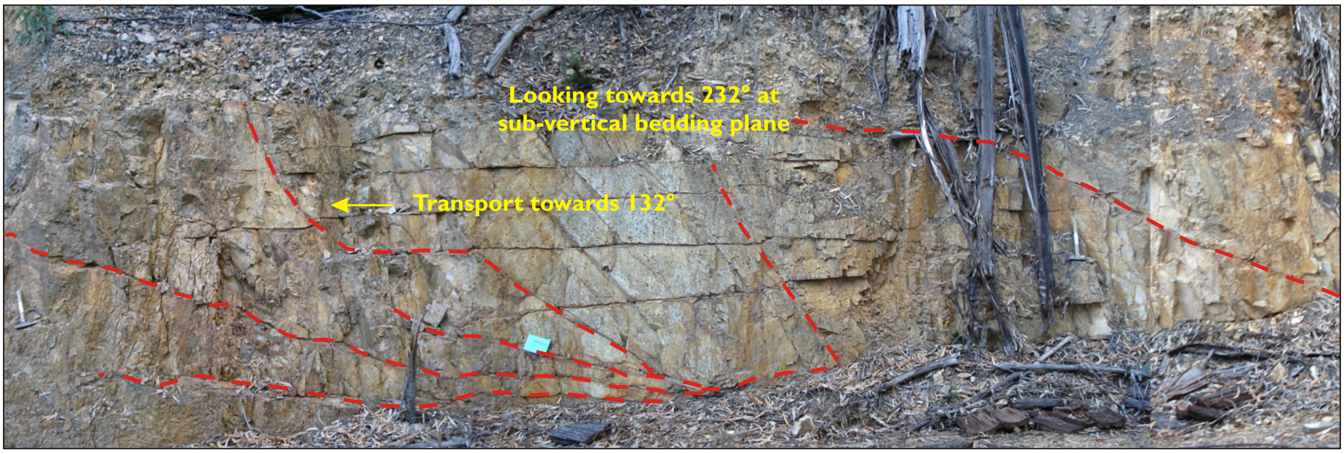

(f) Dpsf along Orieco Road at 600 193 mE, 5 415 155 mN showing F_3 imbricate thrust stack.

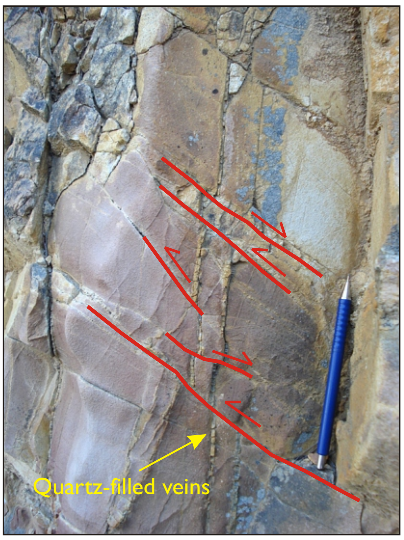

(g) Dpsf along Orieco Road at 600 194 mE, 5 415 312 mN showing sheared quartz-filled gashes close to imbricate stack.

Figure 31

Structures associated with D_3 faulting. (a)–(c) looking approximately towards 240°.

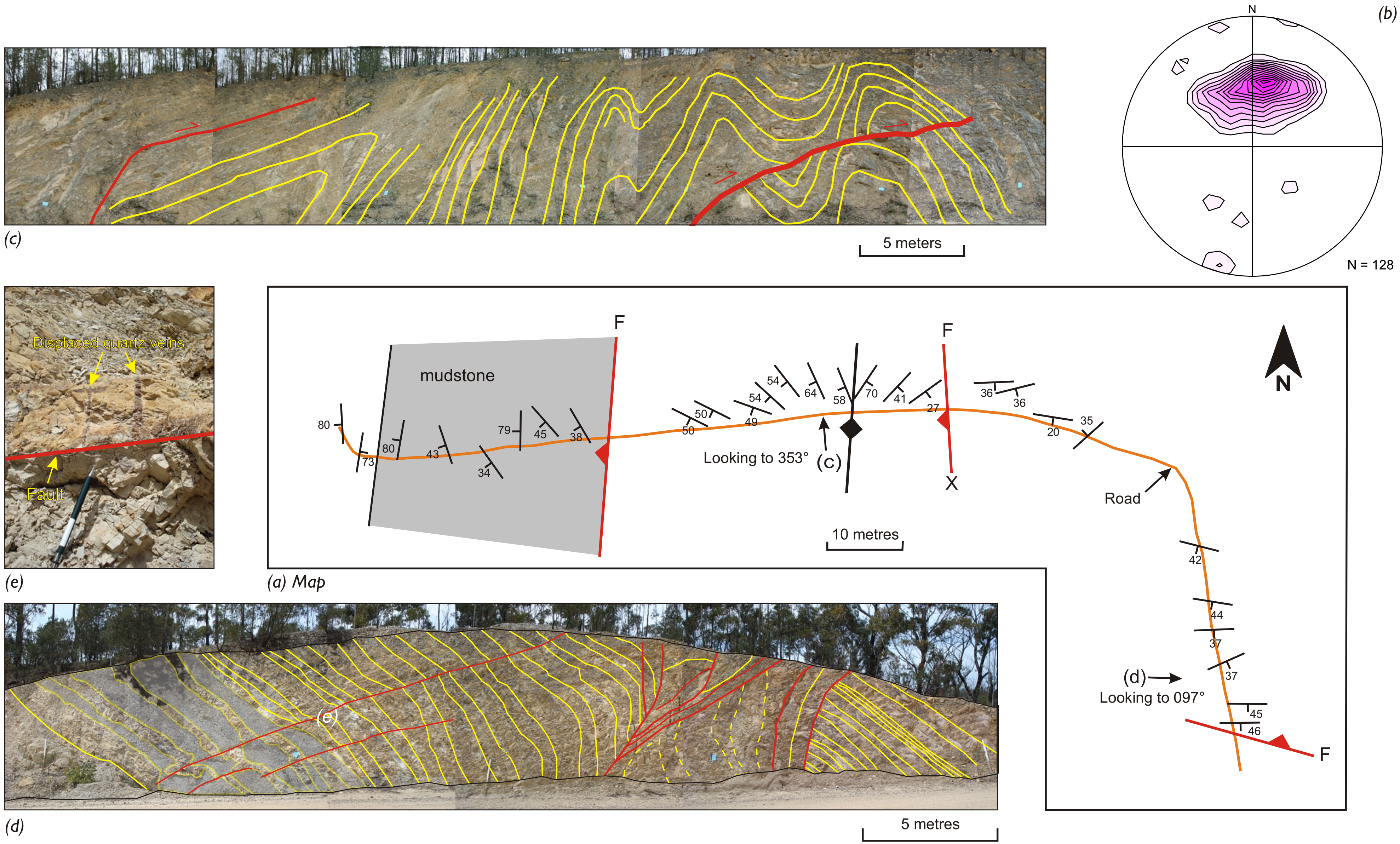

Figure 32

Structures in Dpsf associated with D_3 thrusting along Semmens Road. (a) Map of area. Points (c) and (d) are the locations of Figures (c) and (d) respectively. The hinge of the F_1 fold (point c) is at 599 128 mE, 5 40933 mN and point (d) is at 599 246 mE, 5 409 235 mN. The grey area is a mudstone-rich unit. (b) Plot poles to S_0 of east–west striking rocks along length of Semmens Road. (c) Annotated photograph of outcrop (c). (d) Annotated photograph of outcrop (d). (e) Displaced quartz-filled gash at (e) on Figure (d). Faults are red and bedding is yellow. See text for explanation.

Figure 32*d* shows the road section approximately at right angles and looking towards 097° at 599 246 mE, 5 409 239 mN. The thrusts in this section strike between 90° and 100° and provide clear evidence of a later phase of thrusting with a transport direction approximately to the south. In this section steep northward-dipping thrusts are observed with an associated hanging-wall anticline. The bedding in this domain has been rotated such that it generally strikes eastward and dips to the south. This accounts for the regular swings in strike along Semmens Road and in the forest outcrops referred to above. An explanation for this structural geometry is that D_1 thrusts with an approximately north to south strike have acted as transfer zones, allowing the later southward-directed thrusting to occur between them. The north–south trending fault X in Figure 32*a* is probably such a structure.

In the hanging wall of the D_2 thrusts described above are two flat-lying faults which were probably associated with thrust movements along the steeply-dipping structures. The orientation of these structures appears to be similar to the flat-lying structures in Figure 32*c*. More will be said about these in a later section.

Discussion

The origin of the East Creek Fault, its movement vector and its relationship to the Orieco Fault is unclear. There are two possibilities. Firstly, it may be another strike-slip fault sub-parallel to the Orieco Fault and terminating along Eastern Creek Road. This is how it is represented on the map (Worthing, 2010*a*). However the movement is shown as dextral to accommodate the apparent displacement of the major thrust along Trout Road. A thrust component also cannot be discounted. Secondly it could be a splay off the Orieco Fault. This is suggested by the swing in strike at its western termination plus the occurrence of a zone of anomalous east–west strikes between its extension and the Orieco Fault.

If the latter interpretation is correct, the occurrence of a transpressive duplex or positive flower structure between the two faults is suggested (Sylvester, 1988). The orientation of such a splay is not consistent with the fault being a Riedel shear related to sinistral movements along the Orieco Fault (Naylor *et al.*, 1986). Woodcock and Rickards (2003) described a transpressive duplex between two north–south trending sub-parallel faults in the UK Lake District. As with the East Creek Fault the orientation of the oblique splay faults does not fit the Riedel shear model but Woodcock and Rickards (2003) suggested that many structures in transpression zones are more influenced by boundary conditions than by regional stress configurations.

The D_3 folds and thrusts within the Scamander Formation adjacent to the Orieco Fault and the anomalous east–west strike changes in SDpq further south appear to be linked in a common structural nexus involving south-directed thrusting associated with the fault. However there are problems in making such a link. For example, the transport direction derived from the D_3 folds and thrusts adjacent to the Orieco Fault suggest movement towards 132° whereas the movement direction at Semmens Road appears to be more directly south or even west of south. There are no clear field data to suggest that these two sets of structures are not contemporaneous and the most simple interpretation is that they formed in response to the same stress field. It is tentatively concluded here that southward-directed thrusting associated with the Orieco Fault was responsible for the D_3 folds and thrusts and the anomalous strike changes adjacent to the faults and along Semmens Road. The East Creek Fault is interpreted as a strike-slip fault which may also have had a component of reverse dip-slip movement. The exact chronology of strike-slip movement along these faults and the D_3 folds and thrusts described above is also unclear but the most simple explanation is that they are part of the same yet possibly evolving structural event. The occurrence of a transpressional duplex or positive flower structure between the two faults is a more problematic interpretation as the east–west strike changes referred to above are not confined to the zone between the two faults.

D_5 late extensional faulting

In the section above evidence was presented linking the structural evolution of the Orieco Fault and the strike changes along Semmens Road. An interesting feature of the Semmens Road outcrops concerns the flat-lying faults in Figure 32*c* and the northern (left) side of Figure 31*d*. Although these structures were probably thrust faults associated with south-directed thrusting during D_2 they now show evidence of extensional movement. This is clear from the displacement of mudstone bands in the outcrop (fig. 32*d*). The chronology of these extensional movements is further revealed by the fact that they truncate the D_{1B} quartz-filled veins (fig. 32e) and they clearly represent a very late phase of extensional movement in the structural history of the area. Keele (1994) recorded a phase of extension along pre-existing NNW-trending wrench faults (his D_3) but the normal fault in Figure 32*d* trends 324° and dips 54°NE. The timing of this event is unclear but based on the chronology of the kink bands discussed below it is probable that it pre-dated them.

D_6 kink bands

A small number of kink bands (17) were recorded across the project area. Most of these (8) were found in the Avenue River west of the Catos Creek Dyke where outcrop of the thinly laminated lithologies necessary for kink band formation are well exposed. Their relative abundance here may also be due to the presence of a well-developed S_1 cleavage which facilitated the necessary flexural slip. Kink bands also occur in the aureole adjacent to the Catos Creek Dyke and there are examples here in which they appear to deform quartz veins, suggesting that they are post-D_{1B}. Both symmetric (fig. 33*a*) and conjugate (fig. 33*b*) examples were recorded. Figure 33*c* suggests a spread of axial trends which is probably a consequence of the kink bands deforming laminae with different orientations. Axial surfaces have a more consistent orientation (fig. 33*d*) with one major set striking northeast to southwest and a minor set approximately at right angles.

Goscombe *et al.* (1994) documented regional small-scale and mega-scale kink bands in the Mathinna Supergroup. The megakink bands have an axial spacing of up to nine kilometres

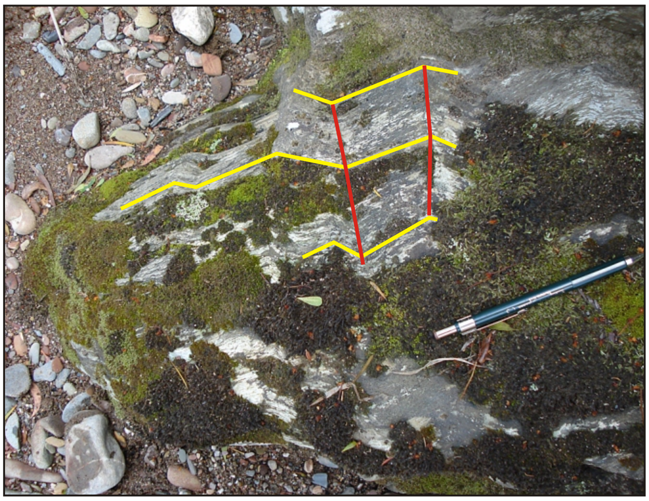

(a) Symmetric kink fold at 592 692 mE, 5 409 407 mN.

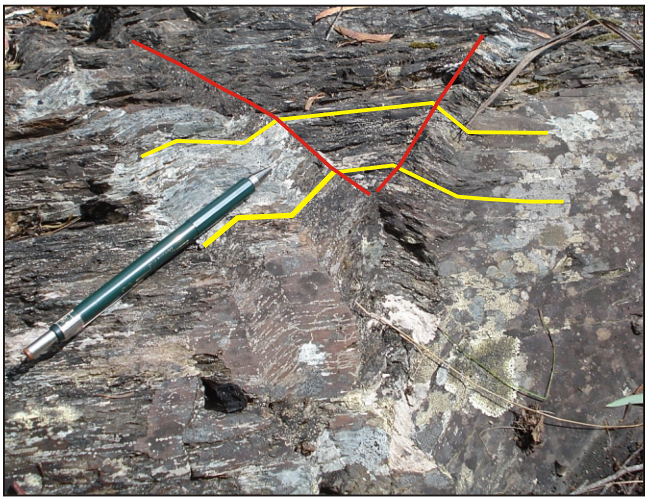

(b) Conjugate kink fold at 592 752 mE, 5 409 527 mN.

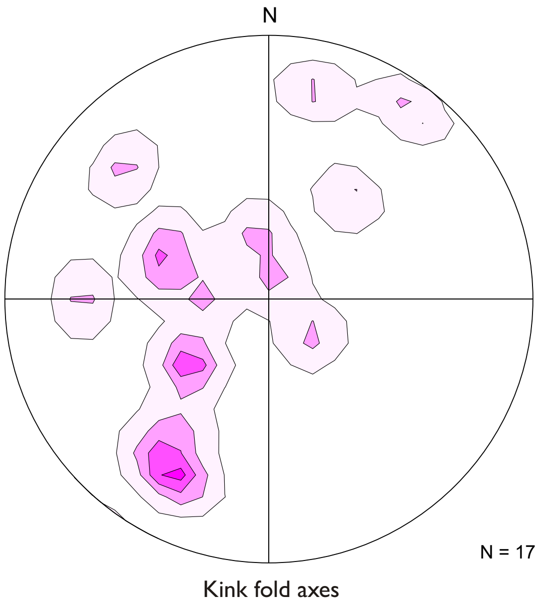

(c) Plot of kink fold axes.

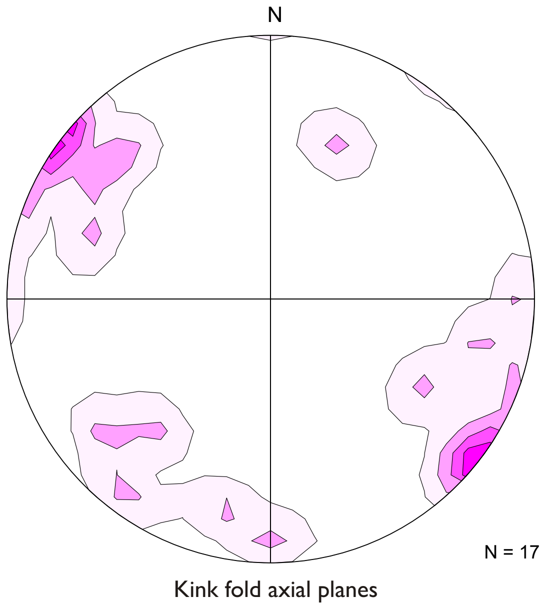

(d) Plot of poles to kink-fold axial planes.

Figure 33

Kink folds in SDpd along the Avenue River.

and were formed at shallow crustal levels (120 ± 45 MPa) which corresponds to depth of 4.2 kilometres. The small-scale kinks were rotated by the megakinks, suggesting progressive up-scale deformation. Both were formed by a 166° ± 10° trending bulk shortening strain which deformed the sub-vertical S_1 cleavage which trended 157°. A small component of shortening (4–5%) suggested that kinks developed because of the acute angle (9°) between the principal shortening axis and the trend of the pre-existing S_1 cleavage (Goscombe *et al.*, 1994). The northeast to southwest orientation of the kink bands described above is approximately the same as that recorded by Goscombe *et al.* (1994), and we can conclude that they are part of the same system.

According to Goscombe *et al.* (1994) the megakinks post-date contact metamorphism of the Middle Devonian Scottsdale Batholith (387 ± 2.3 Ma) (Black *et al.*, 2004) but pre-date deposition of the Parmeener Supergroup between 300 and 200 Ma (Goscombe *et al.*, 1994). The megakinking correlates with similar structures in the Lachlan Fold Belt which occurred under the same bulk shortening direction in the Middle Carboniferous. Thus a similar age is inferred for the kink bands described above.

Western area

This area includes all of the terrain to the east of the Catos Creek Dyke and is represented on the 1:25 000 scale Brilliant (Worthing and Woolward, 2010*a*) and Dublin Town (Worthing and Woolward, 2010*b*) map sheets. Access to this area is more difficult, as there are fewer forestry tracks and the terrain is more rugged. Mapping relied on detailed logging of road sections plus traverses along the Avenue River, the latter providing excellent outcrop along most of its course. Lithologically, the area includes the SDpd up to the Avenue River Fault Zone (ARFZ) (Patison *et al*., 2001) and there are also outcrops of SDpd east of the Catos Creek Dyke. The ARFZ and areas to the western boundary of the project area comprise the SDpf and SDp (Worthing and Woolward, 2010*a,b*).

D_1 — major structures

The large-scale structure of this area is represented in three cross sections (fig. 34*a–d*). Section locations are given in Figure 1. Adjacent to the Catos Creek Dyke the structure is similar to the area east of the dyke. The D_1 folds are asymmetric and inclined to the east but towards the west the geometry becomes more upright.

D_1 — minor structures

Figure 35*a* shows a plot of S_0 for the area between the Catos Creek Dyke and the ARFZ. The diagram suggests that the area is dominated by upright folds trending approximately north to south with a negligible plunge. This is consistent with the picture seen in cross sections G–H and I–J (fig. 34*a*, *b*), although section G–H suggests that easterly fold vergence occurs towards the Catos Creek Dyke, a pattern consistent with that seen to the east of the dyke. As with areas to the east, the F_1 folds have a sub-horizontal plunge (fig. 35*b*) and axial plane orientations again suggest an upright geometry (fig. 35*c*). S_1 orientations are sub-vertical and statistically parallel to the fold axial planes (fig. 35*d*).

More detailed analysis of the structure in this area was permitted by a well-exposed road section along Catos Road (fig. 36*a*, see Figure 40 for location). The section starts at 254 m (593 212 mE, 5 404 772 mN and finishes at 189 m altitude (592 841 mE, 5 404 636 mN) and is therefore not horizontal as the diagram suggests. It is approximately 550 m in length and in the field the rocks are viewed looking southwards.

Figure 36*a* has been transformed electronically such that west is to the left of the diagram. Figure 37*a–c* shows a series of photographs of folds taken along this traverse. The rocks are a sequence of interbedded sandstone, siltstone and mudstone with one intercalated thick massive sandstone unit. A well-developed penetrative cleavage is present in the more pelitic facies. The stereograms (fig. 36*b–e*) show a compilation of the structural data from the traverse. They are very similar to the regional stereograms shown in Figure 35*a–d*. The traverse reveals complex deformation structures with fold wavelengths up to 40 metres. A number of thrusts are apparent which dip both to the west and the east. One of the interesting features of the traverse is the inconsistent vergence shown by the folds; some verging westwards and others eastwards. This variable vergence is also apparent in an anticline exposed in a creek section at 592 795 mE, 5 404 334 mN, close to the end of the traverse (fig. 37*d*). The view looks south and the structure has an outcrop height of about six metres and clearly verges to the west. The inconsistent vergence and the different orientations of the thrusts suggest the possibility that these rocks have been affected by a second, possibly coaxial deformation. This is also consistent with similar evidence presented with respect to the road section east of the Catos Creek Dyke (fig. 25*a*).

A second, less well-exposed section crops out in a forest track on the northern side of the Avenue River (fig. 38*a–c*) (see fig. 40 for location). This traverse starts at 588 893 mE, 5 408 720 mN at 229 m and finishes at 282 m (588 669 mE, 5 408 910 mN) and is also not horizontal as the diagram suggests. It is approximately 350 m long and in the field the rocks are viewed looking approximately southwards. Again, Figure 38*a* has been transformed electronically such that west is to the right of the diagram. The rocks are similar to those documented in Figure 36*a* although more massive sandstone beds are present. The outcrop is generally poor so more interpretation based on dip values has been used in creating the diagram. The stereograms (fig. 38*b,c*) are broadly similar to the regional pattern documented above (fig. 35*a–d*). Again the inconsistent vergence is apparent, suggesting the possibility of a second deformation, possibly coaxial with the first and involving some refolding of earlier folds.

When the structures shown by these traverses are compared with cross section G–H (fig. 34*a*) there is a mismatch in the fold wavelengths. Although the scale of section G–H is much larger than the two road sections, it is clear that it is only in a thrust slice in the central part of the section where the folds have similar wavelengths to those seen in the two road traverses. The line of G–H lies along the Avenue River where outcrop is sufficiently good to give confidence in the interpretation of this section. It is therefore possible that there are major décollement surfaces between the river section and the higher road sections that have partitioned the strain in this way. These may have been partly controlled by lithological differences.

In summary, a consistent pattern emerges for the area east of the ARFZ with respect to the major deformation phases. D_1 is expressed by folds and thrusts which are generally eastward verging except west of the Catos Creek Dyke, where a more upright style was observed. F_1 fold styles were influenced by lithological variations. A single, generally upright axial plane cleavage (S_1) was recorded which increases in intensity towards the west. There is some minor evidence of a second, possibly coaxial deformation expressed by inconsistent vergence and easterly-dipping thrusts observed in detailed road sections both east and west of the Catos Creek Dyke. However in all areas visited east of the Avenue River Fault Zone no evidence of fold interference patterns or folding of S_1 has been observed. There are two possible explanations for these observations and they will be addressed below.

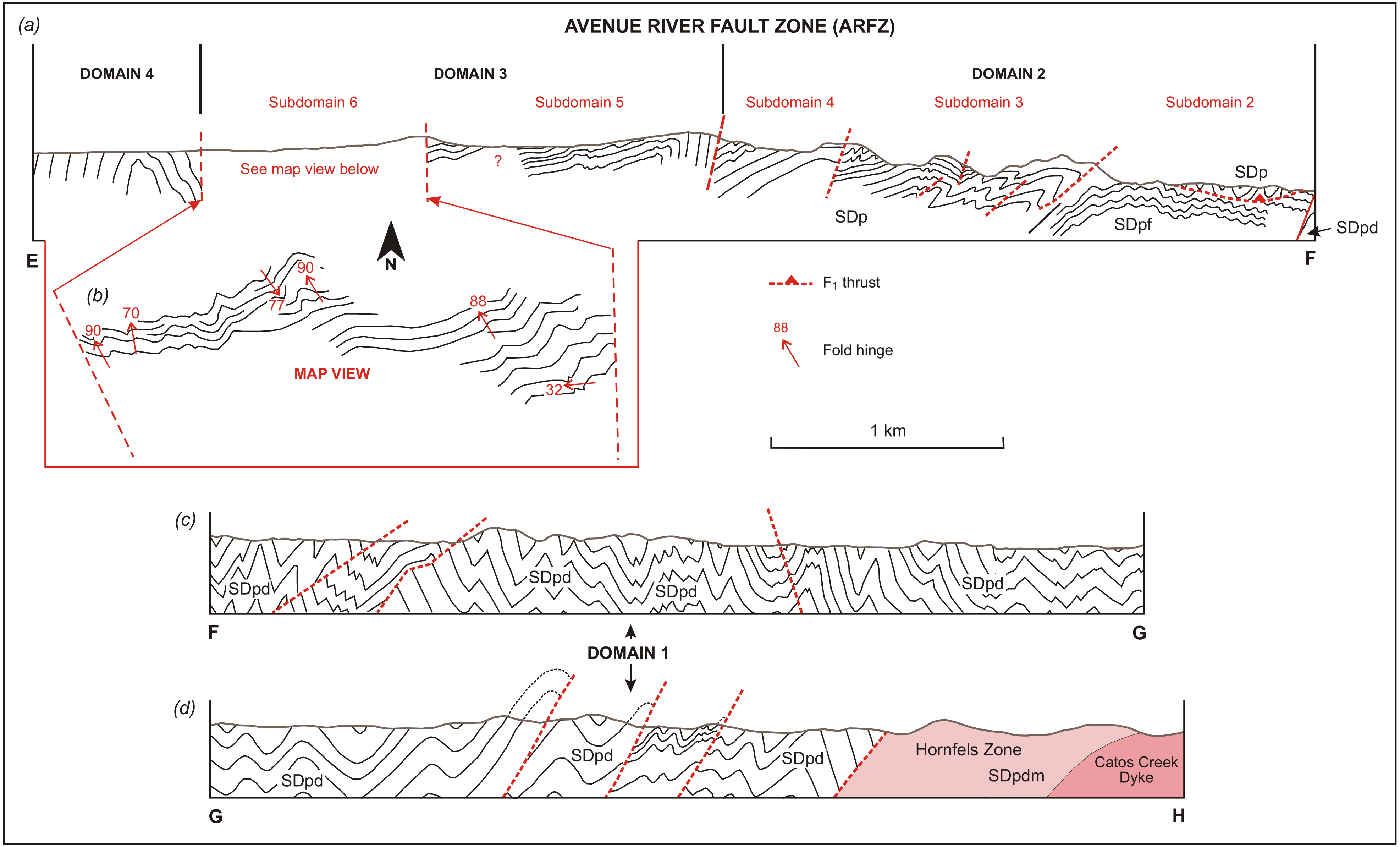

Figure 34

Cross sections west of the Catos Creek Dyke. All sections were compiled from traverses along the Avenue River and creeks to the west. The approximate line of sections is given in Figure 1. (a) (E–F) is a section across the Avenue River Fault Zone showing domains 2 to 4 and subdomains 2 to 6. The inset (b) is a map view of subdomain 6 showing steeply-plunging fold hinges. (c) section F–G and (d) section G–H which together comprise domain 1. See text for explanation.

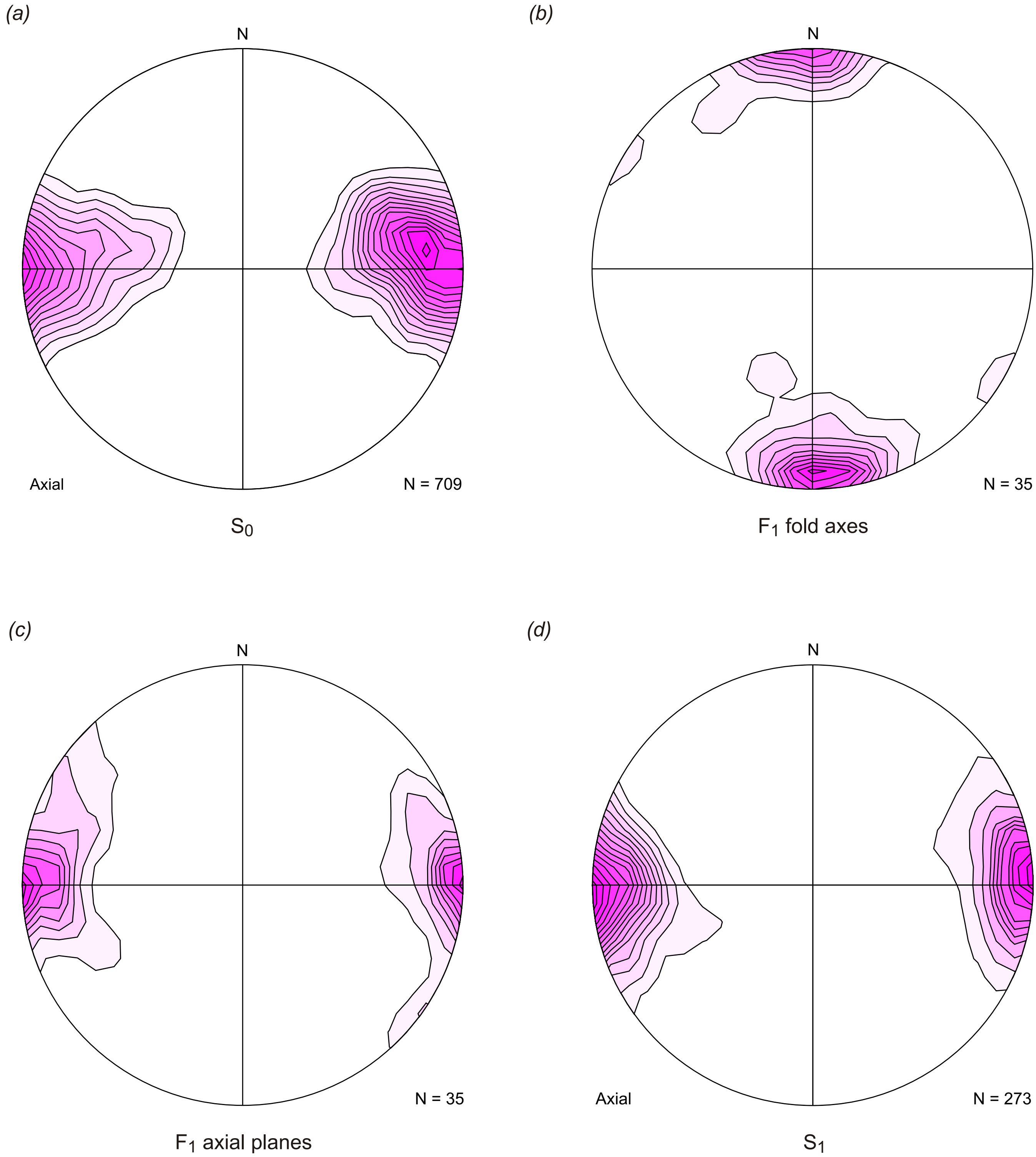

Figure 35

Structural data for SDpd between the Catos Creek Dyke and the Avenue River Fault Zone.

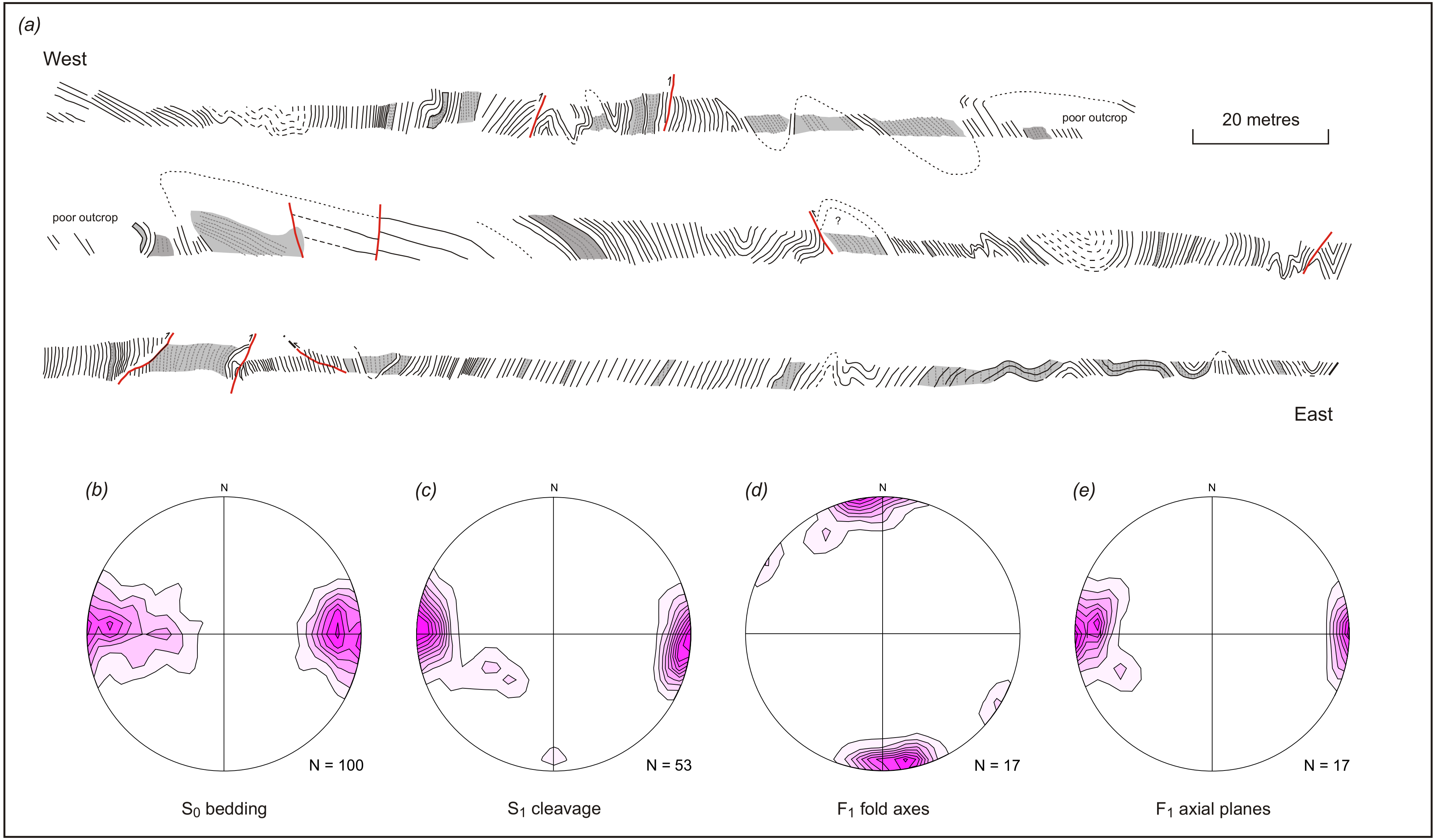

Figure 36

(a) Detailed cross section along Catos Road starting at 593 212 mE, 5 404 772 mN. In the field the section looks approximately south but has been transformed electronically such that west is on the left of the diagram. (b) Poles to S_0 for the section. (c) Poles to S_1. (d) F_1 fold axes. (e) Poles to F_1 axial planes. The outcrop consists dominantly of sandstone and siltstone, pelitic units are shaded. Cleavage in the pelitic units is shown as dashed lines. The thick unornamented unit is massive sandstone.

(a) (b) (c) (d)

Figure 37

(a) and (c) F_1 folds in detailed section (Fig. 36).
(b) and (d) Folds in road below detailed section (b) at 592 787 mE, 5 404 540 mN.
(d) Westerly-verging F_1 folds in creek at 592 795 mE, 5 404 334 mN.
For position of section see Figure 41.

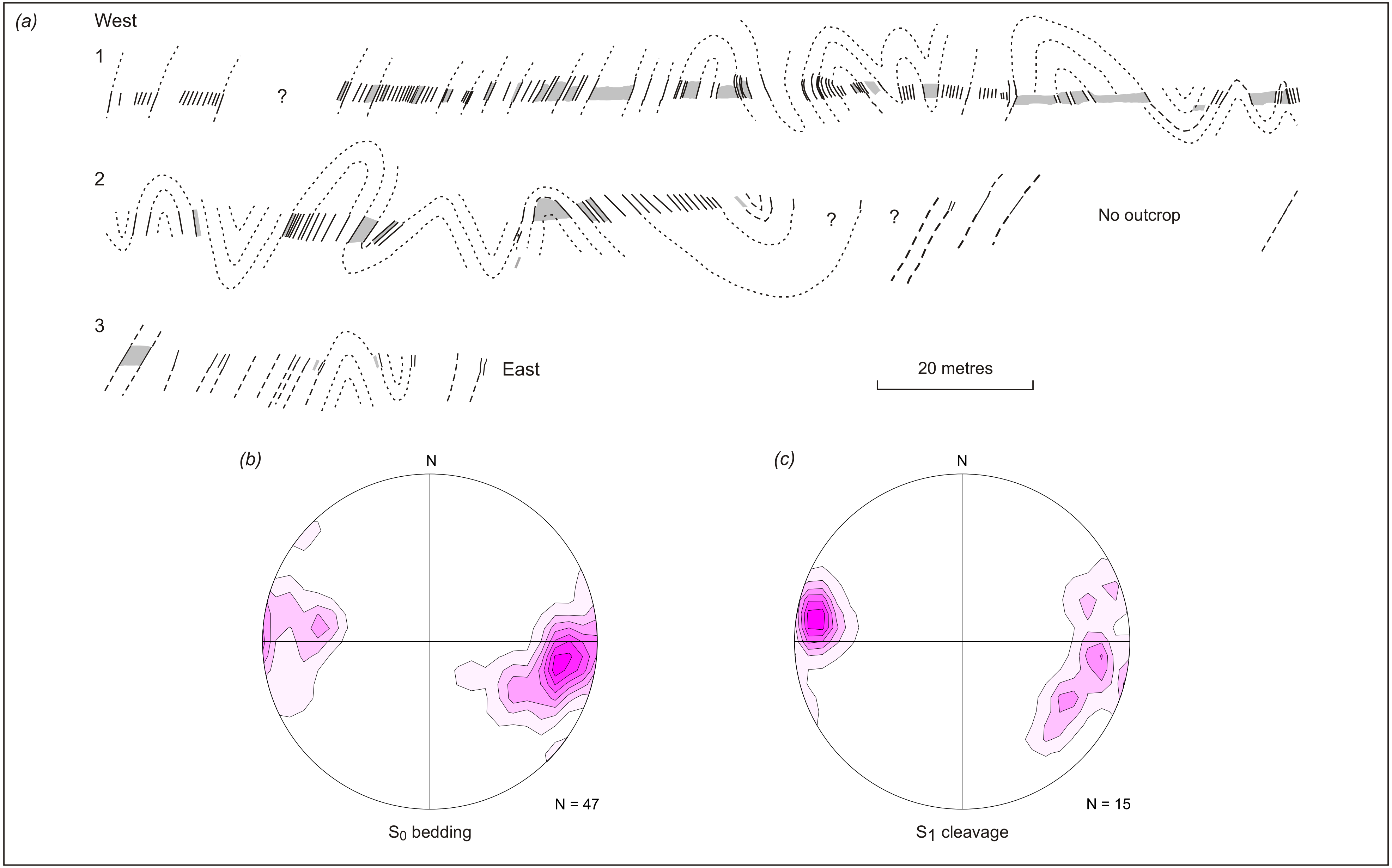

Figure 38

(a) Detailed cross section along track starting at 588 893 mE, 5 408 720 mN. The section looks approximately south but has been manipulated electronically such that west is on the left of the diagram. (b) Poles to S_0 for the section. (c) Poles to S_1 for the section. For position of section see Figure 41. The outcrop consists dominantly of sandstone and siltstone; pelitic units are shaded.

THE AVENUE RIVER FAULT ZONE (ARFZ)

This zone was first described by Patison *et al.* (2001) who mapped it as an approximately 3.8 km wide zone of westerly dipping D_1 folds and thrusts exposed along the Avenue River. Fieldwork for this project has shown that the zone extends five kilometres westwards from the thrusted contact with the SDpd, along the headwaters of the Avenue River, over Hogans Road to approximately one kilometre east of Evercreech Road (fig. 1, 34, 39). Lithologically the zone comprises the SDpf and the more dominant SDp, with the latter unit extending west of the ARFZ, almost to the western boundary of the project area (Worthing and Woolward, 2010*a,b*). Silurian graptolites were found at Golden Ridge, approximately four kilometres northwards along strike from this traverse (Rickards *et al.*, 1993). This implies that a Silurian age can be assigned to the SDp. Thrust faults further east of the ARFZ are considered to separate the Silurian rocks exposed within the zone from the Devonian Scamander Formation (Dpsf), the SDpq and SDpd. The biostratigraphic age of the latter two units is not known. The presence of the ARFZ and some of its interior structures is supported by geophysical evidence. For example, the thrust that defines the eastern boundary of the ARFZ, as well as thrusts within it, coincide with well-defined magnetic worms (fig. 13).

In this study, the area west of the Catos Creek Dyke was divided into four structural domains (fig. 39). Domain 1 is the area between the Catos Creek Dyke and the ARFZ. Domains 2 and 3 are the ARFZ itself and Domain 4 is the area west of the ARFZ. Detailed traverses along the Avenue River and adjacent creeks allowed the ARFZ to be further subdivided into six subdomains. Subdomain 2 is dominantly composed of the SDpf and the remaining subdomains by the SDp. Figure 39*f* shows the geographical distribution of the domains and subdomains and the structural relationships are summarised in a series of S_0 and S_1 stereograms. Figure 39 shows the data for Domain 1 which suggest an upright chevron geometry for the folds (fig. 39*c*) with an associated steeply-dipping S_1 cleavage (fig. 39*d*). Figure 39*e* shows the complex structural relationships within the ARFZ and Figures 39*a* and 39*b* the relationships in Domain 4 to the west. The latter are similar to Domain 1 but appear to have been rotated in an anticlockwise direction. This will be discussed in a later section.

The structural picture within the ARFZ is very different from areas to the east. The cross sections show a complex of faults and eastward-verging inclined asymmetric folds (fig. 34*a*–*b*). With respect to minor structures, recognition of the different structural elements along the traverse was problematic due to the fine-grained nature of the rocks and the difficulty in distinguishing between S_0, S_1 and S_2 in individual outcrops. At least two cleavages were recognised; an earlier one designated S_1 which has a variable orientation, and a second cleavage designated S_2 that trends approximately north–south and typically has a steep dip. Both S_1 and S_2 have been observed together in thin sections. The asymmetric folds within the ARFZ (fig. 34*a*) are quite different from the upright structures immediately east of the ARFZ in Domain 1 (fig. 34*c*). It is probable therefore that they are related to the S_2 cleavage and have been designated F_2. Structural data for the whole traverse are presented in Figure 39*e*.

The S_0 stereograms for subdomains 1 to 5 (fig. 39*e*) suggest an east to west rotational transition expressed in both S_0 and S_1. For example, the orientation of S_0 in Subdomain 1 is similar to that in Domain 1 to the east (fig. 39*c*) but the data show that a slightly rotated girdle has developed. This apparent clockwise rotation of S_0 continues incrementally from Subdomain 1 through to Subdomain 4 (fig. 39*e*) with a girdle developing suggesting the presence of folds plunging to the southwest in Subdomain 4. There is a significant increase in apparent rotation between subdomains 4 and 5. It should be borne in mind that Subdomain 5 has been rotated anticlockwise in a subsequent mega-kinking deformation which will be discussed later. If this is taken into account, the mismatch between subdomains 4 and 5 is even greater. Although there are insufficient data it is possible that Subdomain 5 has been rotated in an anticlockwise sense, i.e. in the opposite sense of subdomains 2 to 4 during the same rotational event. It is clear that there is an important structural break between subdomains 4 and 5.

Although there is less data, a similar rotation occurs with respect to S_1. The structures rotate in a clockwise sense and flatten in an east to west direction, although the differences between subdomains 4 and 5 are not as great as that shown by the S_0 data. There appears to be a decoupling of the rotation between S_0 and S_1 particularly between subdomains 1 and 4, with S_0 rotating further clockwise than S_1. This implies that S_1 increasingly transects the F_1 folds towards the west. The orientation of S_2 appears to be consistent across domains 2 and 3 although this is not shown in Figure 39*e*. Figure 40 shows calculated S_1/S_2 and S_0/S_1 intersections for all outcrops in domains 2 and 3 where both cleavage and bedding were recognised. Figure 40*a* shows that the S_1/S_2 intersections are coherent and in the case of Domain 2 suggest that the associated F_2 folds plunge just west of south whereas the Domain 3 folds plunge towards approximately 140°. The reasons for this difference can also be explained by the subsequent mega-kinking deformation and will be discussed further below.

The structural picture in Subdomain 6 is different. The S_0 plot lacks coherence and S_1 shows a developing girdle similar to that in Domain 4 to the west (fig. 39*a,b*). Field observations suggest that the structure here is complex, as minor fold hinges have a sub-vertical plunge (fig. 34*b*). In the westerly Domain 4 (fig. 39*a,b*) the patterns are again coherent and are similar to those recorded by Keele (1994) and by M. Vicary (pers. comm.) further to the west. The above data clearly show that the ARFZ is an important zone of structural transition between domains 1 and 4. Within this package, the boundary between subdomains 4 and 5 appears to mark a significant break as does the boundary between subdomains 5 and 6, the latter subdomain showing transitional features to the coherent Domain 4. All of these boundaries show associations of variable clarity with magnetic worms (fig. 13).

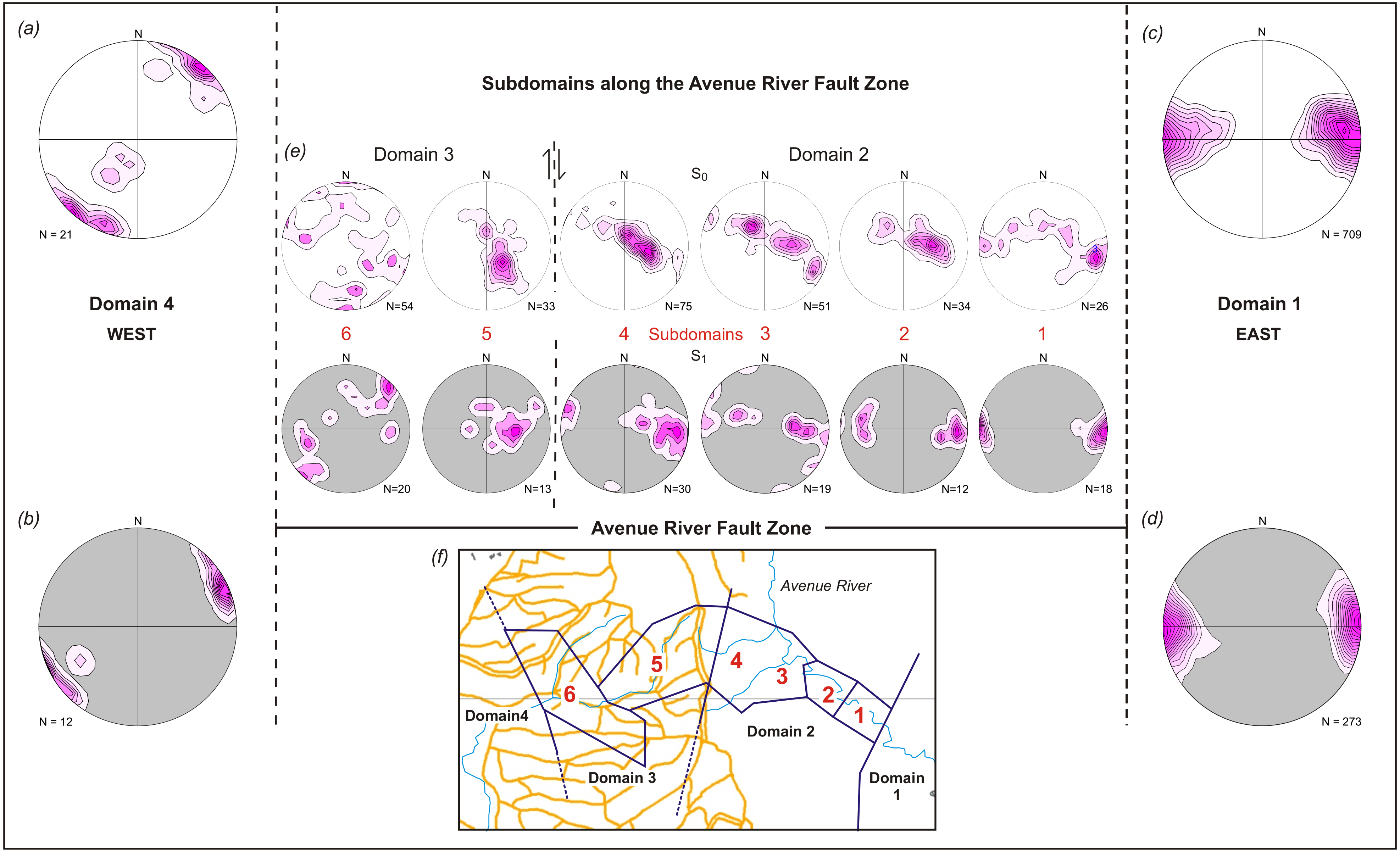

Figure 39

Structural domain changes across the Avenue River Fault Zone. Stereograms with a white background are S_0 and those with a grey background are either S_1 or S_2. See text for explanation. (a) and (b) are stereograms for Domain 4, (c) and (d) for Domain 1. (e) shows a series of stereograms for each of the subdomains along the ARFZ. (f) gives the location of the domains and subdomains in relation to the Avenue River and the tracks.

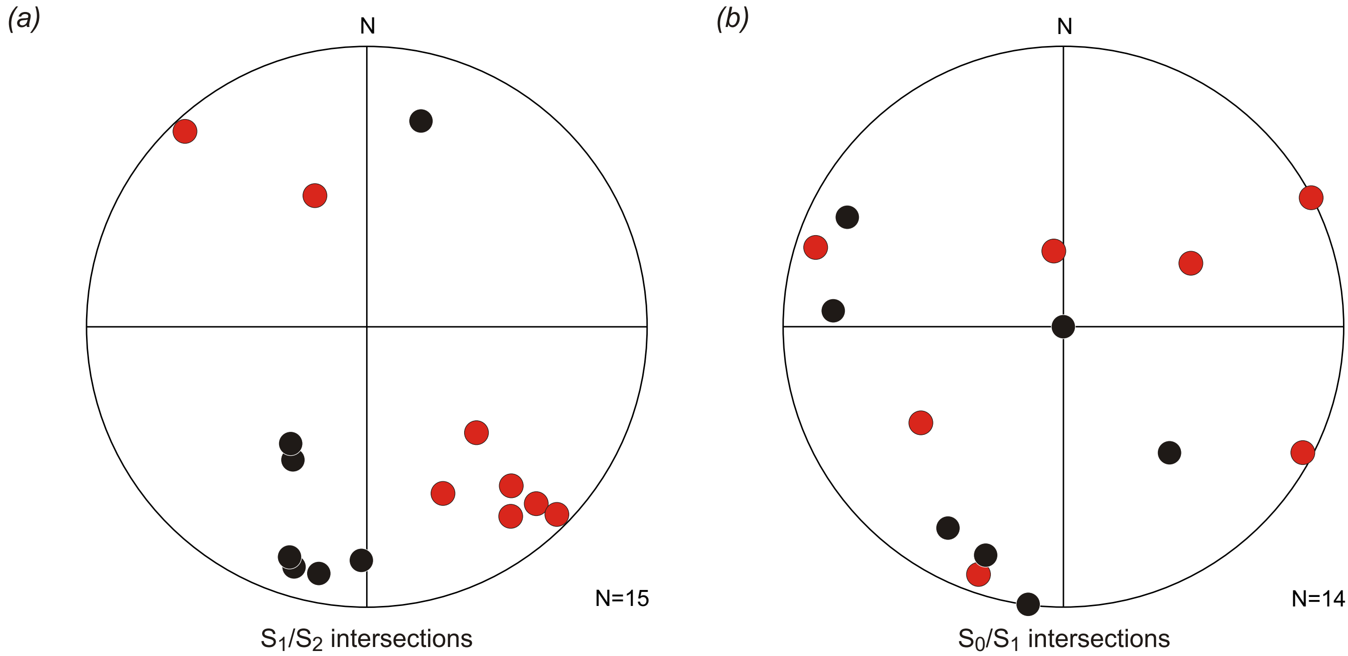

Figure 40

(a) S_1/S_2 intersections in domains 2 and 3. (b) S_0/S_1 intersections in domains 2 and 3. Black symbols Domain 2; red symbols Domain 3.

The rotations between subdomains 1 to 4 and between 4 and 5 described above are intriguing. They suggest that the western boundary of Subdomain 4, which also corresponds with the boundary between domains 2 and 3, is a significant structural break. In addition, the consistent approximately north to south orientation of S_2 noted above implies that this is a later structure and that the cleavage undergoing rotation is earlier, probably S_1. The simplest explanation for these observations is to infer a strike-slip fault between domains 2 and 3. The observed east to west rotational strains expressed in the stereograms may be related to proximity to such a structure, as drag effects would increase towards it. The sense of rotation suggests that the fault may have had a dextral strike-slip movement (fig. 39e) and the incremental nature of the changes suggests that movements occurred in a relatively ductile environment.

There is insufficient data to support a sense of rotation in Subdomain 5 but arguments presented above suggest that it could be opposite to that in subdomains 1 to 4. This would support a strike-slip model as the cause of the rotational strains as the drag on the western side of such a structure would be opposite to that on the east. It is possible that the proposed fault was an oblique thrust active during D_1. During deformation such a structure would have developed a transpressional component resulting in strike-slip movement along it. The apparent rotational decoupling between S_0 and S_1 could be explained by the fact that S_1 started to form after the F_1 folds, perhaps when sufficient strain had occurred to permit cleavage development. This resulted in transection of the folds by the evolving cleavage.

As noted above, the structures observed in Subdomain 6 are different and appear in part to be transitional to Domain 4 (fig. 39*a,b*), particularly with respect to S_1. However the vertical plunges shown by the minor folds (fig. 34*a,b*) suggest significant differences. The subdomain may be a rotated block at the top of the ARFZ, with rotation occurring during the same transpressional event described above. Fault boundaries have been inferred for the east and west contacts for this subdomain, the former may be associated with an abrupt north–south orientated termination of east–west trending magnetic worms (fig. 13).

A complicating factor in the above interpretation is the unknown influence of the granitoid intrusions that underlie the area. Seymour (in prep.) suggests that some of the observed deflections of S_1 at granite–Mathinna sediment contacts can be attributed to forceful intrusion rather than to the mega-kinking described by Goscombe *et al.* (1994). In the project area, Roach (1992) modelled an approximately westerly-dipping tabular granodiorite body under Domain 3 at 200 m depth. The shape and orientation of this body is consistent with emplacement in a thrust environment. It is also possible that the puzzling rotation of fold hinges in Subdomain 6 (fig. 34*a,b*) could be explained by forceful intrusion.

Most authors (e.g. Taylor, 1992; Duffet, 1992) accept that the Scamander Tier and Catos Creek dykes were intruded along D_1 thrusts. The good outcrop adjacent to these intrusions suggests that there has been only minor disturbance of D_1 structures although contact metamorphism is ubiquitous. In the case of the ARFZ therefore, the incremental nature of the rotations and the absence of contact metamorphism suggest that forceful intrusion was not a significant factor in the evolution of the observed structures.

Mega kinking

Evidence presented in Figure 39 shows that there are also significant differences in structural orientations between domains 1 and 4. The ARFZ appears to be a transitional zone between these two domains. For example, comparison of S_0 and S_1 orientations suggests that Domain 4 has been rotated by about 40° in an anticlockwise direction relative to Domain 1 (fig. 39*a–d*). Similarly, S_1/S_2 intersections within the ARFZ also show a mismatch across the boundary between domains 2 and 3 (fig. 40*a*). This mismatch suggests that Domain 3 intersections have also been rotated anticlockwise by 30° to 40° relative to Domain 2 (fig. 40*a*). The implied post-S_2 timing of this mismatch shows that this event was later than the rotations associated with the strike-slip faulting (fig. 39e).

The most likely explanation of these observations is that these later rotations are related to the mega-kinking documented by Goscombe *et al.* (1994). They recognised two mega-kink domains in the project area; an easterly one showing a statistical north–south trend for S_1 and a westerly domain showing a WNW trend (see also Keele, 1994). These statistical orientations have been confirmed by the current work. In the project area their mega-kink domain boundary approximately corresponds with the boundary between domains 2 and 3, which was identified above as the site of the strike-slip fault (fig. 39e). It appears that this structure was reactivated during the mega-kinking event. This boundary is also close to a well-defined magnetic worm (fig. 13). It is interesting to note that the principal shortening direction of 166° ± 10°, said to be responsible for the mega-kinking (Goscombe *et al.*, 1994), could also explain the approximately north–south compressive stress required by the orientation of F_3 folds in Dpsf associated with the Orieco Fault.

There are also some more subtle differences in structural orientations east and west of the Catos Creek Dyke (fig. 41). For example, the orientation of S_0 and S_1 west of the dyke appears to have been rotated by about 10° in a clockwise direction compared to S_0 and S_1 east of the dyke. It is possible that this difference may be related to rotational movements along a D_1 thrust now occupied by the dyke. Such movements may have been either syn-D_1 or later. Alternatively the rotation may be related to minor movement along a mega-kink boundary located close to the Catos Creek Dyke, although Goscombe *et al.* (1994) did not place a mega-kink boundary here.

Summary

Figure 41 presents a summary of the main structural elements for the whole project area, principally in terms of S_0 and S_1 orientations. East of the ARFZ the picture is relatively straightforward although there are variations in fold styles that can be related to lithology. One phase of cleavage was observed (S_1) and this is clearly associated with the F_1 folds. There is no evidence of a second deformation apart from a localised F_3 associated with late thrusting across the Orieco Fault (fig. 31). There is also no evidence for refolding of S_1, although the inconsistent vergence described in Figure 36 and Figure 38 and minor zones of steep easterly-dipping cleavages and thrusts does provide some evidence for a later, minor event.

The picture is much more complex within the ARFZ. S_0 and S_1 have undergone a rotational strain which appears to be related to a dextral strike-slip fault situated along the boundary between domains 2 and 3. This boundary also approximately corresponds to a well-defined north–south magnetic linear. The structural elements in Domain 4 are similar to those recorded further west by other authors (Keele, 1994; M. Vicary, pers. comm.). Subsequently, this domain was rotated about 40° in an anticlockwise sense relative to Domain 1. This was attributed to mega-kinking along the boundary between domains 2 and 3 (Goscombe *et al.*, 1994). We will now consider how these different threads of evidence fit into a regional context.

Discussion

Patison *et al.* (2001) recognised two regional folding events in the Mathinna Supergroup; an Early Devonian phase (D_1), characterised by northeast to east-directed thrusting with regional scale F_1 folds and thrusts, and an associated S_1 cleavage. They suggested that this event caused structurally induced crustal thickening of up to ten kilometres resulting in the post-D_1 attainment of peak metamorphism. An illite crystallinity survey across the entire outcrop area demonstrated a regional west to east decrease in temperature, although Patison *et al.* (2001) noted that peak metamorphism did not correlate with stratigraphic position or age and did not change across most of the large faults.

The ARFZ was an exception, as a significant variation in illite crystallinity could be demonstrated across it. Patison *et al.* (2001) concluded that additional post-D_1, post-peak metamorphism movement had occurred. The geometry of this variation suggested that the higher temperature Silurian rocks to the west of the ARFZ were thrust eastwards over the younger, lower temperature rocks to the east. Patison *et al.* (2001) also suggested that D_1 was followed by late Middle Devonian westward-directed thrusting (their D_2) which post-dates the unconformable St Marys Porphyrite and associated intrusions (fig. 1).

This event was also documented in the far west of the Mathinna Supergroup outcrop area by Powell and Baillie (1992). Here it is clearly expressed by southwesterly-verging imbricate thrusting but its effects appear to be weak or non-existent in the project area. Patison *et al.* (2001) suggested that it provides evidence in the project area for a "foreland propagating thrust wedge", although the relationship between their D_2 event and the 'thrust wedge' is unclear as the foreland during D_1 was presumably to the east.

Keele (1994) also recognised two phases of folding, denoted F_1 and F_2, associated with the Mathinna–Alberton gold lineament immediately to the west of the project area. The F_1 folds are northwest to NNW-trending structures that parallel the gold lineament and plunge at a shallow angle to the northwest and southeast. S_1 is steeply dipping and strikes northwest to southeast. These orientations are similar to those described in Domain 4 above (fig. 39*a,b*). Although the data set is small, Keele (1994) recorded a second fold generation (F_2). These folds are small scale at outcrop but larger scale folds are inferred from girdle distributions of S_0

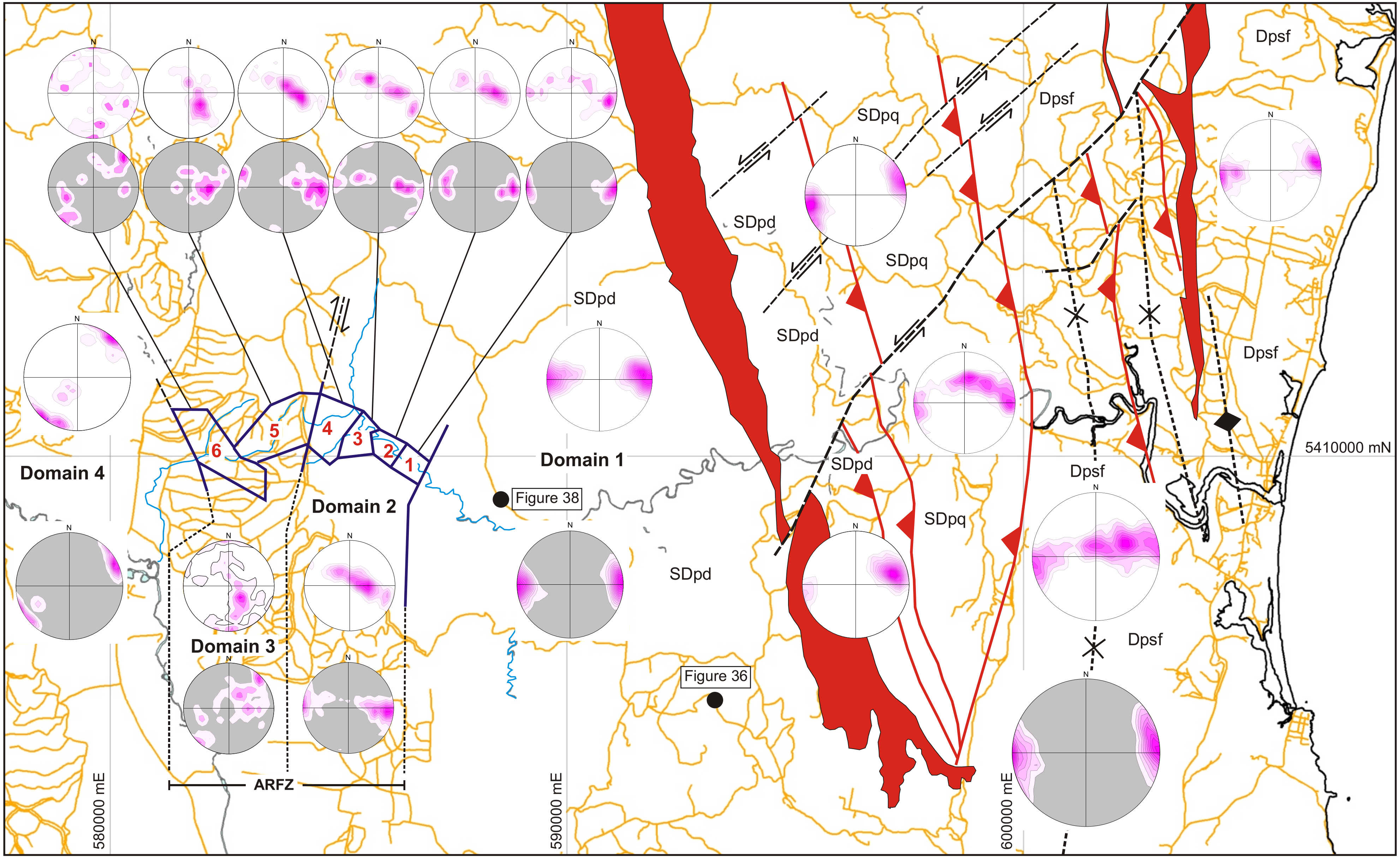

Figure 41

Map of the project area showing main structural features and major granitoid intrusions. The inset stereograms provide structural summaries. Stereograms with a white background are S_0 and those with a grey background are S_1. See text for explanation. For areas east of the Catos Creek Dyke the S_0 stereogram is larger as it covers the whole outcrop area of Dpsf. The S_1 stereogram is largest because it covers the outcrop area of Dpsf, SDpq and SDpd. The area west of the Catos Creek Dyke is divided into four structural domains. Domains 2 and 3 comprise the Avenue River Fault Zone and this was further subdivided into six subdomains. Structural stereograms for these subdomains are given at the top left of the diagram. Summary stereograms for domains 2 and 3 are given at the bottom of the diagram. The locations of the detailed road sections in Figures 36 and 38 are also shown. See text for explanation.

and S_1 on stereograms. The few F_2 folds measured have a similar azimuth to F_1 but a steeper plunge which can be related to the variable orientation of S_0 during F_2 deformation. The F_2 folds are associated with a north to northeast-trending axial plane fracture cleavage (S_2).

M. Vicary (pers. comm.) also recognised two fold phases in the Alberton area to the west. Shallow-dipping D_1 thrusts are truncated by steeply westerly dipping D_2 thrusts associated with F_2 folds and an S_2 cleavage. Structural orientations are similar to those described by Keele (1994). It seems more likely that the post-metamorphic "foreland propagating thrust wedge" of Patison *et al.* (2001) may be equated with the D_2 recorded in the ARFZ and by Keele (1994) and Vicary (pers. comm.) further west.

The most simple explanation for these data is that an early major compressional event (D_1) resulted in the formation of generally eastward-verging folds and thrusts across the whole project area. Within the ARFZ, dextral strike-slip movements developed on an oblique D_1 thrust which now lies along the boundary between domains 2 and 3. These D_1 movements resulted in rotational strains which increased in intensity towards the fault causing incremental rotation of bedding and cleavage from east to west towards the fault. This could have occurred at any time within the protracted D_1 event (Turner and Calver, 1987). This deformation was subsequently overprinted by a second event (D_2) which gave rise to F_2 folds (fig. 34*a,b*) and a second cleavage (S_2) which had a consistent approximately north–south trend. This D_2 deformation was not expressed in the rocks east of the ARFZ except possibly in the inconsistent vergence observed in some road sections. This may be related to the lower temperatures suggested by the illite crystallinity data. Higher temperatures in the west may have made the Silurian rocks more ductile when they were thrust over the cooler Devonian strata to the east.

The ARFZ is interpreted here as a westward-dipping thrust zone which may have been initiated during D_1 but was the locus of further eastward movements during D_2 resulting in eastward-verging folds (fig. 34*a*) and a north–south trending S_2 cleavage. This would explain the post-metamorphic, post-D_1 movements described by Patison *et al.* (2001).

Finally, substantial rotation occurred during a regional mega-kinking event (Goscombe *et al.*, 1994). This resulted in an anticlockwise rotation of about 40° of Domain 4 relative to Domain 1. The location of the mega-kink domain boundary was the strike-slip fault defining the contact between domains 2 and 3 in the ARFZ.

There appear to be two possible explanations for the inconsistent vergences and easterly-dipping thrusts recorded in rocks east of the ARFZ. These could be related to minor effects of the D_2 deformation described above or alternatively they could be caused by the westerly-directed thrusting event of Patison *et al.* (2001) and Powell and Baillie (1992). Whichever is the case, the effects are only weakly expressed in the project area. In view of this uncertainty the structures have been assigned to either D_2 or D_4 in the following summary and in Table 4.

Table 4

Summary of structural events across the project area.

Deformation Phase	Folds/Foliations	Faults	Folds/Foliations	Faults
	ARFZ and area to the WEST		**EAST of ARFZ**	
D_{1A}	F_1 folds eastward facing and inclined with open to tight interlimb angles. S_1 has approximately N–S sub-vertical orientation.	Easterly transport along west-dipping thrust faults.	F_1 folds eastward facing and inclined with open to tight interlimb angles. S_1 has approximately N–S sub-vertical orientation.	Easterly transport along west-dipping thrusts. Orieco Fault active as lateral ramp.
Intrusion	Intrusion of St Marys Porphyite, Catos Creek Dyke and Scamander Tier Dyke at 388 ± 1 Ma (Turner *et al*., 1986). Catos Creek and Scamander Tier dykes probably intruded along F_1 thrusts.			
D_{1A}	Tightening of F_1 folds. In ARFZ rotational strains associated with dextral strike-slip fault.	Continued easterly transport along west-dipping D_1 thrusts.	Tightening of F_1 folds.	Continued easterly transport along west-dipping D_1 thrusts.
D_{1B}	Quartz-veins developed in similar stress field to D_{1A}.			
D_2	F_2 folds have approximately N trend. Axial planes striking N–S. Associated S_2 steeply dipping to west.	Higher grade Silurian rocks to west thrust over lower grade Devonian rocks to east along ARFZ.	Minor local coaxial reorientation of D_1 folds to westerly vergence. Uncertain if this is caused by this D_2 or D_4? Equivalent to D_2 of Patison *et al*. (2001)?	Local westerly transport along east-dipping thrusts. Uncertain if they are related to this D_2 or D_4? Equivalent to D_2 of Patison *et al*. (2001).
D_3			F_3 open upright folding locally developed. Trending to 240° with axial plane S_3 foliation.	Sinistral strike-slip movements on Orieco Fault and other NE–SW trending faults. E–W strike changes explained by south-directed thrusting.
D_4?	Minor local coaxial reorientation of D_1 folds to westerly vergence. Equivalent to D_2 of Patison *et al*. (2001)?	Local westerly transport along east-dipping thrusts. Equivalent to D_2 of Patison *et al*. (2001)?	Minor local coaxial reorientation of D_1 folds to westerly vergence. Equivalent to D_2 of Patison *et al*. (2001)?	Local westerly transport along east-dipping thrusts. Equivalent to D_2 of Patison *et al*. (2001)?
D_5			Movement on low angle extensional faults seen along Semmens Road.	
D_6	Kinks and mega-kinks post-date 387 ± 2.3 Ma (Goscombe *et al*., 1994). West of Catos Creek Dyke resulted in anticlockwise rotation of ~40° of Domain 4 relative to Domain 1. Also possible minor clockwise rotation of Domain 1 relative to area east of Catos Creek Dyke.			
Intrusion	Regional dolerite dyke swarm intruded at 330.2 ± 5.6 (McClenaghan and Everard, in prep.).			

Tectonic summary for the whole area

A summary of the structural chronology is given in Table 4.

- D_{1A} — The dominant structural grain of the area was determined during D_{1A}. Work by Turner and Calver (1987) suggested that this was a protracted event interrupted by intrusion of the St Marys Porphyrite along early thrusts. It produced westerly-dipping thrusts and associated easterly-verging folds which plunge slightly east of south and have steep westerly-dipping axial planes. An axial plane cleavage is poorly developed to the east but increases in intensity westwards across the area. Fold styles were strongly influenced by lithology. During D_{1A} the Orieco Fault was active as a lateral ramp and differential movement on either side has produced a mismatch in fold styles across it. Stacking of D_1 thrust nappes resulted in structural thickening of up to ten kilometres (Patison *et al.*, 2001). In the ARFZ, transpressional movements on an oblique thrust resulted in a dextral rotational couple that deformed S_0 and S_1. West of the ARFZ the structural picture was probably the same as that prevailing east of the ARFZ.
- D_{1B} — The quartz veins post-date emplacement of the St Marys Porphyrite and its associated feeders, the Scamander Tier and Catos Creek dykes. The orientation of the stress field responsible for the veins is the same as that prevailing during D_{1A}.
- Peak metamorphism occurred post-D_1 caused by syn-D_1 crustal thickening. Highest grades were in the west and lowest in the east towards the coast (Patison *et al.*, 2001).
- D_2 — Post-peak metamorphic movement on the ARFZ gave rise to renewed folding and thrusting and reactivation of structures within the ARFZ. Higher grade Silurian rocks were thrust eastwards over lower grade Devonian rocks to east. F_2 folds and an S_2 cleavage developed in the ARFZ and to the west but in the east this event is possibly expressed by inconsistent fold vergences and easterly-dipping thrusts. The lower temperatures prevailing there may have contributed to the lack of a strong D_2 fabric.
- D_3 — Sinistral strike-slip movements occurred along the Orieco Fault and other sub-parallel faults. The close spatial association between the Orieco Fault, imbricate thrusts and D_3 folds suggesting transport towards 132° implies a genetic link with these movements. These structures may also be linked to anomalous changes in strike in forest outcrops south of the Orieco Fault and along strike further to the south in Semmens Road. These changes are related to south-directed thrusting with D_1 thrusts acting as transfer zones. Both the imbricate movements along the Orieco Fault and those along Semmens Road post-date the D_{1B} quartz veins. F_3 fold orientations suggested by the girdles generally agree with the (D_3 / F_3) fold trends associated with the Orieco Fault zone and the thrusting along Semmens Road.
- D_4? — Patison *et al.* (2001) and Powell and Baillie (1992) documented a westerly-verging mid-Devonian thrusting event. It is speculated here that this may be expressed by some easterly-dipping thrusts and/or by the inconsistent vergences also described under D_2 above.
- D_5 — Extensional faulting along low angle faults exposed along Semmens Road. The exact chronology of these structures is unclear.
- D_6 — Development of kink bands from outcrop to regional scale. The chronology of these structures is unclear but analogy with similar structures in the Lachlan Fold Belt of New South Wales suggests that they may be Carboniferous in age. There appears to be a mega-kink domain boundary between domains 2 and 3, implying reactivation of the strike-slip fault active during D_1. This rotated Domain 4 approximately 40° anticlockwise relative to Domain 1 (Goscombe *et al.*, 1994).
- Intrusion of dolerite dyke swarms along pre-existing northeast to southwest-trending faults. These dykes have been dated at about 330.2 ± 5.6 Ma (mid-Carboniferous) (McClenaghan and Everard, in prep.). This is about the same age inferred for the kink bands.

Acknowledgments

The authors wish to thank many colleagues at Mineral Resources Tasmania for their help in the preparation of this report. Particular thanks are due to David Seymour, who provided unstinting help and advice. IW also wishes to thank Mike Worthing for his generous support and guidance throughout the project. The authors also thank Gayle and Darryl Jones of the Kellraine Units in St Helens who provided excellent standard accommodation during the field work. Thanks are also due to Dennis and Ann Buchanan of Eureka Farm in Scamander for providing access to their property and for their hospitality.

REFERENCES

ARMSTRONG-ALTRIN J. S.; YONG IL LEE; SURENDRA, P. V.; RAMASAMY, S. 2004. Geochemistry of sandstones from the Upper Miocene Kundankulam Formation, southern India: Implications for provenance, weathering, and tectonic setting. *Journal of Sedimentary Research* 74:285–297.

BAHLBURG, H. 1998. The geochemistry and provenance of Ordovician turbidites in the Argentine Puna, *in:* PANKHURST, R. J.; RAPELA, C. W. (ed.). The Proto-Andean margin of Gondwana. *Special Publications Geological Society of London* 142:127–142.

BANKS, M. R. 1962. Silurian and Devonian systems. *Journal Geological Society of Australia* 9(2):177–188.

BANKS, M. R. 1992. A fossil from the Mathinna Beds, near Evercreech, northeastern Tasmania, *in:* TAYLOR, B. P. *Structural traverse across the Mathinna Group, north eastern Tasmania*. B.Sc. (Hons) thesis, University of Tasmania.

BANKS, M. R.; SMITH, E. A. 1968. A graptolite from the Mathinna Group, north-eastern Tasmania. *Australian Journal of Science* 31:118–119.

BEACH, A. 1975. The geometry of en-echelon vein arrays. *Tectonophysics* 28:245–263.

BERRY, R. F.; SELLEY, D.; WHITE, M. J.; MEFFRE, S. 1997. Lithogeochemistry, *in: AMIRA Project P.291A. Structure and mineralisation of western Tasmania.* 33–58. CODES Special Research Centre, Geology Department, University of Tasmania.

BHATIA, M. R. 1983. Plate tectonics and geochemical composition of sandstones. *Journal of Geology* 91:611–627.

BHATIA, M. R.; CROOK, K. A. W. 1986. Trace element characteristics of graywackes and tectonic setting discrimination of sedimentary basins. *Contributions to Mineralogy and Petrology* 92:181–193.

BLACK, L. P.; CALVER, C. R.; SEYMOUR, D. B.; REED, A. 2004. SHRIMP U-Pb detrital zircon ages from Proterozoic and Early Palaeozoic sandstones and their bearing on the early geological evolution of Tasmania. *Australian Journal of Earth Sciences* 51:885–900.

BLACK, L. P.; MCCLENAGHAN, M. P.; KORSCH, R. J.; EVERARD, J. L.; FOUDOULIS, C. 2005. Significance of Devonian–Carboniferous igneous activity in Tasmania as derived from U-Pb SHRIMP dating of zircon. *Australian Journal of Earth Sciences* 52:807–829.

BLACK, L. P.; EVERARD, J. L.; MCCLENAGHAN, M. P.; KORSCH, R. J.; CALVER, C. R.; FIORETTI, A. M.; BROWN, A. V.; FOUDOULIS, C. 2010. Controls on Devonian–Carboniferous magmatism in Tasmania, based on inherited zircon age patterns, Sr, Nd and Pb isotopes, and major and trace element geochemistry. *Australian Journal of Earth Sciences* 57:933–968.

BOYER, S. E.; ELLIOTT, D. 1982. Thrust systems. *Bulletin American Association of Petroleum Geologists* 66:1196–1230.

BUTLER, R. W. H. 1982. The terminology of structures in thrust belts. *Journal of Structural Geology* 4:239–245.

CRACKNELL, M. J. 2009. *Remote sensing geological structures using high resolution digital elevation models*. B.Sc. (Hons) thesis, School of Earth Sciences, University of Tasmania.

DEER, W. A.; HOWIE, R. A.; ZUSSMAN, J. 1965. *An introduction to the rock forming minerals*. Longman Group : London.

DEER, W. A.; HOWIE, R. A.; ZUSSMAN, J. 1992. *An introduction to the rock forming minerals (2nd edition)*. Longman Scientific and Technical : Harlow, England.

DUFFET, M. L. 1992. *Geophysics of the Scamander Mineral Field.* B.Sc. (Hons) thesis, University of Tasmania.

FEDO, C. M.; NESBITT, H. W.; YOUNG, G. M. 1995. Unraveling the effects of potassium metasomatism in sedimentary rocks and paleosols, with implications for paleoweathering conditions and provenance. *Geology* 23:921–924.

FERMOR, P. 1999. Aspects of the three-dimensional structure of the Alberta Foothills and Front Ranges. *Bulletin Geological Society of America* 111:317–346.

FISCHER, M. P.; CAMILO HIGUERA DÍAZ, I.; EVANS, M. A.; PERRY, E. C.; LEFTICARIU, L. 2009. Fracture-controlled paleohydrology in a map-scale detachment fold: Insights from the analysis of fluid inclusions in calcite and quartz veins. *Journal of Structural Geology* 31:1490–1510.

FODEN, J. D.; ELBURG, M. A.; TURNER, S. P.; SANDIFORD, M.; O'CALLAGHAN, J.; MITCHELL, S. 2002. Granite production in the Delamerian Orogen, South Australia. *Journal of the Geological Society* 159:557–575.

GOSCOMBE, B. D.; MCCLENAGHAN, M. P.; EVERARD, J. L. 1992. Contact metamorphism of the Mathinna Beds and the depth of crustal residence during mega-kinking in northeast Tasmania. *Report Department of Mines Tasmania* 1992/34.

GOSCOMBE, B. D.; FINDLAY, R. H.; MCCLENAGHAN, M. P.; EVERARD, J. L. 1994. Multi-scale kinking in northeast Tasmania: crustal shortening at shallow crustal levels. *Journal of Structural Geology* 16:1077–1092.

GRAY, C. M.; WEBB, J. A. 1995. Provenance of Palaeozoic turbidites in the Lachlan Orogenic Belt: strontium isotopic evidence. *Australian Journal of Earth Sciences* 42:95–105.

GRAY, D. R.; FOSTER, D. A. 2004. Tectonic evolution of the Lachlan Orogen, southeast Australia: historical review, data synthesis and modern perspectives. *Australian Journal of Earth Sciences* 51:773–817.

GROVES, D. I. 1972. The zoned mineral deposits of the Scamander–St Helens district. *Bulletin Geological Survey Tasmania* 53.

HANCOCK, P. L. 1985. Brittle microtectonics: principles and practice. *Journal of Structural Geology* 7:437–457.

HERRON, M. M. 1988. Geochemical classification of terrigenous sands and shales from core or log data. *Journal of Sedimentary Petrology* 58:820–829.

KEELE, R. A. 1994. Structure and veining in the Devonian-aged Mathinna–Alberton Gold Lineament, northeast Tasmania. *Report Mineral Resources Tasmania* 1994/06.

LEAMAN, D. 2008. Assessment of selected features in the 2007 magnetic surveys of North East Tasmania. *Geophysics Contractors Report Mineral Resources Tasmania* 2008/01.

MCCLENAGHAN, M. P. 1984. The petrology, mineralogy and geochemistry of the Pyengana and Gardens granodiorites, the Hogans Road diorite and the dolerite dykes of the Blue Tier batholith. *Unpublished Report Department of Mines Tasmania* 1984/04.

MCCLENAGHAN, M. P. 1996 (Compiler). *Geological Atlas 1:25 000 digital series. Sheet 5841. Brilliant.* Mineral Resources Tasmania.

MCCLENAGHAN, M. P. 2002*a* (Compiler). *Geological Atlas 1:25 000 digital series. Sheet 6041. Beaumaris.* Mineral Resources Tasmania.

MCCLENAGHAN, M. P. 2002*b* (Compiler). *Geological Atlas 1:25 000 digital series. Sheet 6040. Falmouth.* Mineral Resources Tasmania.

MCCLENAGHAN, M. P. 2006*a* The geochemistry of Tasmanian Devonian–Carboniferous granites and implications for the composition of their source rocks. *Record Geological Survey Tasmania* 2006/06.

MCCLENAGHAN, M. P. 2006*b* (Compiler). *Geological Atlas 1:25 000 digital series. Sheet 5840. Dublin Town.* Mineral Resources Tasmania.

MCCLENAGHAN, M. P.; TURNER, N. J.; WILLIAMS, P. R. 1987. *Geological Atlas 1:50 000 series. Sheet 41 (8515S). St Helens.* Department of Mines, Tasmania.

McClenaghan, M. P.; Turner, N. J.; Everard, J. L. 1992. Geological Atlas 1:50 000 series. Sheet 41 (8515S). St Helens. *Explanatory Report Geological Survey Tasmania*.

McClenaghan, M. P.; Everard, J. L.; Goscombe, B. D.; Findlay, R. H.; Calver, C. R. 1993. *Geological Atlas 1:50 000 series. Sheet 40 (8415S). Alberton.* Department of Mines, Tasmania.

McClenaghan, M. P.; Everard, J. L. (in prep.). Dolerite dykes of eastern Tasmania. *Record Geological Survey Tasmania*

McLennan, S. M.; Taylor, S. R.; McCulloch, M. T.; Maynard, J. B. 1990. Geochemical and Nd-Sr isotopic composition of deep-sea turbidites: Crustal evolution and plate tectonic associations. *Geochimica and Cosmochimica Acta* 54:2015–2050.

McQueen, K. G. 2006. Unravelling the regolith with geochemistry, *in:* Fitzpatrick, R. W.; Shand, P. (ed.). *Regolith 2006: Consolidation and dispersion of ideas.* Proceedings of the CRC LEME Regolith Symposium 2006. 230–234.

Naylor, M. A.; Mandl, G.; Sijpesteijn, C. H. K. 1986. Fault geometries in basement-induced wrench faulting under different initial stress states. *Journal of Structural Geology* 8:737–752.

Nesbitt, H. W. 2003. Petrogenesis of siliclastic sediments and sedimentary rocks, *in:* Lentz, D. R. (ed.). *Geochemistry of sediments and sedimentary rocks. Evolutionary considerations to mineral deposit-forming environments*. 39–51. Geological Association of Canada.

Patison, N. L.; Berry, R. F.; Davidson, G. J.; Taylor, B. P.; Bottrill, R. S.; Manzi, B.; Ryba, J.; Shepherd, R. E. 2001. Regional metamorphism of the Mathinna Group, northeast Tasmania. *Australian Journal of Earth Sciences* 48:281–292.

Pohn, H. A. 2000. Lateral ramps in the folded Appalachians and in overthrust belts worldwide — A fundamental element of thrust-belt architecture. *Bulletin U.S. Geological Survey* 2163.

Powell, C. McA.; Baillie, P. W. 1992. Tectonic affinity of the Mathinna Group in the Lachlan Fold Belt. *Tectonophysics* 214:193–209.

Powell, C. McA.; Baillie, P. W.; Conaghan, P. J.; Turner, N. J. 1993. The mid-Palaeozoic turbiditic Mathinna Group, northeast Tasmania. *Australian Journal of Earth Sciences* 40:169–196.

Ramsay, J. G.; Huber, M. I. 1987. *The techniques of modern structural geology. Volume 2: Folds and fractures*. Academic Press : London.

Reed, A. R. 2001. Pre-Tabberabberan deformation in eastern Tasmania: a southern extension of the Benambran orogeny. *Australian Journal of Earth Sciences* 48:785–796.

Rickard, M. J.; Rixon, L. K. 1983. Stress configurations in conjugate quartz-vein arrays. *Journal of Structural Geology* 5:573–578.

Rickards, R. B.; Banks, M. R. 1979. An early Devonian monograptid from the Mathinna Group, Tasmania. *Alcheringa* 3:307–311.

Rickards, R. B.; Davidson, G. J.; Banks, M. R. 1993. Silurian (Ludlow) graptolites from Golden Ridge, NE Tasmania. *Memoir Association Australasian Palaeontologists* 15:125–135.

Roach, M. J. 1992. Regional geophysics of the Alberton–Mangana goldfield, northeast Tasmania. *Bulletin Geological Survey Tasmania* 70:199–207

Roser, B. P.; Korsch, R. J. 1986. Determination of tectonic setting of sandstone–mudstone suites using SiO_2 content and K_2O/Na_2O ratios. *Journal of Geology* 94:635–650.

Roser, B. P.; Korsch, R. J. 1988. Provenance signatures of sandstone-mudstone suites determined using discriminant function analysis of major element data. *Chemical Geology* 67:119–139.

Rothery, E. 1988. En échelon vein array development in extension and shear. *Journal of Structural Geology* 10:63–71.

Seymour, D. B. (in prep.). Middle Devonian deformation, *in:* Corbett, K. D.; Quilty, P. G. (ed.). The geological evolution of Tasmania. *Special Publication Geological Society of Australia*.

Sloane, D. J. 1974. *The geomorphology of the Georges Bay area, St Helens*. B.Sc. (Hons) thesis, University of Tasmania.

Smith, J. V. 1996. Geometry and kinematics of convergent conjugate vein array systems. *Journal of Structural Geology* 18:1291–1300.

Sylvester, A. G. 1988. Strike-slip faults. *Bulletin Geological Society of America* 100:1666–1703.

Taylor, B. P. 1992. *Structural traverse across the Mathinna Group, north eastern Tasmania*. B.Sc. (Hons) thesis, University of Tasmania.

Taylor, S. R.; McClennan, S. M. 1985. *The continental crust: its composition and evolution*. Blackwell Scientific Publications : Oxford.

Thompson, R. N. 1982. Magmatism of the British Tertiary Volcanic Province. *Scottish Journal of Geology* 18:49–107.

Turner, N. J.; Black, L. P.; Higgins, N. C. 1986. The St Marys Porphyrite — a Devonian ash-flow and its feeder. *Australian Journal of Earth Sciences* 33:201–218.

Turner, N. J.; Calver, C. R. 1987. Geological Atlas 1:50 000 series. Sheet 49 (8514N). St Marys. *Explanatory Report Geological Survey Tasmania*.

Turner, N. J.; Calver, C. R.; Castleden, R. H.; Baillie, P. W. 1984. *Geological Atlas 1:50 000 series. Sheet 49 (8514N). St Marys*. Department of Mines, Tasmania.

Walker, K. R. 1957. The geology of the St Helens–Scamander area, Tasmania. *Papers and Proceedings Royal Society of Tasmania* 91:23–39.

Walker, R. G.; Mutti, E. 1973. Turbidite facies and facies associations, *in: Turbidites and deep-water sedimentation*. Short Course Notes Society of Economic Paleontologists and Mineralogists, Pacific Section. 119–157.

Williams, E. 1959. The sedimentary structures of the Upper Scamander Sequence and their significance. *Papers and Proceedings Royal Society of Tasmania* 93:29–32.

Woodcock, N. H.; Rickards, B. 2003. Transpressive duplex and flower structure: Dent Fault System, NW England. *Journal of Structural Geology* 25:1981–1992.

Worthing, M. A. (Compiler). 2010*a*. *Geological Atlas 1:25 000 digital series. Sheet 6041. Beaumaris*. Mineral Resources Tasmania.

Worthing, M. A. (Compiler). 2010*b*. *Geological Atlas 1:25 000 digital series. Sheet 6040. Falmouth*. Mineral Resources Tasmania.

Worthing, M. A.; Woolward, I. R. (Compilers). 2010*a*. *Geological Atlas 1:25 000 digital series. Sheet 5841. Brilliant*. Mineral Resources Tasmania.

Worthing, M. A.; Woolward, I. R. (Compilers). 2010*b*. *Geological Atlas 1:25 000 digital series. Sheet 5840. Dublin Town*. Mineral Resources Tasmania.

Wyborn, L. A. I.; Chappell, B. W. 1983. Chemistry of the Ordovician and Silurian greywackes of the Snowy Mountains, southeastern Australia: An example of chemical evolution of sediments with time. *Chemical Geology* 39:81–92.